Modelling the Effects of Short-Term Solar Variability on Stratospheric Chemistry

by

RYAN MUNCASTER

Department of Atmospheric and Oceanic Sciences

McGill University

Montreal, Quebec, Canada

June 2009

A thesis submitted to McGill University in partial fulfillment of the requirements of the degree of Master of Science (M.Sc.)

Abstract

A new stratospheric chemistry box model with a more accurate on-line photolysis calculation is used to study the effects of daily solar variability on stratospheric chemistry, both with and without dynamics. The chemical response on this time-scale has not been looked at before. The underlying mechanisms behind the chemical response are thoroughly analyzed using a step-by-step approach. The daily response is found to have the ability to be extrapolated to longer time-scales, specifically the 27-day cycle, and the inclusion of dynamics is found to reduce the response of ozone to solar variability. Also, the detailed analysis of chemical species other than ozone fills a gap in current research.

Résumé

Un nouveau modèle de boîte pour la chimie stratosphérique a été développé et est utilisé pour étudier les effets journaliers de la variabilité solaire sur la chimie stratosphérique, avec ou sans dynamique atmosphérique. La réponse chimique sur cette échelle de temps n'avait pas été étudiée. Les mécanismes sous-jacents à la réponse chimique sont analysés dans les détails en incluant progressivement les différents couplages. En outre, il est montré que la réponse journalière peut être extrapolée sur de plus longues échelles de temps, en particuliers pour le cycle de 27 jours. Lorsque la dynamique est introduite, il est montré que le signal en est diminué. L'analyse détaillée des espèces chimiques autres que l'ozone comble un manque dans l'état de la recherche actuelle.

Contents

List of Tables

List of Figures

Chapter 1

Introduction

1.1 Sun-Climate Relationship

The amount of solar irradiation that reaches the Earth's atmosphere can have a significant impact on the Earth's climate. The balance between the amount of incoming solar irradiation and outgoing terrestrial radiation establishes the radiative equilibrium temperature of the Earth's surface. Therefore a change in the amount of solar irradiation is one factor that controls the temperature on Earth. Variation in the total solar irradiance (TSI) over the 11-year solar cycle is approximately 0.1 % of the TSI. This equates to a direct radiative equilibrium forcing of 0.2 Wm^{-2} (*Fröhlich and Lean*, 2004), or a change in the temperature of Earth's surface by approximately 0.2 K (IPCC, 2001). However, a review of climate model results (*North et al.*, 2004) has shown that this change is much smaller than the actual climate response determined through analysis of observations. Therefore, the change in TSI must affect the Earth's climate through another mechanism. This mechanism is the absorption of solar irradiation by atmospheric gases, and the resulting feedback. These feedbacks can not be measured from observations and therefore must be evaluated using models that represent these processes (*Ravishankara*, 2005).

The absorption of solar irradiation in the stratosphere is dominated by ozone. The stratospheric ozone absorbs the incoming solar irradiation, specifically the ultraviolet (UV) wavelengths, resulting in a heating of the stratosphere. The UV absorption

causes the production of more ozone (Sec. 1.2), resulting in a feedback mechanism as increased concentrations of ozone will absorb more UV irradiation. Thus, ozone is the link between chemistry and dynamics as changes in the distribution of ozone result in changes in the heating rates in the stratosphere, which result in changes in the circulation patterns. Since the distribution of ozone can cause changes in circulation patterns, it is important to understand the factors that determine its distribution. Ozone distribution in the stratosphere is determined by circulation, chemical production, and chemical loss. Since the focus of this paper is the effect of solar variability on stratospheric chemistry, the latter two factors are now discussed in detail.

1.2 Stratospheric Chemistry

1.2.1 Chapman Theory

The production of ozone can be described by the Chapman mechanism, which requires the photolysis (described in Sec. 1.2.4) of O_2 by UV irradiation, creating two O atoms:

$$O_2 + h\nu \longrightarrow O + O \qquad (\lambda < 240nm). \tag{1.1}$$

The O atom then combines with O_2 to produce ozone:

$$O_2 + O + M \longrightarrow O_3 + M. \tag{1.2}$$

The O_3 molecules can also be photolyzed to produce more O atoms:

$$O_3 + h\nu \longrightarrow O_2 + O(^1D) \qquad (\lambda < 320nm), \tag{1.3}$$

$$O(^1D) + M \longrightarrow O + M, \tag{1.4}$$

$$Net : O_3 + h\nu \longrightarrow O_2 + O, \tag{1.5}$$

where Re. 1.4 produces heat. Notice that the photolysis of O_3 is not a sink of O_3 as the O atoms produced in Re. 1.5 can recombine with O_2 through Re. 1.2 to produce O_3. Due to this rapid conversion between O and O_3, it is convenient to define the O_x

family as $O_x = O + O_3$. Loss of O_3 is through the Chapman termination mechanism, which is the direct reaction between O and O_3:

$$O_3 + O \longrightarrow O_2 + O_2 \tag{1.6}$$

The destruction of ozone is not limited to Re. 1.6, but is also caused by catalytic loss cycles. The catalytic cycles that are discussed in this paper are the HO_x and NO_x cycles as they result in the largest ozone loss in the stratosphere and upper stratosphere. There are also Cl_x and Br_x cycles, however, these are secondary in importance for ozone chemistry and are not discussed for sake of briefness.

1.2.2 HO_x Catalytic Cycle

Ozone destruction by HO_x (where $HO_x = OH + HO_2$) requires OH, which is mainly produced by the oxidation of water vapour:

$$H_2O + O(^1D) \longrightarrow 2OH, \tag{1.7}$$

where the $O(^1D)$ atom is produced through the photolysis of O_3 (Re. 1.3). The resulting OH molecules react with O_3 producing HO_2 which further react with O_3:

$$OH + O_3 \longrightarrow HO_2 + O_2, \tag{1.8}$$

$$HO_2 + O_3 \longrightarrow OH + 2O_2, \tag{1.9}$$

$$Net : 2O_3 \longrightarrow 3O_2. \tag{1.10}$$

Thus the production of one OH molecule by Re. 1.7 can result in a significant loss of O_3. Another path available for the OH molecule is the conversion to HO_2 when reacting with O atoms:

$$OH + O + M \longrightarrow HO_2. \tag{1.11}$$

Here, OH is converted to HO_2 and together with Re. 1.9, cause O_x destruction. However, Re. 1.8 dominates Re. 1.11 in the stratosphere due to the larger concentrations of O_3 than O. Termination of the HO_x catalytic cycle occurs when OH reacts with HO_2:

$$OH + HO_2 \longrightarrow H_2O + O_2. \tag{1.12}$$

1.2.3 NO_x Catalytic Cycle

For NO_x (where $NO_x = NO + NO_2$), NO molecules react with O_3 or HO_2 to produce NO_2:

$$NO + O_3 \longrightarrow NO_2 + O_2, \tag{1.13}$$

$$NO + HO_2 \longrightarrow NO_2 + OH, \tag{1.14}$$

where Re. 1.13 dominates in the stratosphere due to the larger concentrations of O_3 than HO_2. The NO_2 molecules can then either photolyze to convert back to NO:

$$NO_2 + h\nu \longrightarrow NO + O, \tag{1.15}$$

resulting in a null cycle as the O atoms produced can react with the O_2 molecules produced in Re. 1.13 to produce O_3 (Re. 1.2), or the NO_2 molecules can react with O:

$$NO_2 + O \longrightarrow NO + O_2, \tag{1.16}$$

where Re. 1.13 and 1.16 create the NO_x catalytic cycle for O_3 destruction which can be summarized as the net reaction:

$$Net : O_3 + O \longrightarrow 2O_2. \tag{1.17}$$

Termination of the NO_x catalytic cycle occurs when the NO_x radicals are converted into the reservoirs of NO_x (HNO_3 and N_2O_5). This occurs through the reaction of NO_2 with O_3 and the subsequent conversion of NO_3 into N_2O_5:

$$NO_2 + O_3 \longrightarrow NO_3 + O_2, \tag{1.18}$$

$$NO_2 + NO_3 + M \longrightarrow N_2O_5, \tag{1.19}$$

or through the reaction of NO_2 with OH molecules:

$$NO_2 + OH + M \longrightarrow HNO_3. \tag{1.20}$$

However, the NO_x reservoirs are eventually converted back to NO_x radicals in the presence of sunlight:

$$N_2O_5 + h\nu \longrightarrow NO_2 + NO_3, \tag{1.21}$$

$$HNO_3 + h\nu \longrightarrow OH + NO_2, \tag{1.22}$$

$$HNO_3 + OH \longrightarrow NO_3 + H_2O. \tag{1.23}$$

1.2.4 Photo-Chemistry

Since the purpose of this paper is to study the effects of solar variability, and steps have been taken to ensure more accurate calculation of the photolysis rates, this section highlights the photo-chemistry that occurs and makes suggestions as to what can be anticipated when the amount of solar irradiation increases. Also, the differences between daytime and nighttime chemistry are pointed out.

First, certain chemical species are only present during the daytime when sunlight is available for photolysis to occur. O requires the photolysis of O_2 (Re. 1.1) or O_3 (Re. 1.5), OH requires the oxidation of water vapour (Re. 1.7), and conversion between NO_x reservoir species to NO_x radicals requires sunlight (Re. 1.21 - 1.23). Therefore any chemical reactions that require these chemical species will also only occur during the daytime, such as the production of O_3 (Re. 1.2). However, for the case of NO_x, the conversion into the reservoirs can take longer than a day, resulting in NO_x being present at night as well.

Next, the chemical reactions that involve photolysis or involve species that are produced by photolysis are expected to be enhanced when the amount of solar irradiation is increased. An increase in solar irradiation is expected to result in an increase in O_x production (Re. 1.1 and 1.2), an increase in OH production (Re. 1.7) and an enhanced conversion of NO_x reservoirs to NO_x radicals (Re. 1.21 - 1.23). However, it is impossible to anticipate how an increase in solar irradiation will propagate through all of the chemical reactions, and thus numerical modelling is necessary.

Photolysis Rates

To understand how an increase in solar irradiation affects chemical equations involving photolysis it is necessary to look at the details of the photolysis rates. The photolysis rate (J) is simply the reaction rate for a photolysis reaction, which involves the breaking of a chemical bond in a molecule X due to the energy of an incident photon:

$$X + h\nu \longrightarrow Y + Z \qquad \lambda < \lambda_{critical}, \tag{1.24}$$

where Y or Z is usually a radical, and the value of $\lambda_{critical}$ corresponds to the minimum energy required to break the chemical bond. The rate of reaction for Re. 1.24 is given by:

$$-\frac{d}{dt}[X] = \frac{d}{dt}[Y] = \frac{d}{dt}[Z] = J[X], \tag{1.25}$$

where J is calculated by:

$$J = \int_{\lambda} q_X(\lambda)\sigma_X(\lambda)I_\lambda d\lambda. \tag{1.26}$$

The photolysis rate depends on the quantum yield (q), absorption cross-section (σ) and the actinic flux (I). The quantum yield is the probability that the absorption of a photon will result in the photolysis of the molecule X, the absorption cross-section is the cross-sectional area of molecule X that is available to absorption, and the actinic flux is the number of photons crossing the unit horizontal area per unit time. The actinic flux is dependent on the Sun's intensity and the solar zenith angle (sza), and is thus dependent on latitude and longitude. Each variable is specific to a wavelength and the photolysis rate is integrated over the wavelength spectrum, however, specific wavelengths often dominate the calculation of the photolysis rate. The quantum yield is typically 1 at wavelengths smaller than $\lambda_{critical}$ and 0 above. The absorption cross-section typically increases with smaller wavelengths (higher energy). The actinic flux depends on the solar irradiation, and although the Sun can be considered a black-body in the visible part of the spectrum, it emits more than a blackbody in the UV. Thus it is important to not only consider the solar variation in the TSI, but the variation in the spectral solar irradiance (SSI) as well. Specifically for ozone, the UV wavelengths mentioned in Sec. 1.1 are of importance.

Solar Cycles and Solar Variability

Solar variability has different amplitudes on different time-scales. Typically, solar cycles with periods of 11 years, 27 days, 13.5 days, and 9 days are observed (*Fioletov*, 2009). In Fig. 1.1, the power spectrum of both TSI (F10.7 cm) and UV irradiation (205 nm) can be seen. The power spectrum represents the variability that occurs at each frequency or period. Peaks are seen for the 27-day, 13.5-day, 9-day, and 6.7-day

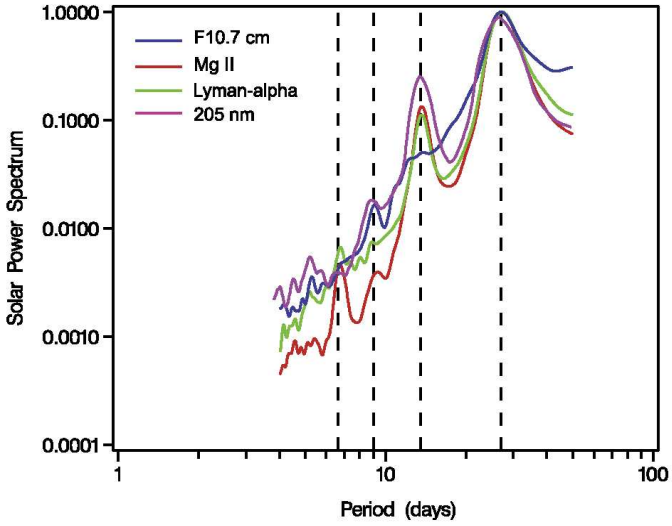

Figure 1.1: Time series power spectra for the three proxies of the solar signal: Mg II index, the solar flux at 10.7 cm, and composite Solar Lyman-alpha estimated for the period 1979-2005 and for SOLSTICE UV flux at 205 nm data set estimated for the period from September 1991 to June 2000. The solar spectra are normalized to the 27-day period value. The vertical lines indicate the 27, 13.5, 9, and 6.7-day periods. Source: *Fioletov* (2009).

periods. This paper focuses on the 11-year cycle and the 27-day cycle. The variation in the TSI over the 27-day cycle is twice as large (0.2 % of the TSI) as the variation in the 11-year cycle (Sec. 1.1), and variations in the UV wavelengths are even larger at this time-scale (seen in Fig. 1.1). Also, the variability increases as the wavelength decreases (*Fröhlich and Lean*, 2004). The spectrum of the variability used in the photolysis code (Sec. 2.1.2) (*Lean*, 1997a) is shown in Fig. 1.2 as the percent change between solar maximum and solar minimum.

1.3 Literature Review on the Effects of Solar Variability on the Stratosphere

The response of a climate system to a forcing can be analyzed by either looking into observations and using data correlation analysis, or by using numerical models to

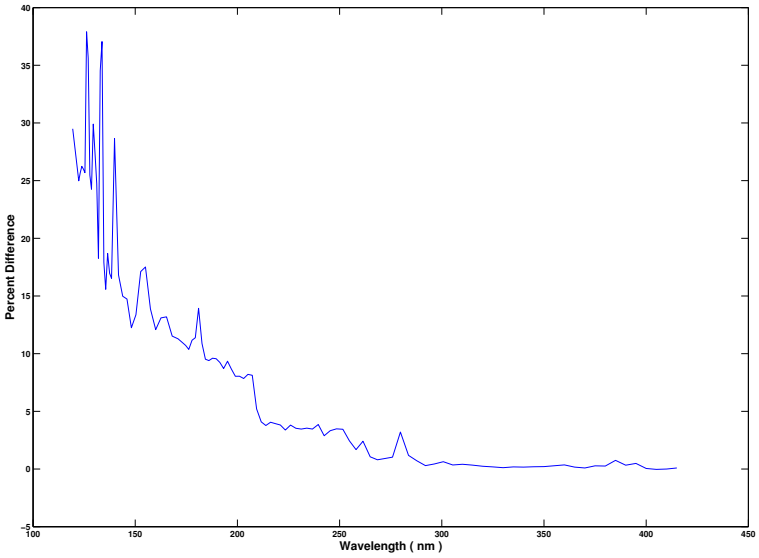

Figure 1.2: Spectral solar variability shown as the percent change between solar maximum and solar minimum for all wavelengths. Solar maximum and minimum spectrum is taken from SOLSTICE (*Lean*, 1997a).

simulate the response to such a forcing. In terms of observations, the data sets must be both accurate and long enough in duration. Since the purpose of this paper is to address the effects of solar variability, it would be necessary to have accurate, long-term data series representing solar variability. However, there aren't any long-term solar records, and furthermore the records are only recently becoming reliable due to the launch of satellites with solar observation as their purpose, such as the PICARD mission which is expected to launch in the fall of 2009 (*Thuillier et al.*, 2003). The only records long enough to study the 11-year cycle are the sunspot observations that are often of limited quality and require reconstructions with many assumptions in order to create a TSI record (*Crouch et al.*, 2008; *Solanki and Fligge*, 1999). In terms of numerical models, the models ideally would possess accurate depictions of the dynamics in the troposphere, stratosphere and mesosphere, a full radiation code, a full representation of the chemistry, and a high enough resolution to accurately depict atmospheric processes. Such a model would be extremely computationally expensive. Despite these difficulties, many attempts have been made to investigate the effect of solar variability on stratospheric chemistry, specifically stratospheric

ozone. In the literature, both types of analysis have been performed and each have their advantages.

First attempts to analyze the effects of solar variability involved determining the change in ozone between solar maximum and solar minimum conditions of the 11-year cycle. *Soukharev and Hood* (2006) and *Fioletov* (2009) used satellite observations and multivariate linear correlation to estimate the effects. Both studies found that the largest minimum-to-maximum difference occurred around 40 km and ranged from approximately 1 - 3 %, with large uncertainties in the calculations (seen in Fig. 1.3). Numerical modelling analysis has been performed by *Brasseur* (1993), *Haigh* (1994), *Shindell et al.* (1999), *Tourpali et al.* (2003), *Egorova et al.* (2004), and *Rozanov et al.* (2002, 2004). Amongst these models, the largest minimum-to-maximum difference also occurs around 40 km and ranges from approximately 2 - 3 % (*Matthes et al.*, 2003). A similar height and range was found by *Tourpali et al.* (2003) using a coupled chemistry-climate model (CCM). Values on the low end of the range (2 %) were found using a 2-D chemical-dynamical-radiative model by *Brasseur* (1993) and a CCM by *Egorova et al.* (2004), while values in the mid-to-high end of the range (2.5 - 3 %) were found using a 1-D chemical-radiative-convective model by *Rozanov et al.* (2002), a 2-D chemical-dynamical-radiative model by *Haigh* (1994), and CCMs by *Shindell et al.* (1999) and *Rozanov et al.* (2004). It is worth noting that the 1-D model by *Rozanov et al.* (2002) contains a convective adjustment and a parameterization of the vertical transport of long-lived trace gases. The results of some of the above models can be seen in Fig. 1.3, where it is clear that there is a large variation in the minimum-to-maximum difference calculated from both the observations and simulations, and therefore more work needs to be done in order to better assess the response of ozone to solar variability.

Further attempts included looking at the shorter time-scale solar cycles, specifically the 27-day solar cycle. For the purpose of analyzing the 27-day solar cycle an *ozone sensitivity* is usually looked at. The ozone sensitivity is defined as the percent change in ozone due to a 1 % change in the 205 nm solar flux. The 205 nm flux is considered because it is the 205 nm radiation that actually photo-dissociates O_2,

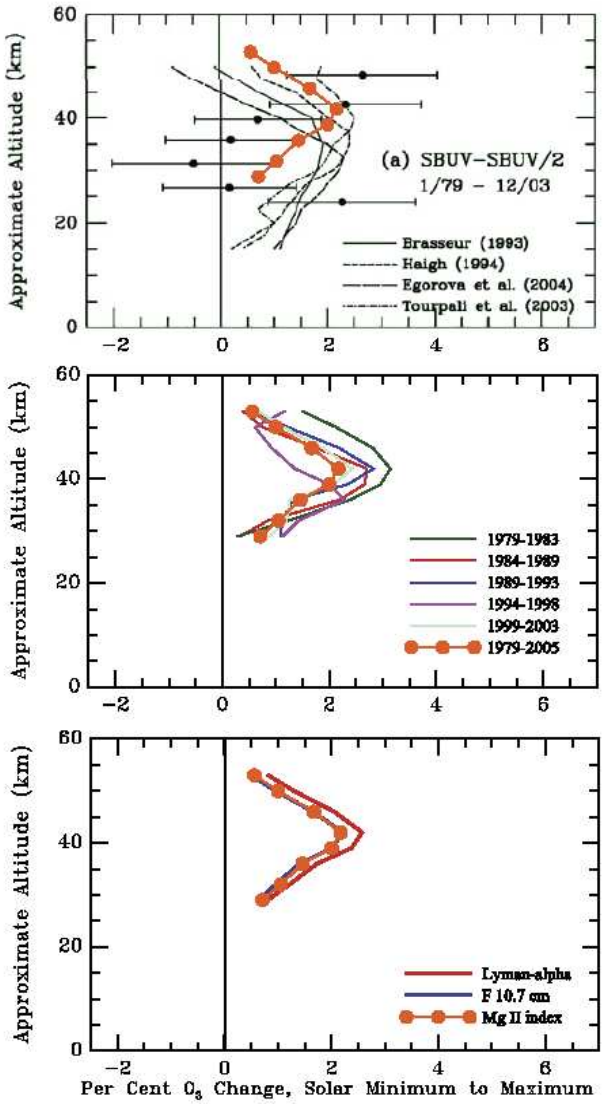

Figure 1.3: (top) Comparison of annual mean solar regression coefficients calculated from the SBUV(/2) analysis for 25° S - 25° N at selected levels (black dots) to simulations by a series of two- and three-dimensional stratospheric models that account for observed 11-year changes in solar UV spectral irradiance from Soukharev and Hood (2006) and estimated in this study from the 27-day cycle using Mg II data (the orange line). (middle) Estimates of the 11-year cycle amplitude from the 27-day cycle using Mg II data for different 5-year intervals. (bottom) Estimates of the 11-year cycle amplitude from the 27-day cycle using Mg II, Lyman alpha, and 10.7-cm flux data. Source: *Fioletov* (2009).

and because the 205 nm flux is the strongest solar signal with substantial variability (*Keating et al.*, 1987). Observational analysis of the 27-day cycle has been performed by *Keating et al.* (1987), *Hood and Zhou* (1999) and *Fioletov* (2009). *Keating et al.* (1987) found that there can be a large variation in the ozone sensitivity depending on the time period that is observed, specifically values ranging from approximately 0.25 - 0.7 %, with an average value of approximately 0.4 %. *Hood and Zhou* (1999) and *Fioletov* (2009) also found a value of 0.4 % when taking a long-term average. Simulations of the 27-day cycle response have been performed by *Brasseur et al.* (1987), *Brasseur* (1993), *Fleming et al.* (1995), *Williams et al.* (2001), *Rozanov et al.* (2006), and *Austin et al.* (2007). Again, large variations in the ozone sensitivities were found depending on the model year chosen. Using CCMs, *Rozanov et al.* (2006) found a spread between 0.2 - 0.8 % (seen in Fig. 1.4) and *Austin et al.* (2007) found ozone sensitivities ranging between approximately 0.2 - 0.5 %. Similarly to the observational analysis, the average value of the ozone sensitivity in the above simulations was approximately 0.4 %. When taking a long-time average over the simulations, a value of 0.4 % was also found using a 1-D chemical-radiative time-dependent model by *Brasseur et al.* (1987), a 2-D chemical-dynamical-radiative model by *Brasseur* (1993), and a CCM by *Williams et al.* (2001). Again, it is worth noting that the 1-D model by *Brasseur et al.* (1987) contains a parameterization of the vertical transport of long-lived trace gases, potential temperature, and heat. In an attempt to remove the effect of dynamical feedbacks, *Fleming et al.* (1995) used a 2-D photo-chemical model with pre-specified temperature and transport fields and found a slightly larger maximum value of 0.5 %. Therefore, although there is a large variation in the ozone sensitivities calculated from both observations and simulations, most of the long-term averages are in fairly good agreement with each other. However, much more work needs to be done in order to better understand the large variations in the calculated ozone sensitivities.

For studies on both the 11-year and 27-day solar cycle, a large scattering of results was found in the observational analysis. Issues with the length and accuracy of observational records has already been discussed as a possible explanation. Another

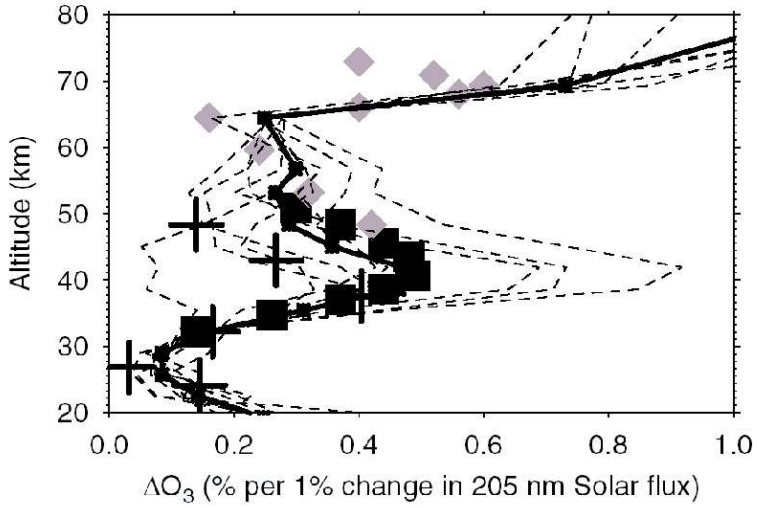

Figure 1.4: Ozone sensitivity to 1 % change of 205 nm solar flux for the maximum correlation. Simulated sensitivity is shown by solid line (ensemble mean) and dotted lines (ensemble members). Observed sensitivities are from MLS (Hood and Zhou, 1998; crosses), SBUV (Hood, 1986; squares), SME (Hood et al., 1991; diamonds) for the ozone. Source: *Rozanov et al.* (2006).

possible explanation is the problems associated with the linear multivariate analysis of the satellite observations. For this type of analysis it is necessary to include all of the predictor variables possible, and it is assumed that the predictor variables are orthogonal to each other. For ozone, two common predictor variables are the solar irradiation and the quasi-biennial oscillation (QBO), which are two variables that are not completely independent of each other. Thus it is hard to separate the response to each predictor variable. Also, the analysis only captures the linear dependencies. For these reasons, numerical modelling is used to help separate the effect of each predictor variable, and is the focus of this paper.

However, as mentioned previously, numerical modelling methods have limitations as well. Some of the models lack a full chemistry scheme (e.g., *Shindell et al.*, 1999) and probably all lack a full and accurate representation of the photo-chemistry. The photolysis rates for all of the above mentioned models are taken from a look-up table, which is calculated once for all simulations using standard atmospheric concentra-

tions of absorbing gases and standard atmospheric temperatures. The photolysis rates are calculated for several total ozone column amounts so that interpolation can be done on-line. In this paper, the aim is to model the effects of solar variability on stratospheric photo-chemistry with a chemistry model which includes an accurate, fully-interactive, on-line photolysis calculation (described in Sec. 2.1.2).

1.4 Objectives of the Study

The research presented in this paper attempts to model the effect of solar variability on stratospheric chemistry using a chemistry model with an on-line and fully interactive photolysis calculation (described in Sec. 2.1.1 and 2.1.2). This allows for a more accurate representation of the response of ozone, as well as other chemical species to solar variability. It adheres to the need of simulations using models with improved interaction of solar UV radiation, ozone, absorbing gases, and spectral redistribution of the TSI variations (*Fröhlich and Lean*, 2004). It also adheres to the need to assess the effect of atmospheric dynamics, as the dynamical perturbations caused by solar flux variability can change the transport process, which plays a substantial role in determining the chemical state of the atmosphere (*Egorova et al.*, 2005). This is all in an attempt to better understand the chemical mechanisms behind the correlations between solar irradiation and climate change, as the scientific understanding of solar forcing is still relatively low (IPCC, 2007).

The research in this paper starts by analyzing in detail the daily chemical response to solar variability. The chemical response on these time-scales has not been looked at yet. It is recognized that the chemical response to short-term solar variability can provide further understanding of the possible mechanisms driving the solar cycle ozone response (*Williams et al.*, 2001). The extent to which the daily response can explain the response to the 27-day cycle is then analyzed in the context of both chemistry only, and chemistry with atmospheric dynamics. But the very first step of this project was to build a chemistry model with an accurate, fully-interactive, on-line photolysis calculation. This assemblage is described next in Sec. 2.1.

Chapter 2

Methodology

2.1 Description of Model

2.1.1 BIRA Box Model

The model used in this study is the box model version (adapted by Ninad Sheode, Andrew Ryzhkov, and Michel Bourqui) of the BIRA (Belgian Institute of Research in Aeronomy) stratospheric photo-chemical scheme provided by Simon Chabrillat (*Khosravi et al.*, 2002). The model looks at a vertical column of the atmosphere between 10 to 55 km above the Earth's surface. At each 6 minute time step, the evolution of the 57 chemical species (Table 2.1) is determined by calculating the rates of 200 chemical reactions (Table A.2 in Appendix A.2). The concentrations of the following families are also kept track of: $Br_x = BrO + Br$, $Cl_x = ClO + Cl$, $HO_x = HO_2 + OH + H$, $NO_x = NO_2 + NO + NO_3$, and $O_x = O_3 + O + O(^1D)$.

2.1.2 Photolysis Code

Originally, the photo-chemistry was included by obtaining 52 photolysis rates (Table A.1 in Appendix A.1) from a look-up table. The look-up tables were calculated off-line using a radiation scheme that was extracted from the SOCRATES 2D

	Chemical Species
Bromine	Br, Br_2, $BrCl$, BrO, $BrONO_2$, HBr, $HOBr$
Chlorine	CCl_4, HCl, Cl, Cl_2, Cl_20_2, ClO, $ClONO_2$, $ClOO$, $OClO$, $HOCl$, $ClNO_2$
Freons	$CFC11$, $CFC12$, $CFC113$, $CFC114$, $CFC115$, $HCFC22$, $Ha1211$, $Ha1301$, HF, CH_3Br, CH_3CCl_3, CH_3Cl, $CHBr_3$
Hydrogen	H, H_2, H_2O, H_2O_2, HO_2, OH
Nitrogen	HNO_3, HNO_4, N ,N_2O, N_2O_5, NO, NO_2, NO_3
Organic	CH_3, CH_4, CH_2O, CH_3O_2, CH_3O, CH_3OOH, CO, CO_2, HCO
Oxygen	O , $O(^1D)$, O_3

Table 2.1: Chemical species that are included in the BIRA box model.

troposphere-stratosphere-mesosphere chemistry model, courtesy of Simon Chabrillat (*Khosravi et al.*, 2002). The photolysis rates were obtained at each time step. They are time-dependent by way of the sza and are only obtained when $sza < 96^o$. The look-up table was a function of height, total column ozone and sza. Thus only ozone was interactive to some extent with the BIRA box model through column ozone. The photolysis rates in the table were calculated between 0 - 120 km using standard atmospheric concentrations of the absorbing gases (O_3, O_2, NO, NO_2, CO_2, and air), standard atmospheric temperatures and pressures, and a solar spectrum with 171 wavelength intervals between 116.3 nm - 730 nm. The standard atmospheric temperatures, pressures and chemical concentrations were taken from MSIS (*Hedin*, 1991). The solar spectrum came from SOLSTICE (*Lean*, 1997a) and included maximum, minimum, and average solar irradiation at each wavelength interval. Either maximum, minimum, or average solar irradiation was used to calculate the look-up table to be used by the BIRA box model.

For the purpose of this study, the BIRA box model is modified to include an on-line calculation of the photolysis rates. This allows for more accurate photochemistry to occur. In order to do this, the scheme extracted from the SOCRATES

2D model is coupled to the BIRA box model. The photolysis rates are no longer interpolated from a look-up table, and are now interactive with all of the absorbing gases. The code is also modified to include a solar variability that is updated daily (at midnight), which is explained in greater detail in Sec. 2.2.2. The photolysis rates are now a function of height, sza, and the updated concentrations of all of the absorbing gases.

2.1.3 Verification of Modified BIRA Box Model

In order to verify that the modified BIRA model accurately calculates photolysis rates, the original BIRA box model (using the look-up table) and the modified BIRA box model (with on-line calculation of photolysis rates) are compared. In order to avoid differences due solely to interpolation, only heights, sza, and total ozone column amounts that are directly found in the look-up tables are used for the on-line calculation. Also, the concentrations of the absorbing gases are kept constant to ensure that the results are directly comparable.

Upon first comparison, differences between the modified BIRA and the original BIRA were found in several photolysis rates. In the modified BIRA, some photolysis rates were found to be orders of magnitude larger than expected at higher altitudes (50 - 55 km), and some photolysis rates were found to be lower than expected at all altitudes. It was quickly noted that the former of the two errors was caused by too much solar irradiation reaching the upper boundary of the BIRA model (55 km). This was due to the fact that the look-up tables account for the absorption of solar irradiation between 55 - 120 km, and the modified BIRA did not. To correct this, an artificial upper atmosphere is added to the modified BIRA model. Similarly to the SOCRATES code used to calculate the photolysis look-up table (used by the original BIRA), the concentrations of the absorbing gases in the artificial levels are taken to be standard atmospheric concentrations (MSIS). Standard atmospheric temperatures and pressures are also used (MSIS). The second difference in the photolysis rates occurred due to the lack of a troposphere in the modified BIRA. Again, the look-up table used in the original BIRA model accounts for the levels of the atmosphere

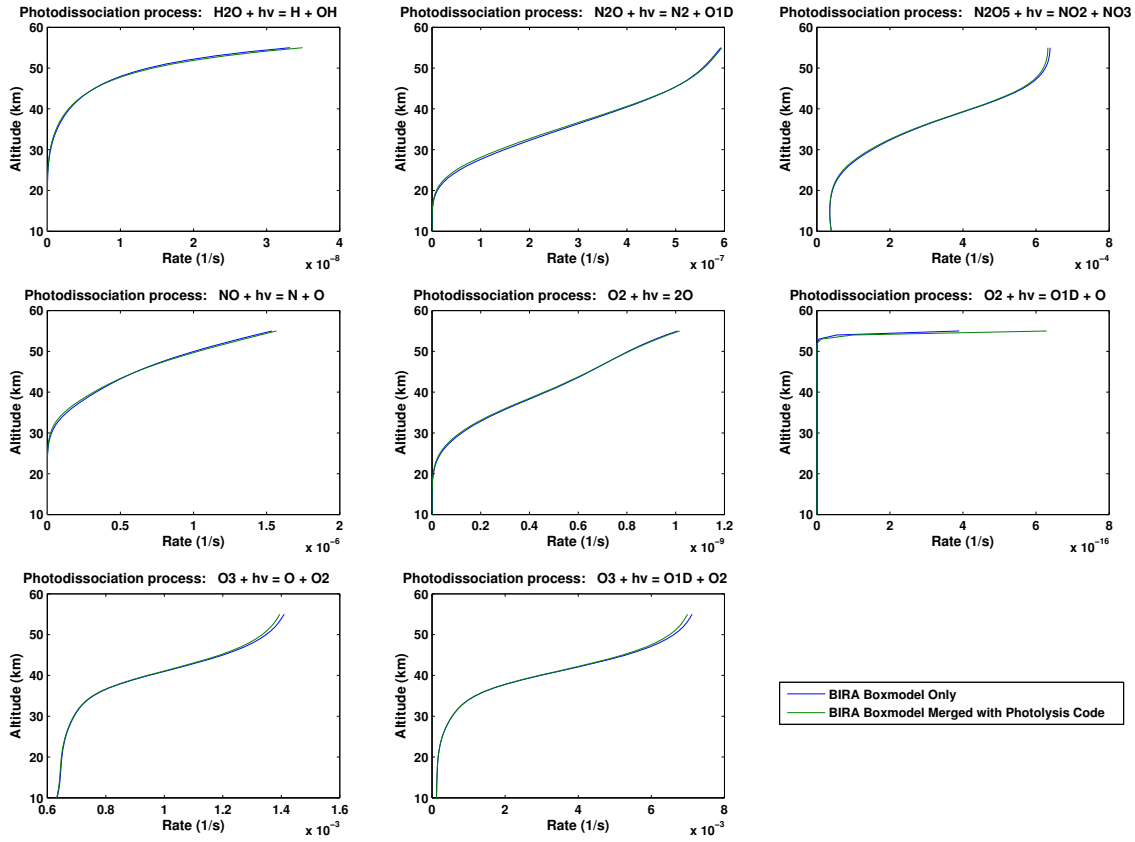

Figure 2.1: Comparison of photolysis rates calculated by the original BIRA box model using look-up tables (blue), and by the modified BIRA box model with on-line photolysis calculation and interactive absorbing gases (green).

between 0 - 10 km. Without these lower levels, including the surface, there is no reflection of the solar irradiation at the surface due to the Earth's albedo, and thus the photolysis rates are lower at all altitudes. To correct this, an artificial lower atmosphere is included in the modified BIRA model. Again, standard atmospheric concentrations are used for the absorbing gases in these lower levels, as well as standard atmospheric temperatures and pressures (MSIS).

As seen in Fig. 2.1, the addition of the artificial atmospheric levels result in accurate calculations of the photolysis rates (not all shown) by the modified BIRA model. Some of the photolysis rates are still slightly different than the ones taken from the look-up table, however the difference between them is always much less than 1 % (for all photolysis rates). Therefore, it can be concluded that the on-line

calculation of the photolysis rates are accurate and can now be used to investigate the effect of daily solar variability on stratospheric chemistry.

2.1.4 Optimization of Modifications

A chemistry-climate model (CCM) with on-line photolysis rate calculation is computationally expensive. Thus, it is necessary to make the photolysis calculations as efficient as possible. One way to do this with respect to the modifications is to limit the number of artificial atmospheric levels added. For the upper levels, photolysis rates are compared when adding 65, 13, 7, 5, 4, and 3 extra levels, corresponding to vertical spacings (between 55 - 120 km) of 1, 5, 10, 15, 20, 30, and 40 km respectively. For the lower levels, photolysis rates are compared when adding 10, 5, 2 and 1 extra levels, corresponding to vertical spacings (between 0 - 10 km) of 1, 2, 5, and 10 km respectively. The number of vertical levels necessary between 10 - 55 km, the area in which the chemistry is solved for, is also looked at. The photolysis rates are compared when using 46, 23, 10, and 5 levels, corresponding to vertical spacings of 1, 2, 5, and 10 km respectively.

Figures 2.2, 2.3, and 2.4 show that the results when using 4 upper levels is equivalent to using as many as 65, that using 5 lower levels is equivalent to using 10, and that using 10 levels between 10 - 55 km is nearly equivalent to using 46. Therefore to minimize computational time, the modified BIRA model used includes 4 upper atmospheric levels and 5 lower atmospheric levels. The lower levels are located at 0, 2, 4, 6, and 8 km, and the upper levels are located at 60, 80, 100, and 120 km. A 1 km spacing is kept between 10 - 55 km in order to provide more robust chemistry results.

2.1.5 BIRA-IGCM Model

In order to include dynamics, the modified BIRA box model is coupled to the Intermediate Global Circulation Model (IGCM) (*de F. Forster et al.*, 2000), a three-dimensional global circulation model (GCM). The BIRA-IGCM is a version of the

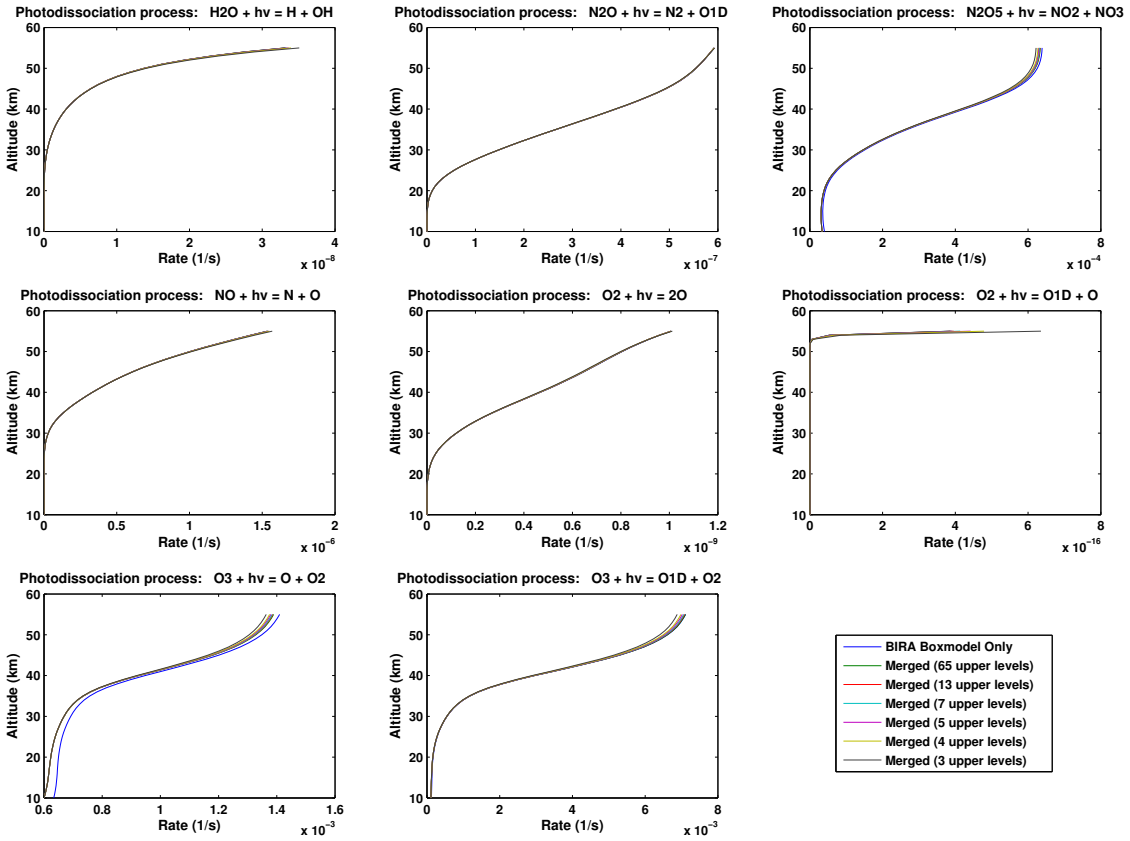

Figure 2.2: Comparison of photolysis rates calculated using the original BIRA box model (blue), and the modified BIRA box model with varying numbers of additional artificial upper (55 - 120 km) atmospheric levels. Rates are compared when using 65 (green), 13 (red), 7 (cyan), 5 (magenta), 4 (yellow), and 3 (black) artificial upper atmospheric levels.

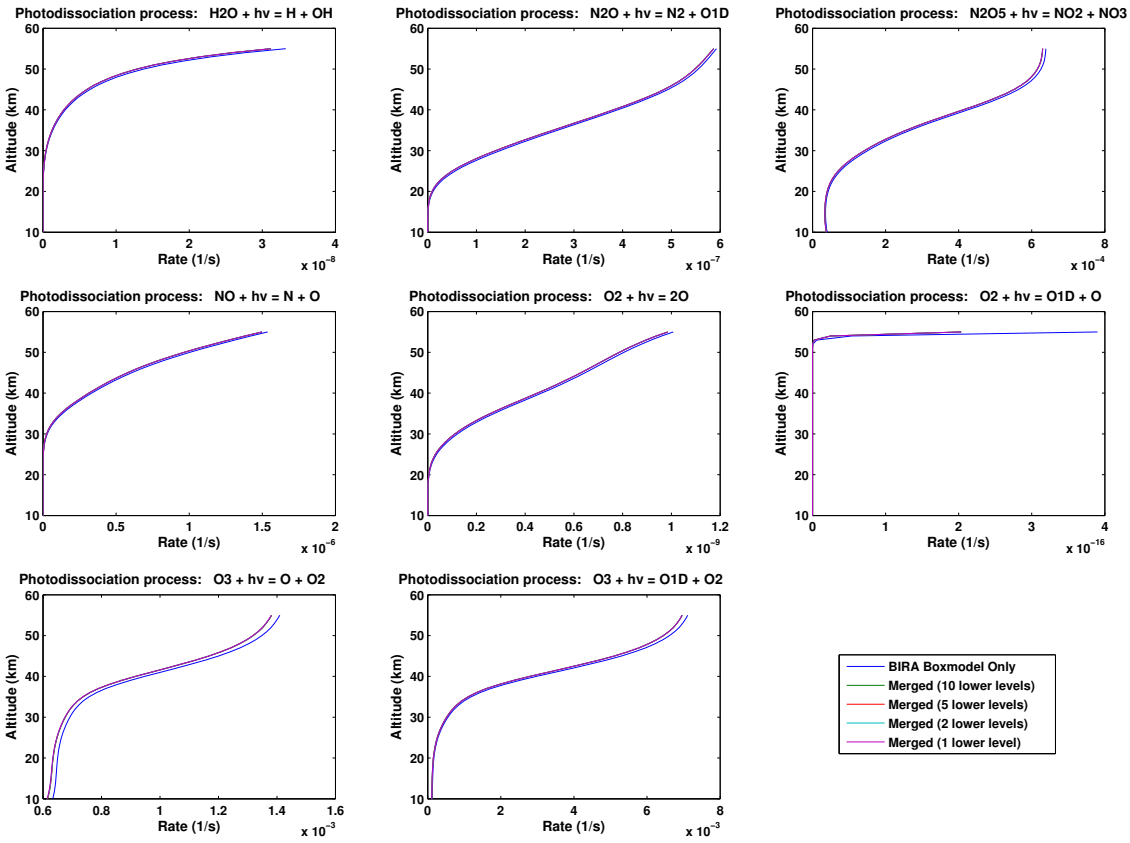

Figure 2.3: Comparison of photolysis rates calculated using the original BIRA box model (blue), and the modified BIRA box model with varying numbers of additional artificial lower (0 - 10 km) atmospheric levels. Rates are compared when using 10 (green), 5 (red), 2 (cyan), and 1 (magenta) artificial lower atmospheric levels.

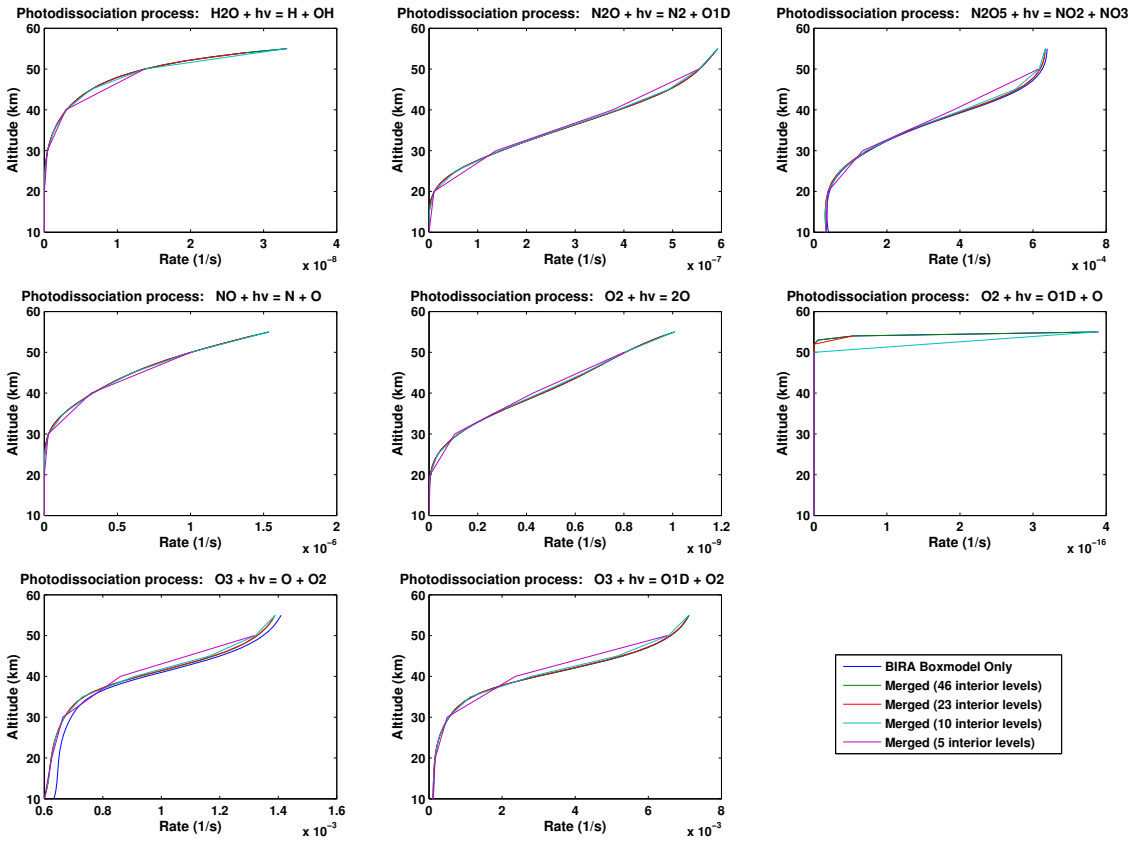

Figure 2.4: Comparison of photolysis rates calculated using the original BIRA box model (blue), and the modified BIRA box model with varying numbers of interior (10 - 55 km) atmospheric levels. Rates are compared when using 46 (green), 23 (red), 10 (cyan), and 5 (magenta) interior atmospheric levels.

IGCM-FASTOC which has been thoroughly used (*Taylor and Bourqui*, 2005; *Bourqui et al.*, 2005), where the FAst STratospheric Ozone Chemistry (FASTOC) scheme has been replaced with the BIRA box model by Andrew Ryzhkov, and the BIRA box model has been replaced with the modified BIRA box model with on-line photolysis calculation. The BIRA-IGCM has been successfully tested for gas-phase and heterogenous chemistry and the manuscript is in progress. The model runs at a T-31 resolution with 26 vertical levels, where half of the vertical levels are located in the stratosphere. The model has full radiation, surface and convective schemes, and has a good representation of planetary wave forcing of the stratospheric circulation. Currently, gravity waves are parameterized using Rayleigh friction in the 3 uppermost levels. The chemistry solver is the same as described in Sec. 2.1.1 and is solved for up to 1 hPa. The chemistry is solved for a full 24 hours, and then the family concentrations are advected according to the dynamics. The ozone is coupled to the photolysis rate calculation, but is currently un-coupled from the radiation scheme, where an ozone climatology is used to calculate the heating rates.

2.2 Description of Simulations

Using the modified BIRA box model, chemistry simulations are run in order to analyze the response of stratospheric chemistry to solar variability. A few important points are worth noting. First, there are no dynamics involved, and only the chemical response to solar variability is being analyzed. Therefore there is no change in temperature or pressure, and no transport of any of the chemical species. Without transport, there are no sources or sinks for any of the species involved. To account for this, all simulations are held to 10 days long, which corresponds to the time-scale during which an air parcel can be considered chemically isolated from its environment in the stratosphere. Also, all simulations start at midnight, occur in January, and are located at the equator. Again, since there are no dynamics, this only affects the initial conditions, sza, and the duration of the daily sunlight.

2.2.1 Constant Solar Irradiation

As a first step, the chemical response to various levels of constant solar irradiation is investigated. Three simulations using different constant solar irradiation are run. The simulations are run using identical initial conditions taken from the SLIMCAT three-dimensional chemical transport model (*Chipperfield*, 1999) and forced with either:

- solar maximum irradiation,
- solar minimum irradiation,
- or average solar irradiation.

2.2.2 Daily Solar Variability

The next step is to analyze the chemical response to random daily solar variability. A group of 200 ensemble members is run, each forced by a different solar variability. Solar irradiation is updated daily and held constant for 24 hours. Updates are at midnight to avoid a sudden change in the photolysis calculation. The solar variability

ranges between solar minimum and solar maximum, where the solar minimum and maximum values are provided by the same solar spectrum used to calculate the look-up table of photolysis rates (described in Sec. 2.1.2).

To incorporate solar variability, a pseudo-random number generator is used. A random sequence of 2000 numbers (200 members x 10 days each) is generated and then subdivided into 200 smaller sequences of 10 random numbers. These smaller sequences of random numbers are used as the solar variability forcing for each ensemble member. The random numbers are uniformly distributed and each solar variability forcing is independent of each other. Each random number (x_i) generated is between 0 and 1. Equation 2.1 is then used to calculate the solar irradiation to be used as the solar irradiation at the top of the model in the photolysis calculations:

$$I_i = x_i \times I_{max} + (1 - x_i) \times I_{min} \qquad x_i \in [0, 1], \tag{2.1}$$

where I_i is the solar irradiation, x_i is the random number (perturbation number), I_{max} is the maximum solar irradiation, and I_{min} is the minimum solar irradiation.

Therefore, a random number of 1 corresponds to using solar maximum irradiation, while a random number of 0 corresponds to using solar minimum irradiation. Since the random numbers are uniformly distributed, the expected value of the average forcing for an infinite size ensemble is 0.5, corresponding to average solar irradiation.

Note that it is not necessary to use a real solar variability forcing, as the purpose of this paper is to look at the basic chemical response to solar variability. By using a random solar variability it is also possible to examine the fundamental properties of the photo-chemistry. This is the first use of daily updated, random solar perturbations, and it allows for simulation of the chemical response to radiative output variations across the entire solar spectrum, over a large range of solar activity conditions. Note that all simulations are run using the same initial conditions as the constant solar irradiation experiments (Sec. 2.2.1).

2.2.3 Sensitivity to Initial Conditions

The previous experiments all use the same initial conditions, and are all run in January at the equator. However, chemical concentrations, temperatures, and pressures vary significantly when taking into consideration all latitudes, longitudes and seasons. Thus it is necessary to test the sensitivity of the chemical response to the initial conditions used. In order to do this, the initial conditions are perturbed, and the ensemble members are run again. One chemical species is perturbed at a time, and then 100 ensemble simulations forced by solar variability are run for each perturbation. The solar variability sequences used are the same as the first 100 of the 200 ensemble members used in the solar variability experiment (Sec. 2.2.2). The chemical species are perturbed from their globally and annually averaged concentrations. The concentration is either not perturbed, or perturbed by adding or subtracting two standard deviations, where the standard deviation is the global/annual standard deviation taken at each altitude. The sensitivity to perturbations in H_2O, NO_x, O_x, and temperature is tested. The average concentrations and standard deviations are taken from the SLIMCAT three-dimensional chemical transport model (*Chipperfield*, 1999) and can be seen in Fig. 2.5.

The above species are chosen to be perturbed as they pertain to the production and destruction of ozone. H_2O is chosen as it is a major source of HO_x, which can contribute to significant ozone destruction. NO_x is chosen as it also significantly contributes to ozone destruction. O_x is chosen to see if different regimes of ozone result in different responses to solar variability, and temperature is chosen due to the fact that many ozone destroying reactions are highly temperature dependent.

It is worth noting that different latitudes and seasons also affect the sza, as well as the length of day. This affects both the amount and duration of incoming solar irradiation, and sensitivity to this is addressed in the simulations described next in Sec. 2.2.4.

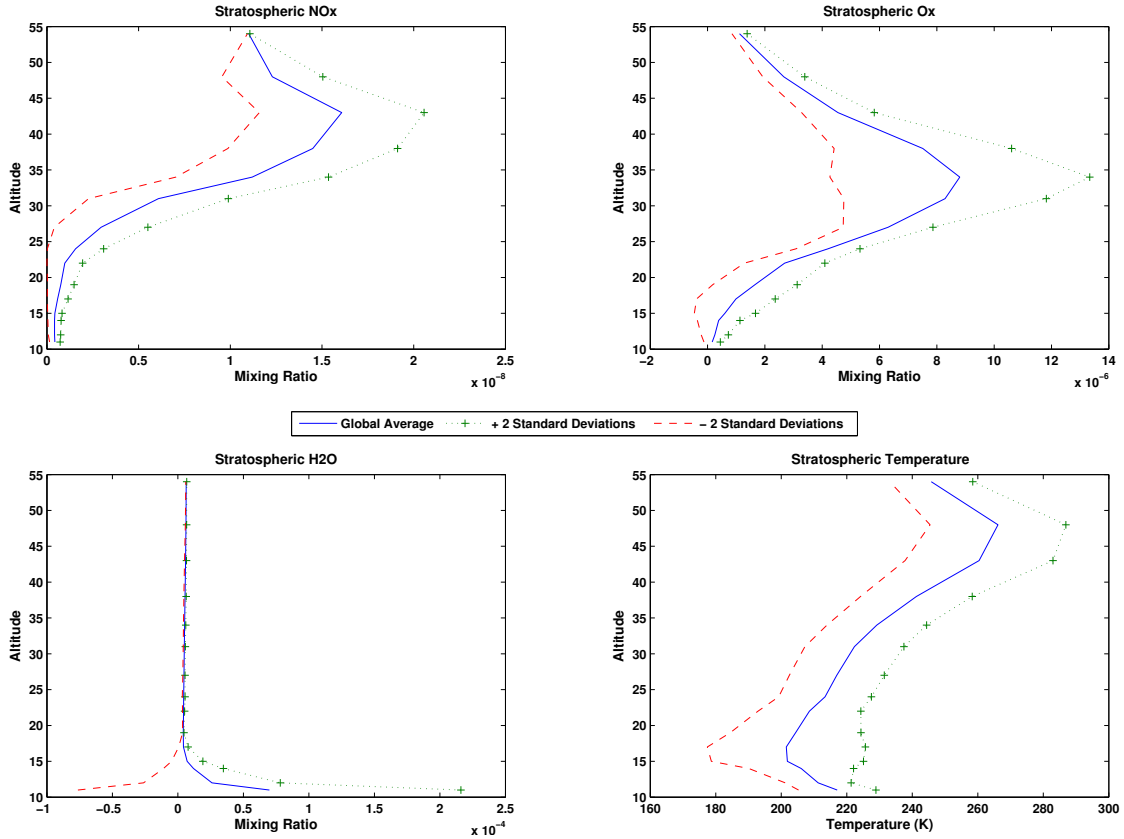

Figure 2.5: Statistics for stratospheric concentrations of NO_x (upper left), O_x (upper right) and H_2O (lower left), as well as stratospheric temperatures (lower right) used for initial condition perturbations. Each panel shows the global average (blue), as well as the global average $\pm$ 2 standard deviations (green plus signs for +, and red dashes for -). Statistics are taken from the SLIMCAT three-dimensional chemical transport model (*Chipperfield*, 1999).

2.2.4 BIRA-IGCM

Using the IGCM-BIRA model, simulations that include both chemistry and dynamics are run in order to further assess the impact of solar variability on stratospheric chemistry. Analysis of these simulations will help assess the impact of including dynamics, as well as the dependence on latitude and season. It is important to recall that the heating rates for the simulations are calculated using an ozone climatology, and hence are not interactive with the solar variability. This enables the ability to isolate the impact of including dynamics, and the possibility to isolate the impact of including interactive heating rates (and thus the temperature feedback described in 1.1) with future simulations.

Constant Solar Irradiation

Similarly to the chemistry-only simulations, the chemical response to various levels of constant solar irradiation is investigated. Two 5-year long simulations using different constant solar irradiation are run. One simulation is forced with solar minimum irradiation and the other with solar maximum irradiation. In order to minimize the amount of time needed for the stratospheric dynamics to adapt to the level of constant solar irradiation, each simulation is started from the end of a 5-year run at T-21 resolution that was forced with the corresponding constant solar irradiation.

Chapter 3

Results

All analysis is done for the following chemical families and chemical partitions: O_x, NO_x, HO_x, Cl_x, Br_x, $\frac{O}{O_x}$, $\frac{NO}{NO_x}$, $\frac{OH}{HO_x}$, $\frac{Cl}{Cl_x}$, and $\frac{Br}{Br_x}$. However, not all results are shown for each analysis for sake of briefness. The purpose of the analysis is to isolate and quantify the effects of solar variability on stratospheric chemistry.

3.1 Constant Solar Irradiation

3.1.1 Average Solar Irradiation

To investigate the effects of changing the overall constant solar irradiation, it is useful to first describe the average vertical distribution of chemical species. Figures 3.1 - 3.3 present the chemical evolution of the species over the 10 days for the solar average case.

O_x

From Fig. 3.1, it can be seen that O_x is present above 20 km and is most abundant at 30 km with a mixing ratio of approximately 9 ppmv, while significant O concentrations are present only above 47 km with a maximum partitioning ratio of 0.2 located around 55 km. The low values of the partitioning ratio of $\frac{O}{O_x}$ signifies that $[O_3] \sim [O_x]$, especially at altitudes lower than 42 km. There is a diurnal cycle evident

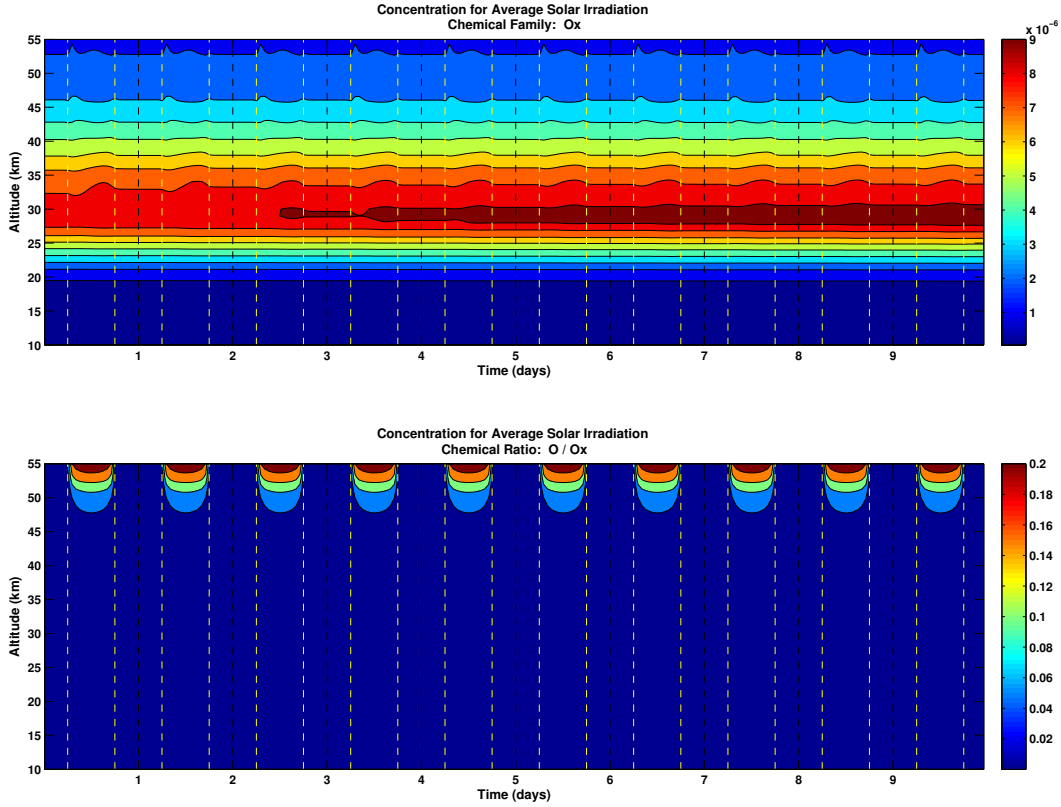

Figure 3.1: 10-day evolution of the volume mixing ratio of O_x (top) and of the partitioning ratio of $\frac{O}{O_x}$ (bottom). Results are taken from the average solar irradiation simulation. Dashed black lines represent midnight and dashed yellow lines represent 6 am and 6 pm.

in $\frac{O}{O_x}$, such that O is only present during the day when there is ample sunlight for the photolysis of O_2 (Re. 1.1) and photolysis of O_3 (Re. 1.5) to occur.

HO_x

In Fig. 3.2 it can be seen that both HO_x and $\frac{OH}{HO_x}$ follow a diurnal cycle, where HO_x (and hence OH and HO_2) is only present during the day when there is ample sunlight for the oxidation of water vapour (Re. 1.7), as well as the oxidation of CH_4 (both require $O(^1D)$ to occur). HO_x is found above 35 km with a maximum mixing ratio of 1.4 ppbv at 55 km, while the maximum in the partitioning ratio shows that about half of HO_x (55 %) is in the form of OH above 42 km. This partitioning is

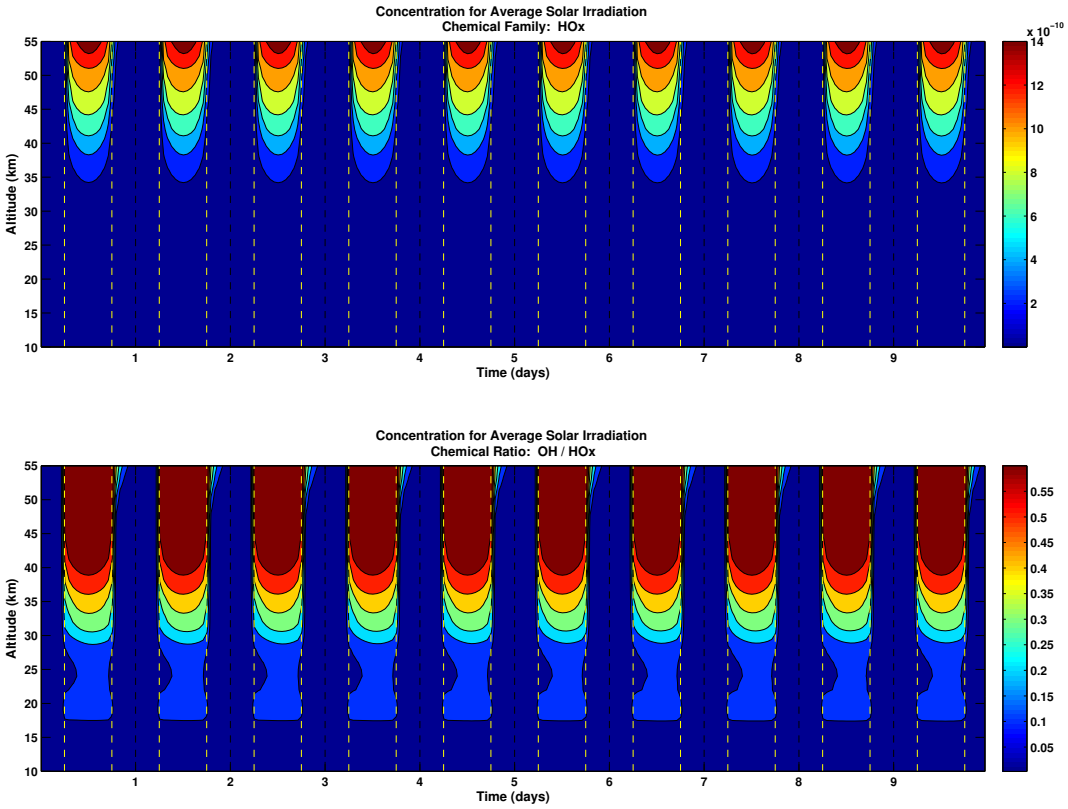

Figure 3.2: Same as Fig. 3.1 but for HO_x (top) and $\frac{OH}{HO_x}$ (bottom).

in agreement with the results from Brasseur's (1990) two-dimensional model of the middle atmosphere.

NO_x

Figure 3.3 shows that NO_x is present above 25 km with a maximum mixing ratio of 180 ppbv, while $\frac{NO}{NO_x}$ appears to be high throughout the column with maximum partitioning ratios of 0.9 at both 15 km and 45 - 55 km. In terms of NO concentration, the lower maximum can be ignored (negligible amounts of NO_x here), and NO is really only present above 30 km. A diurnal cycle is present in both NO_x and $\frac{NO}{NO_x}$. NO_x is more abundant during the day when photolysis converts NO_x reservoirs back into active NO_x through Re. 1.21 - 1.23, and $\frac{NO}{NO_x}$ is present only during the day when there is ample sunlight for the photolysis of NO_2 (Re. 1.15) and Re. 1.16 (requires O) to occur.

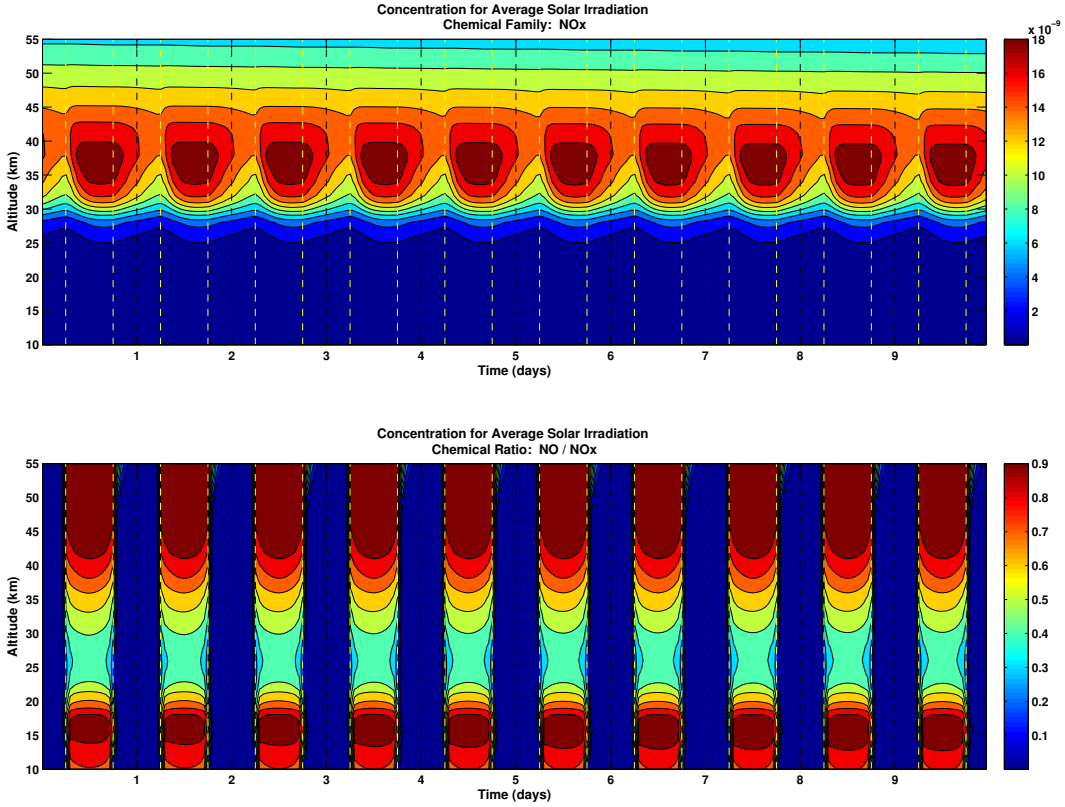

Figure 3.3: Same as Fig. 3.1 but for NO_x (top) and $\frac{NO}{NO_x}$ (bottom).

3.1.2 Difference Between Solar Minimum and Solar Maximum

The next step is to estimate the difference between the solar minimum case and the solar maximum case. Figures 3.4 - 3.6 present the percent difference between the concentrations in the solar minimum and the solar maximum runs, where the percent difference is given by:

$$\%\ Difference = 100 \times \frac{Concentration_{solarmax} - Concentration_{solarmin}}{Concentration_{solaraverage}}. \quad (3.1)$$

O_x

Figure 3.4 shows that the change in the amount of solar irradiation affects the vertical column above 25 km for O_x and above 45 km for $\frac{O}{O_x}$. The minimum-to-maximum difference for O_x occurs during both the day and night and builds to a peak difference of approximately 3 % around 40 km. This result is within the range of the minimum-to-maximum differences calculated from the observations by *Soukharev and Hood* (2006) and *Fioletov* (2009), and is in agreement with the largest minimum-to-maximum differences calculated from simulations by 1-D models (e.g., *Rozanov et al.*, 2002), 2-D models (e.g., *Haigh*, 1994) and CCMs (e.g., *Shindell et al.*, 1999; *Tourpali et al.*, 2003; *Egorova et al.*, 2004; *Rozanov et al.*, 2004). The increase in O_x during the solar maximum case is due to an increase in the abundance of O atoms available (enhanced photolysis of O_2), resulting in an increase in Re. 1.2. The peak difference occurs at 40 km due to the strength of the solar irradiation at this altitude. Even though the solar irradiation is stronger above 40 km, the response is not as strong due to the combination of a few factors. Above 40 km, the O_3 production (Re. 1.2) is not as strong due to the decrease in the air density, and due to the increase in O atoms, the Chapman termination mechanism (Re. 1.6) proceeds faster. Also, above 40 km, an abundance of HO_x (seen in Sec. 3.1.1) results in the destruction of O_x (through Re. 1.8 and 1.9), thus further limiting the response of O_x to solar irradiation above 40 km. Similar results are obtained for the upper stratosphere and mesosphere in simulations by 2-D models (e.g., *Brasseur*, 1993; *Khosravi et al.*, 2002) and CCMs

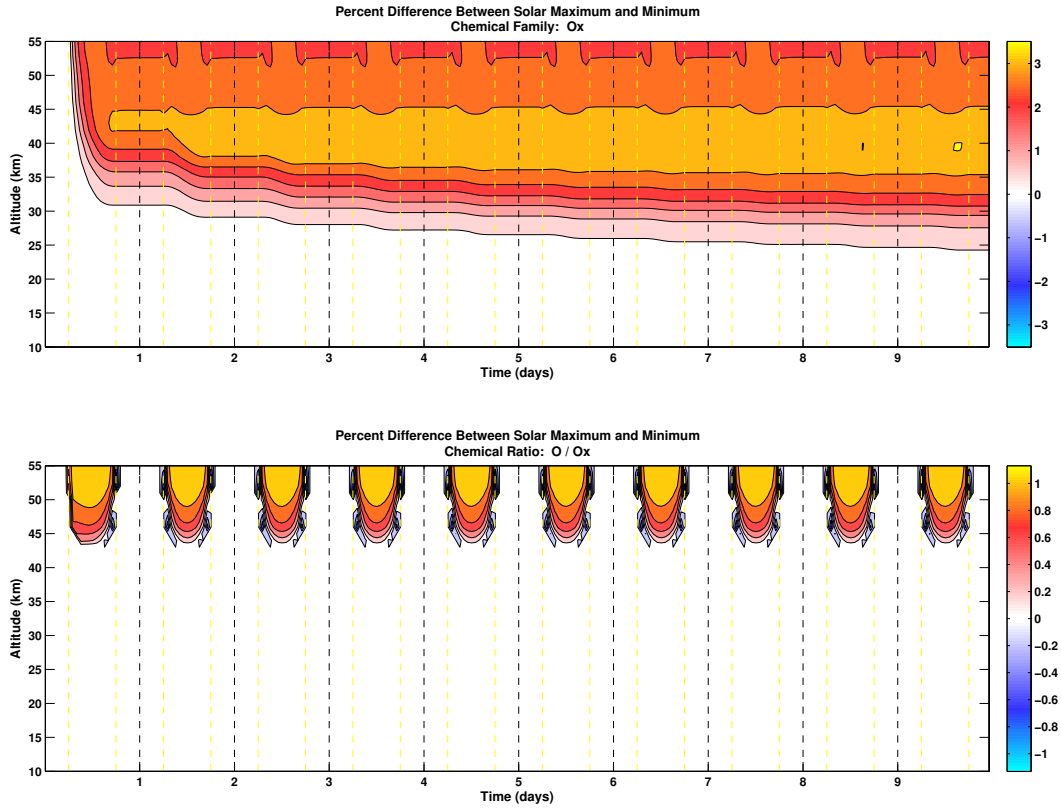

Figure 3.4: 10-day evolution of the percent difference in the volume mixing ratio of O_x (top), and the partitioning ratio of $\frac{O}{O_x}$ (bottom), between solar minimum and solar maximum simulations. Dashed black lines represent midnight and dashed yellow lines represent 6 am and 6 pm.

(e.g., *Egorova et al.*, 2005)), and in observations by *Zhou et al.* (1997). Since O is only present during the day, the minimum-to-maximum difference in $\frac{O}{O_x}$ only occurs during the day and peaks at approximately 1 % above 55 km. The peak difference for $\frac{O}{O_x}$ occurs at the highest altitudes in the model because this is where there is the largest amount of UV radiation allowing for Re. 1.1 to occur more strongly.

HO_x

In Fig. 3.5 it can be seen that the minimum-to-maximum difference for HO_x is positive and occurs mostly during the day above 35 km with a peak difference of approximately 3 % at 50 - 55 km. The peak occurs where the incoming solar irradia-

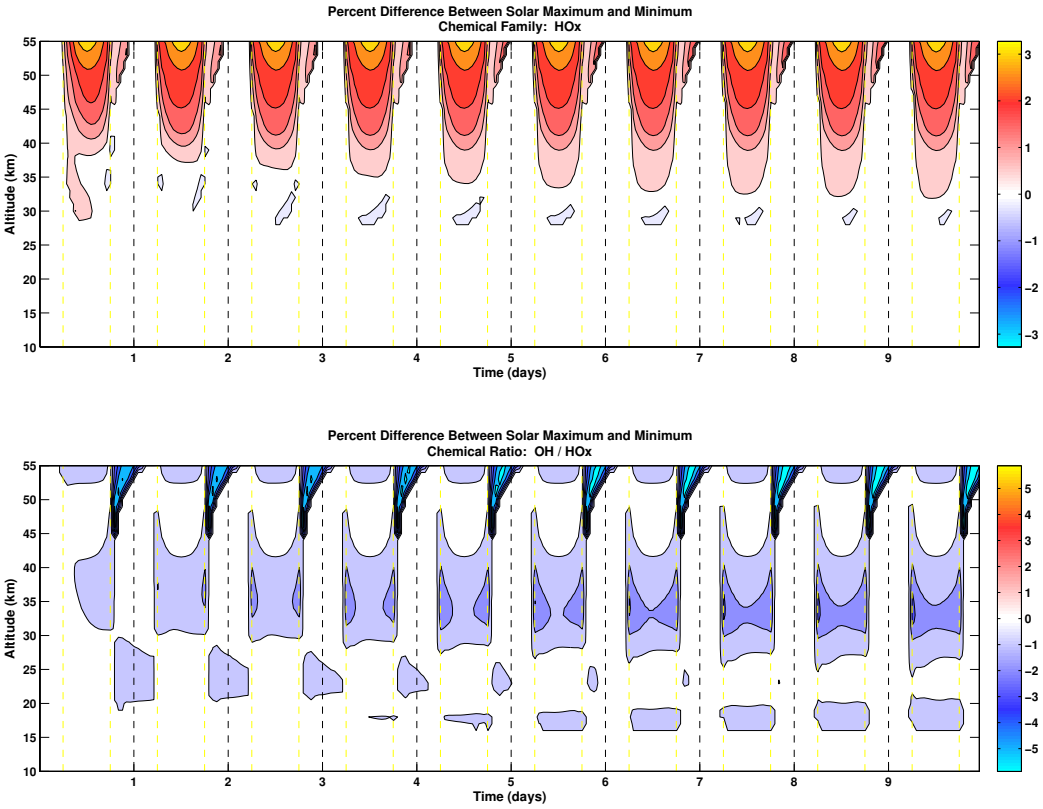

Figure 3.5: Same as Fig. 3.4 but for HO_x (top) and $\frac{OH}{HO_x}$ (bottom).

tion is strongest resulting in an increase in the photolysis of water vapour (Re. 1.7). A similar increase of HO_x during solar maximum is found in the CCM simulations of *Egorova et al.* (2005). In Fig. 3.5 the maximum difference (-6 %) in $\frac{OH}{HO_x}$ occurs only at the beginning of the night when there really is not much OH present. There is however a smaller negative difference in the partitioning ratio (2 %) located between 30 - 45 km. It is not well resolved here, but is looked at in greater detail in Sec. 3.2.2. Any decrease of $\frac{OH}{HO_x}$ during the day in the solar maximum case would likely be due to the fact that Re. 1.8 is faster than Re. 1.9 in the mid-stratosphere (*Dessler*, 2000), resulting in an enhanced conversion of OH to HO_2 due to the increase of O_x.

NO_x

Figure 3.6 shows both a positive and negative difference in minimum-to-maximum NO_x. The negative response during the daytime above 40 km can be attributed to

the increase in OH during solar maximum (seen previously in Fig. 3.5), resulting in an increase in the conversion of NO_x to its reservoir HNO_3 through Re. 1.20. A similar increase in HNO_3 during solar maximum is found in the CCM simulations of *Egorova et al.* (2005). The negative difference peaks occurring during the night in the upper stratosphere with peak differences slowly growing to -1.5 % at both 35 - 40 km and 50 - 55 km can not be attributed to OH. Less NO_x during the night in the solar maximum case at these altitudes occur due to the growing amount of O_x during solar maximum. The increase in O_x results in the increase of NO_3 (through Re. 1.18) which then converts more NO_x to its reservoir N_2O_5 through Re. 1.19. The positive minimum-to-maximum difference occurs during the day and grows to a peak difference of approximately 1 % between 25 - 30 km. The increase of NO_x during the day in the solar maximum case is due to an increase in the conversion of the reservoirs back into NO_x (Re. 1.21 - 1.23) due to enhanced photolysis. The minimum-to-maximum difference for $\frac{NO}{NO_x}$ is similar to the situation for $\frac{OH}{HO_x}$. The peak difference (-5 %) occurs during the beginning of the night when not much NO is present and there is a smaller negative difference in the partitioning ratio (< 1 %) that occurs during the day between 25 - 45 km. The minimum-to-maximum decrease in $\frac{NO}{NO_x}$ during the day would likely be due to an increase in Re. 1.13 due to an increase in O_x at these altitudes. This difference is looked at in greater detail in Sec. 3.2.2.

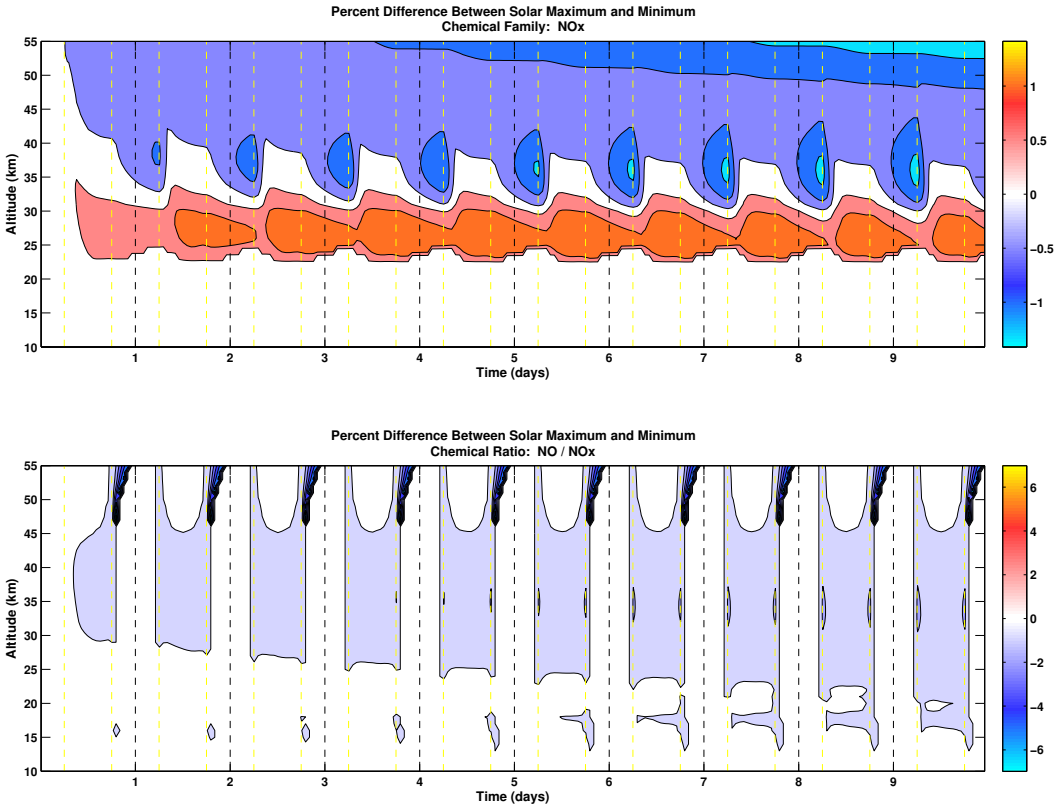

Figure 3.6: Same as Fig. 3.4 but for NO_x (top) and $\frac{NO}{NO_x}$ (bottom).

3.2 Solar Variability

Now that the differences in various constant solar irradiation have been looked at, it is time to investigate the effect of daily solar variability. Similarly to the constant solar irradiation analysis, it is important to first look at where the response to the solar variability occurs. Figures 3.7 - 3.9 present the standard deviation amongst the members. The figures also give an idea of the spread of possible responses to the daily solar variability.

O_x

Figure 3.7 shows that the ensemble members deviate from each other above 28 km for O_x and above 47 km for $\frac{O}{O_x}$. O_x members deviate during both the day and night, however the maximum deviations (0.1 ppmv) occur during the night at around 40 km. This is the same height that the peak minimum-to-maximum difference occurs at in Sec. 3.1.2. This represents a maximum deviation that is approximately 1 % of the average concentration of O_x at this altitude. The slightly larger deviations at night occur simply due to statistics. At noon, the ensemble members are in the middle of transitioning from one solar perturbation to another, and are statistically more likely to have less variance between them at that point than at night when their variance is attributed to a single solar perturbation. As expected for $\frac{O}{O_x}$, the members deviate from each other only during the day when sunlight is available. Also, the peak deviation in the partitioning ratio is 8×10^{-4} (~ 0.5 % of the average partitioning ratio of $\frac{O}{O_x}$) and occurs at the top of the model where the solar irradiation is strongest.

HO_x

Figure 3.8 shows that the HO_x members deviate from each during the day above 40 km, with a peak deviation of 0.014 ppbv (~ 1 %) at 55 km. The height of maximum deviation corresponds to the height of peak minimum-to-maximum difference seen in Fig. 3.5 (Sec. 3.1.2). For $\frac{OH}{HO_x}$, Fig. 3.8 shows the same signal as Fig. 3.5, with

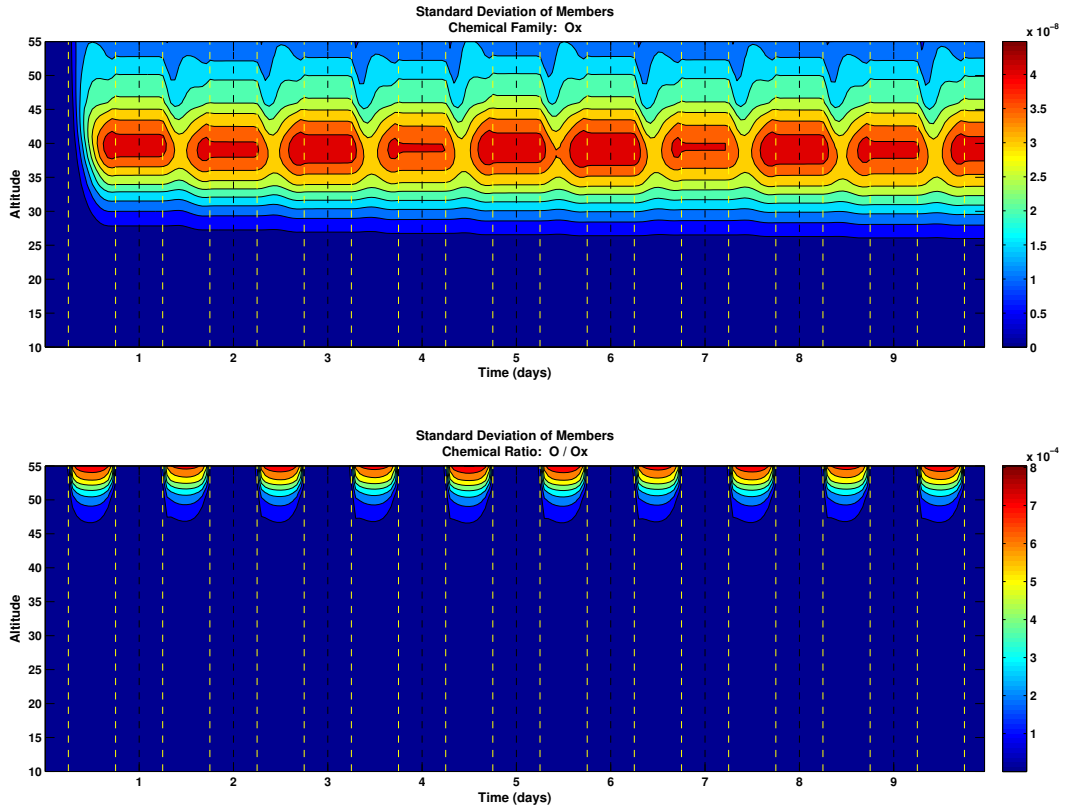

Figure 3.7: 10-day evolution of the standard deviation in the mixing ratio of O_x (top) and the partitioning ratio of $\frac{O}{O_x}$ (bottom) of the 200 ensemble members. Dashed black lines represent midnight and dashed yellow lines represent 6 am and 6 pm.

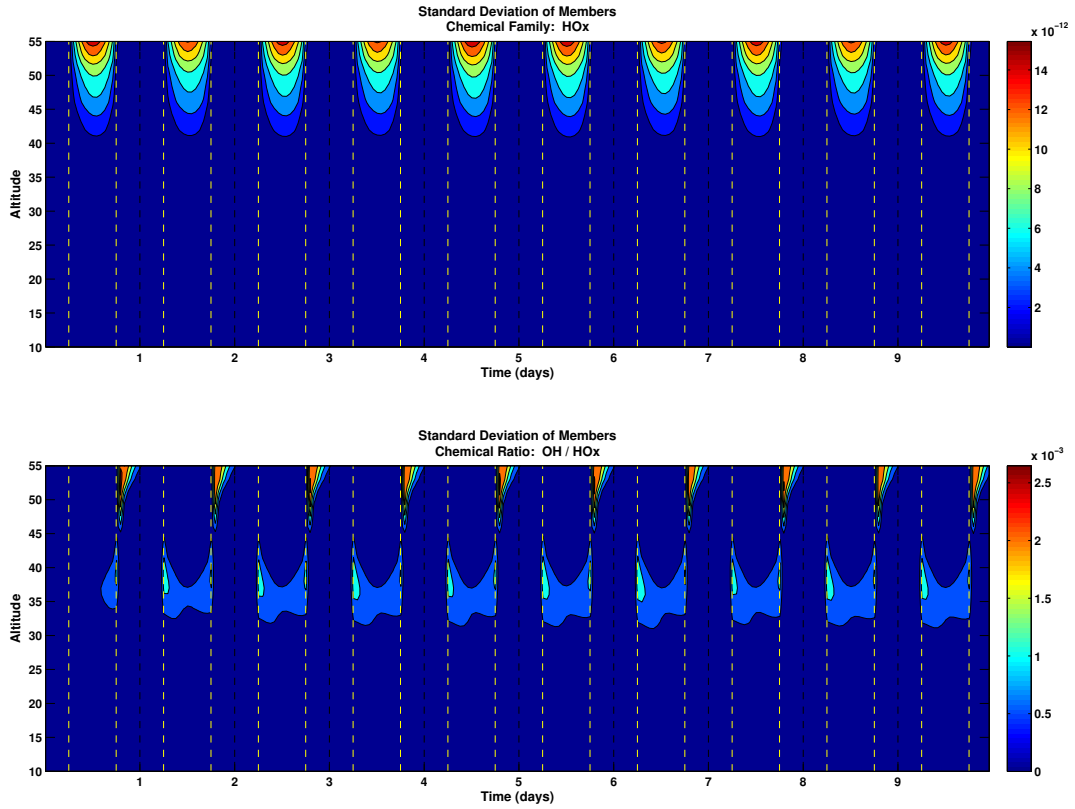

Figure 3.8: Same as Fig. 3.7 but for HO_x (top) and $\frac{OH}{HO_x}$ (bottom).

the largest deviations occurring at the beginning of the night (between 50 - 55 km). However, a deviation in the partitioning ratio of approximately 1×10^{-3} (~ 0.5 %) is also evident between 35 - 40 km during the day.

NO_x

In Fig. 3.9, it can be seen that the NO_x members deviate from each other during both the day (between 25 - 35 km) and night (between 35 - 45 km). These deviations correspond to the positive and negative responses seen in Fig. 3.6 and described in Sec. 3.1.2. The maximum deviation of 0.03 ppbv (~ 0.3 %) occurs during the day at 30 - 35 km, corresponding to the positive minimum-to-maximum difference. Again, the deviation for $\frac{NO}{NO_x}$ is similar to the situation for $\frac{OH}{HO_x}$. The maximum deviation in the partitioning ratio occurs at the beginning of the night. However, a more clear deviation of approximately 1×10^{-3} (~ 0.2 %) is seen between 30 - 45 km during

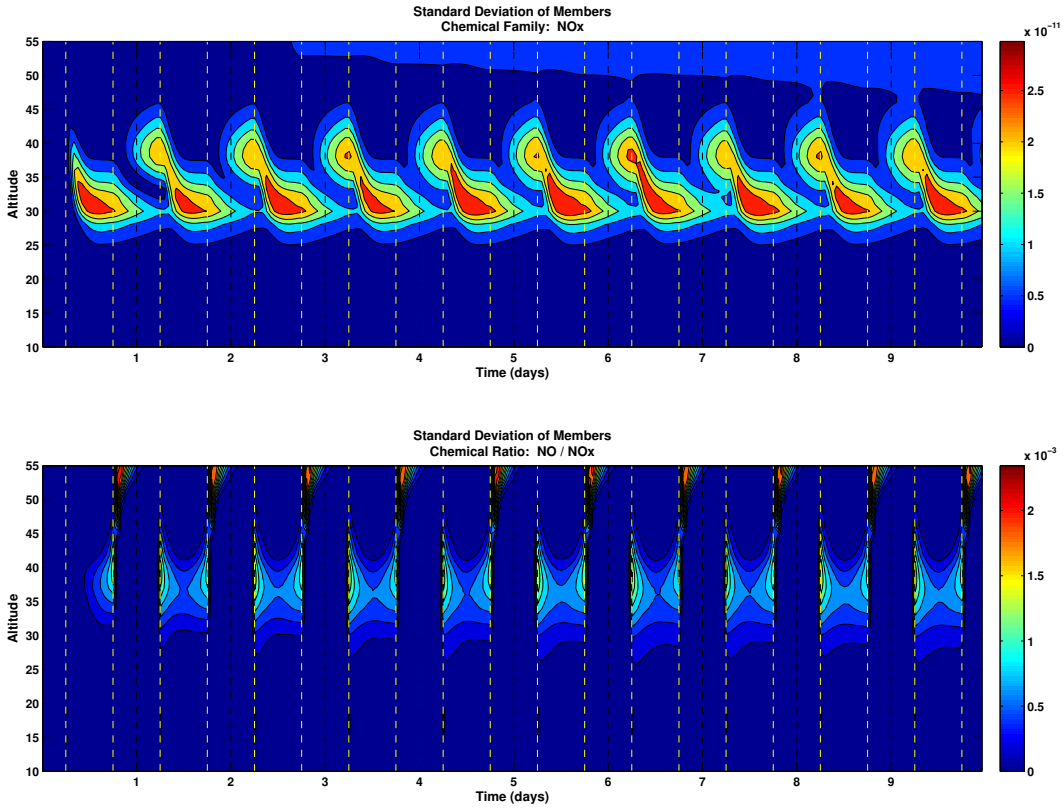

Figure 3.9: Same as Fig. 3.7 but for NO_x (top) and $\frac{NO}{NO_x}$ (bottom).

the day.

Multiple Linear Regression

To assess the effect of daily solar variability on stratospheric chemistry, a multiple linear regression is performed on the 200 ensemble members. The 'observed' or dependent variable (y) is taken as the daily (24 hour) average concentration of each ensemble member for days 3 - 9, resulting in a data set of 1400 'observations'. Day 1 is left out to allow for a spin-up to the experiment, and day 2 is left out as the concentration from the previous day is part of the spin-up. A separate regression is performed on the results from each day. This is done in order to ensure that the regression coefficients, and hence the effect does not change over time. The predictors or independent variables are taken as the current day's solar perturbation (x_1) and the previous day's daily average concentration (x_2). The dependence on the previous

day's daily average concentration is referred to as the memory. The multiple linear regression equation becomes:

$$y(t) = c' + a'x_1 + b'x_2 + r, \tag{3.2}$$

where $x_2(t) = y(t-1)$ and r is the residual. The regression coefficient a' gives the dependence of the chemical species on the current day's solar irradiation, and the regression coefficient b' gives the dependence on the previous day's concentration.

Since the observations and the predictor variables have scales of such different magnitudes, both the observations and the predictor variables are standardized before performing the regression analysis. The standardization is performed by subtracting the mean and dividing by the standard deviation, such that:

$$Y = \frac{y - \bar{y}}{\sigma_y},\ X_1 = \frac{x_1 - \bar{x_1}}{\sigma_{x_1}},\ and\ X_2 = \frac{x_2 - \bar{x_2}}{\sigma_{x_2}}, \tag{3.3}$$

where Y, X_1 and X_2 are the corresponding standardized variables. This results in the standardized variables having a mean of 0 and a standard deviation of 1. Also, the constant term in the equation goes to zero. By standardizing the variables, it allows for the determination of which variable has a greater relative effect on the dependent variable. The regression coefficients are standardized accordingly. The standardized regression coefficients can be related to the unstandardized coefficients by:

$$A = a'\frac{\sigma_{x_1}}{\sigma_y},\ B = b'\frac{\sigma_{x_2}}{\sigma_y},\ and\ R = \frac{r'}{\sigma_y}, \tag{3.4}$$

where A and B are the standardized coefficients, and R is the standardized residual.

When using standardized coefficients, it is important to remember that they relate to a change in a certain number of standard deviations of the observed variable. At certain heights in the column it is seen that the observed variable's standard deviation is negligibly small or zero. This means that even if the coefficient is non-zero at these altitudes, the response to the predictor variable is still in fact zero. Thus it is necessary to ignore these altitudes. As a reminder of this, the levels of the column with standard deviations less than 5 % of the maximum deviation are hatched out on all further plots.

3.2.1 Regression Coefficients

Figures 3.10 - 3.15 present the regression coefficients, mean concentration, and the standard deviation of the members for each day. The correlation coefficient (R^2) is also included to determine how well the linear model fits the data. Recall that the regression coefficients are standardized, thus they can only be used to give an idea of where the solar irradiation and the memory are important within the vertical column and can not directly give the magnitude of the response. The mean concentration and standard deviation of the members is included to help give insight to the overall effect.

O_x

Figure 3.10 confirms that the constant or intercept term is zero throughout the column. This result is the same for all species. The correlation coefficient for O_x is very close to 1 for the entire column, showing that the linear model is indeed a good fit. The vertical profile of the mean concentration of the members shows the same peak at 30 km as the constant average solar irradiation case seen in Fig. 3.1. The mean concentration of the members is similar to the constant average solar irradiation case for all species and is not discussed any further. From the regression coefficients for O_x, it appears that solar irradiation is dominant in the upper stratosphere (above 40 km) where the solar irradiation is strongest, and memory is dominant in the lower stratosphere (below 35 km) where chemical life-times of O_x are longer. Both the solar irradiation and the memory are positively correlated with the O_x concentration. The regression coefficients do not differ much from day to day and therefore the effect of the solar variability does not change significantly with time as the concentrations of the species evolve. Recall that the magnitude of the response depends on the standard deviation of O_x which peaks at 40 km. The magnitude of the response to solar irradiation and to the memory is discussed later in Sec. 3.2.2.

For $\frac{O}{O_x}$, Fig. 3.11 shows that the correlation coefficient is 1 above 45 km, where the standard deviation is large enough such that the response is non-negligible. The regression coefficients show that solar irradiation is dominant above 45 km and that

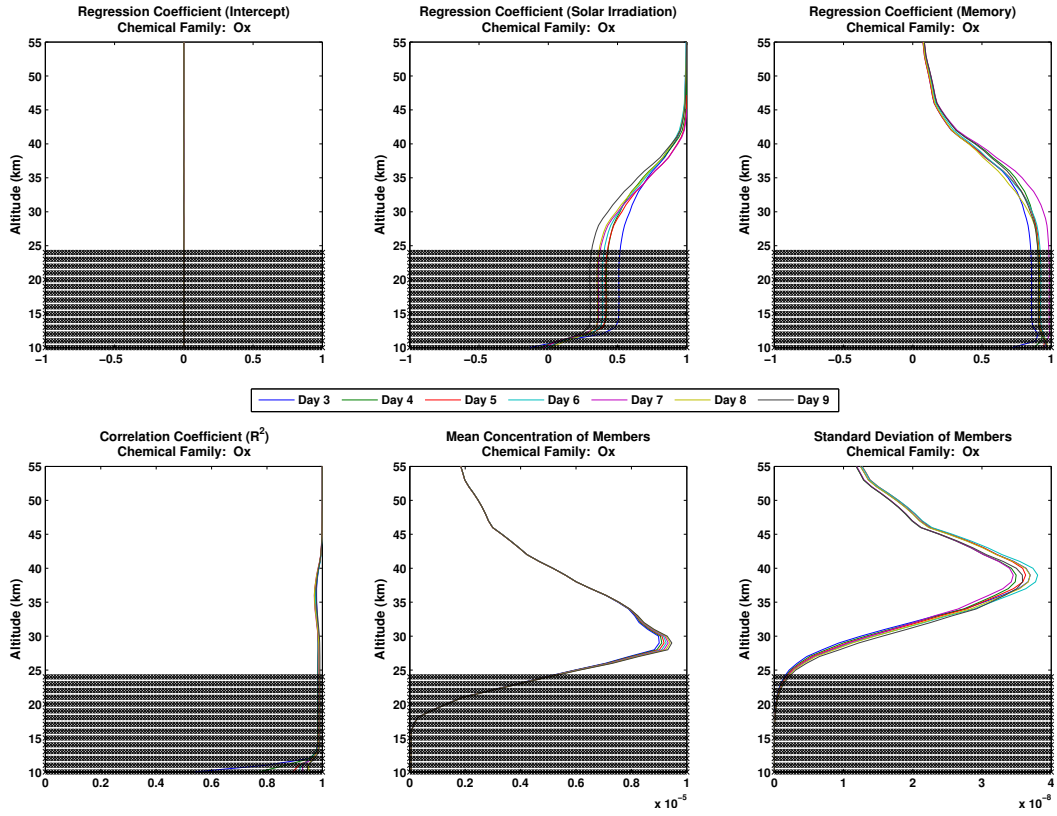

Figure 3.10: Standardized regression coefficients, correlation coefficient (bottom left), mean concentration (bottom middle) and standard deviation (bottom right) of the 200 ensemble members for O_x. Standardized regression coefficients consist of a constant term (top left), solar irradiation coefficient (top middle) and memory coefficient (top right). Results are shown for days 3 - 9. Hatched out areas represent altitudes at which the response is negligible (standard deviation of less than 5 % of the maximum).

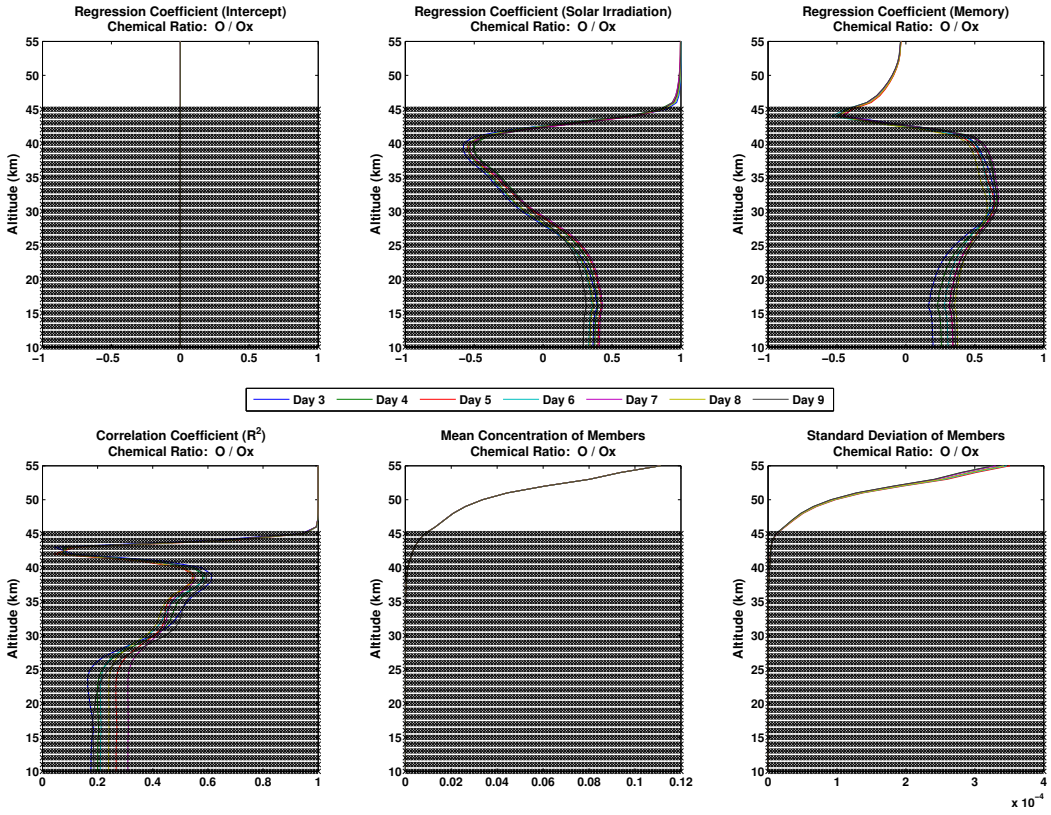

Figure 3.11: Same as Fig. 3.10 but for the partitioning ratio of $\frac{O}{O_x}$.

the memory is negligible for $\frac{O}{O_x}$. This is due to the abundance of sunlight and the short life-time of O at such high altitudes. Solar irradiation is correlated with $\frac{O}{O_x}$ and the strongest response is expected to occur at 55 km where the standard deviation peaks. For $\frac{O}{O_x}$, the regression coefficients show negligible change throughout the days.

HO_x

As was the case for O_x, Fig. 3.12 shows that the correlation coefficient for HO_x is 1 everywhere there is a non-negligible response. The regression coefficients illustrate that the solar irradiation is the dominant factor, due to the short life-times and the abundance of sunlight at such high altitudes. Also, the solar irradiation is correlated with the HO_x concentrations, and the largest response is expected to occur at the top of the model. Again the regression coefficients show negligible change throughout

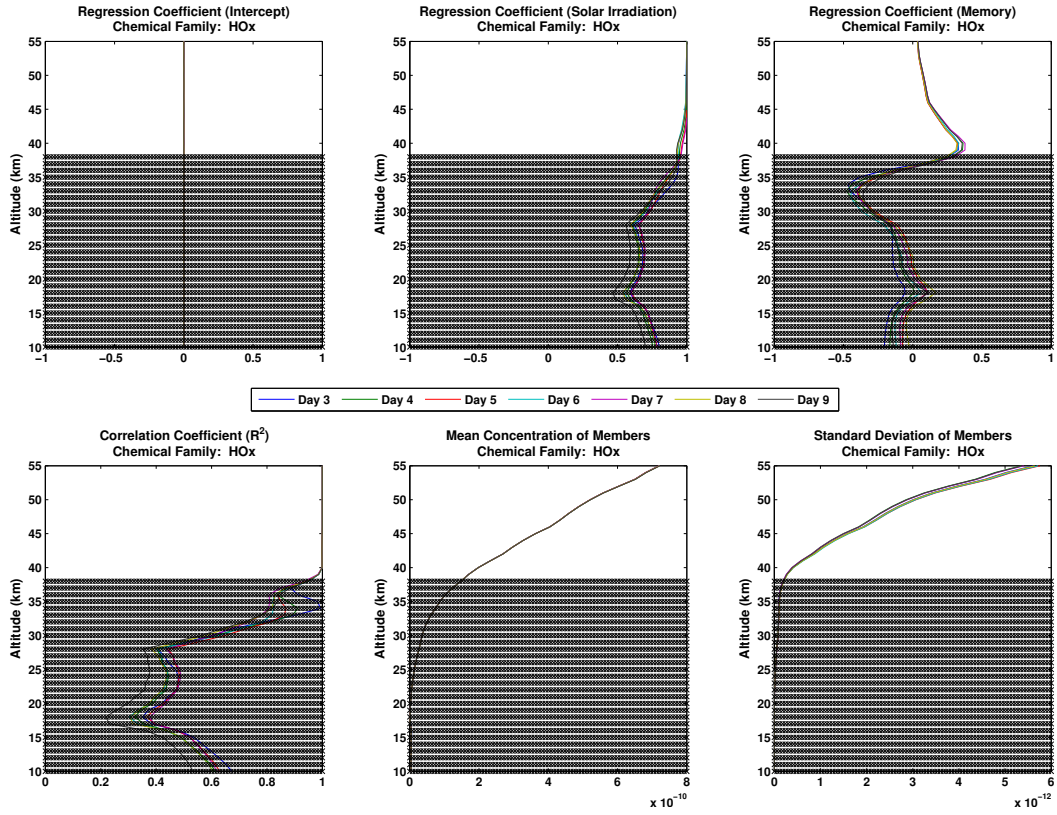

Figure 3.12: Same as Fig. 3.10 but for HO_x.

the different days.

It can be seen in Fig. 3.13 that $\frac{OH}{HO_x}$ has many non-linearities, as the correlation coefficient is less than 1 almost everywhere with minimums at 48 km ($R^2 = 0.6$), 32 km ($R^2 = 0.4$) and 43 km ($R^2 = 0$). The regression coefficients for $\frac{OH}{HO_x}$ do not appear to be as clear as for O_x and appear to change multiple times throughout the vertical column. However, it is only important to focus above 50 km and between 30 - 40 km where the standard deviations are large enough. Above 50 km, solar irradiation is the dominant factor and is anti-correlated. Between 30 - 40 km both solar irradiation and memory appear to be equally important, with solar irradiation anti-correlated and memory correlated. Similarly to O_x, the regression coefficients for $\frac{OH}{HO_x}$ do not show a significant change throughout the days.

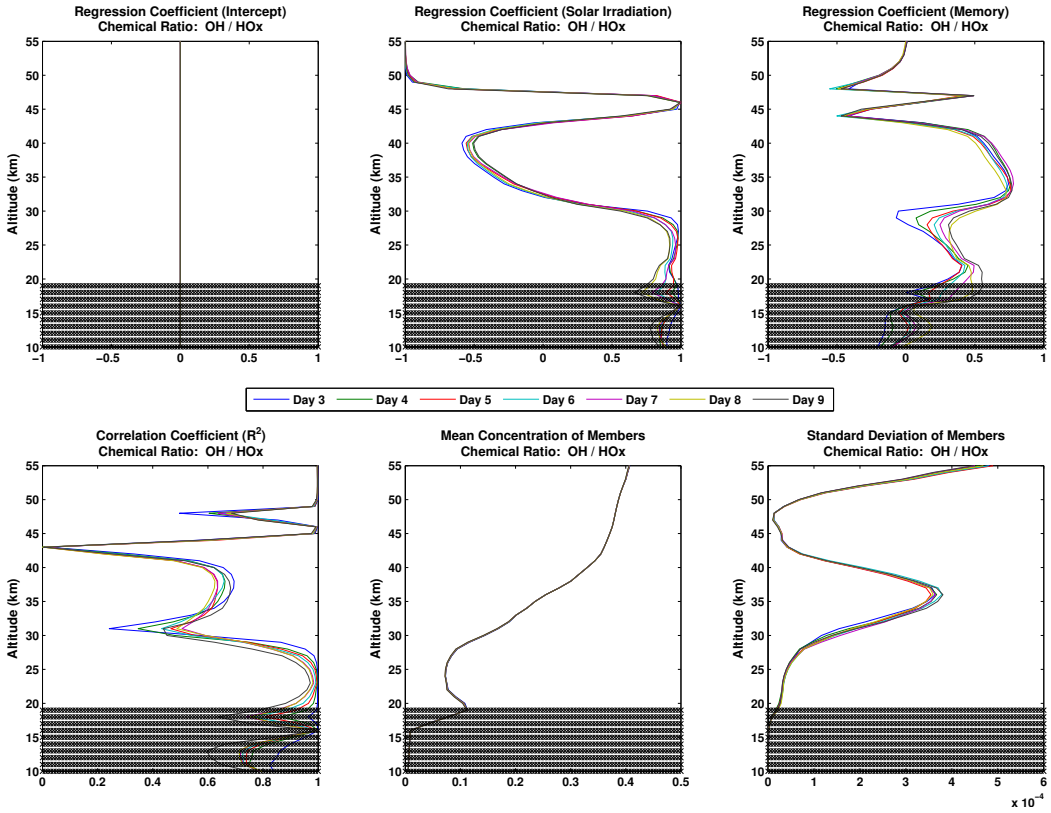

Figure 3.13: Same as Fig. 3.10 but for the partitioning ratio of $\frac{OH}{HO_x}$.

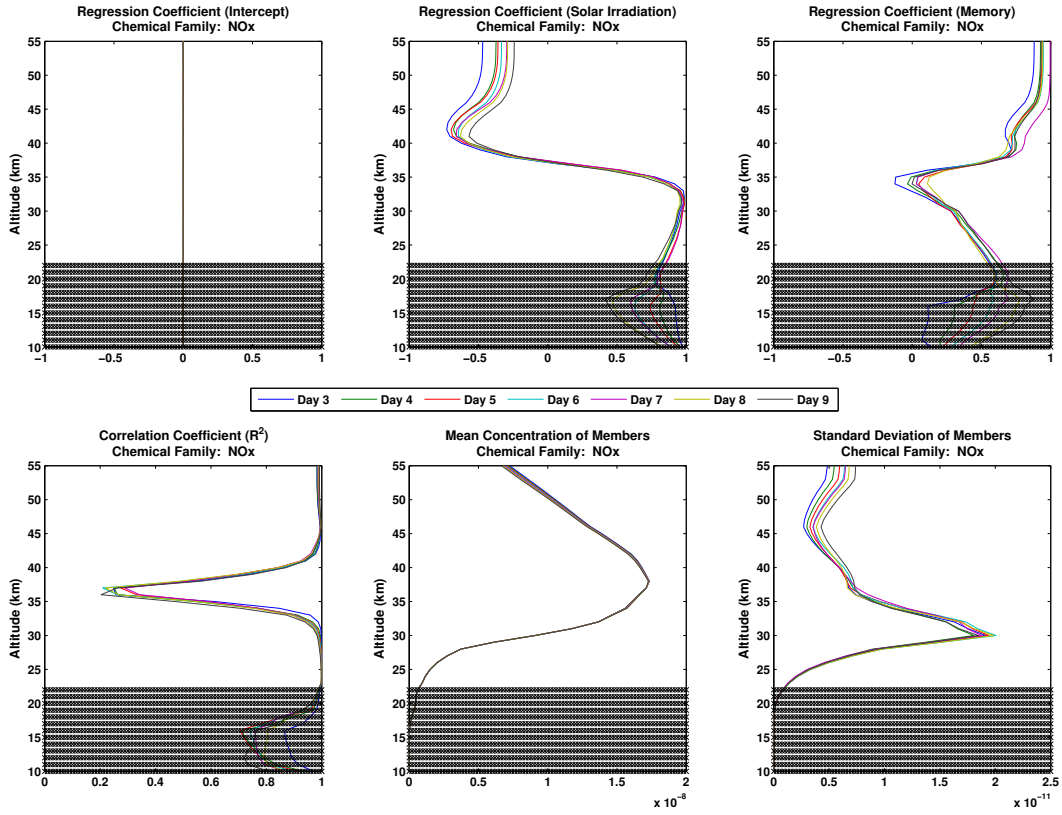

Figure 3.14: Same as Fig. 3.10 but for NO_x.

NO_x

In Fig. 3.14, it can be seen that the correlation coefficient for NO_x is not equal to 1 everywhere. It dips to approximately 0.3 between 35 - 38 km and thus there is expected to be a significant residual at this height (discussed later in Sec. 3.2.3). It appears that for NO_x, the solar irradiation effect is slightly stronger in the lower stratosphere (below 35 km) while memory is slightly stronger above 40 km. The solar irradiation is anti-correlated above 37 km and correlated below 35 km, while the memory is correlated pretty much throughout the column. Due to the peak in the standard deviation, the strongest response is expected to occur between 30 - 35 km. Again, the regression coefficients show an insignificant change over the different days.

Figure 3.15 shows that the correlation coefficient for $\frac{NO}{NO_x}$ is less than 1 below 45 km with a minimum value of approximately 0.4 at 30 km. This suggests that

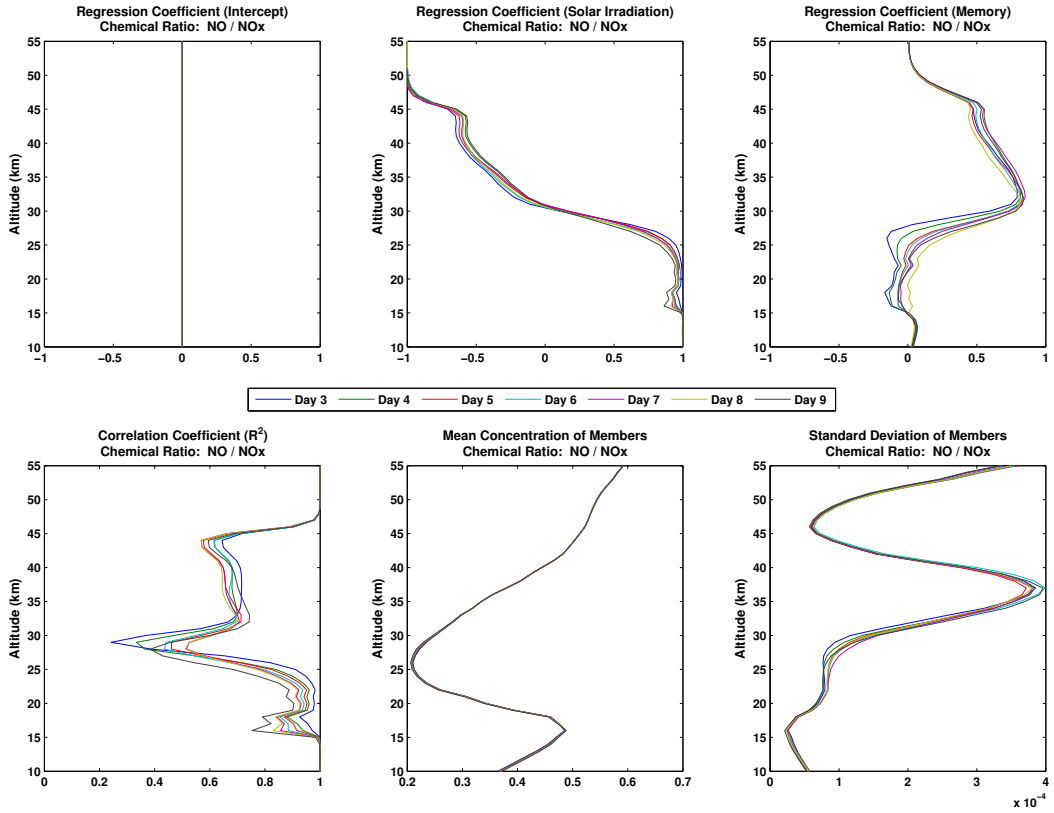

Figure 3.15: Same as Fig. 3.10 but for the partitioning ratio of $\frac{NO}{NO_x}$.

there is a residual present and it should be strongest at 35 km. The memory appears to be slightly more important between 30 - 40 km, whereas solar irradiation is more important throughout the rest of the column. In fact, the memory has no effect either above 50 km or below 25 km. The memory is correlated throughout, while solar irradiation is anti-correlated above 32 km and correlated below. Peak responses are expected to occur at altitudes of 50 - 55 km and 35 - 40 km. Once again, the regression coefficients for $\frac{NO}{NO_x}$ show an insignificant change throughout the simulation.

3.2.2 Partial Residuals

In order to assess the magnitude of the effect of each predictor variable, partial residuals are plotted. The partial residuals are calculated by:

$$\psi_s = AX_1 + R, \tag{3.5}$$

$$\psi_m = BX_2 + R, \tag{3.6}$$

and are plotted against X_1 and X_2 respectively, where ψ_s is the partial residual for the solar irradiation and ψ_m is the partial residual for the memory. Plotting the partial residuals allows for the isolation of the effect of one predictor variable by removing the effect of the other predictor variables. The plots for the dependence on solar irradiation (Fig. 3.16, 3.18, and 3.20) present the change in concentration versus the current day's solar perturbation. The plots for the dependence on memory (Fig. 3.17, 3.19, and 3.21) present the change in concentration versus the previous day's solar perturbation. Similar effects are seen for all days, so the results here are presented for one day only. Keep in mind that a solar perturbation factor of 0 means solar minimum and a factor of 1 means solar maximum.

O_x

Figure 3.16 presents the response of O_x and $\frac{O}{O_x}$ to the current day's solar irradiation. The responses for both O_x and $\frac{O}{O_x}$ are correlated with solar irradiation. This means that a stronger solar irradiation results in larger concentrations and vice versa. The strongest responses always occurs at either the solar maximum or solar minimum perturbation, so to simplify the analysis, only solar maximum perturbation responses are discussed (as the solar minimum perturbation responses are simply the opposite). For O_x, the strongest response is a change of 0.06 ppmv located at 40 km. The strongest response occurs at this altitude due to the chemistry described previously in Sec. 3.1.2. For $\frac{O}{O_x}$, the strongest response is a change in the partitioning ratio of 5×10^{-4}. The largest response for $\frac{O}{O_x}$ occurs at the top of the model as this is where the incoming solar irradiation is strongest. Recall that these responses are only due to the current day's solar perturbation and that a solar perturbation on one day can have an effect on the next day's concentrations as well. This is the next topic of discussion.

The effect on the next day's concentration is seen in Fig. 3.17. For O_x, the memory response is correlated, and the strongest response is 0.04 ppmv at approximately 35 km. Note that this response is only a little bit smaller in magnitude and slightly

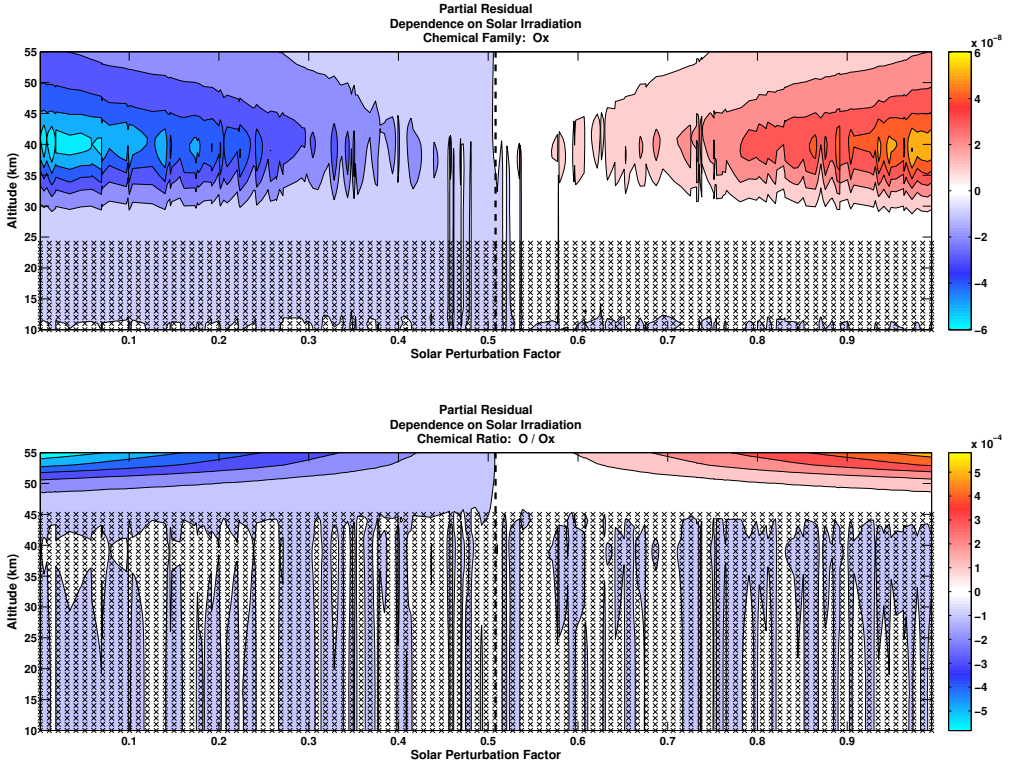

Figure 3.16: Solar irradiation dependence (partial residual) of O_x (top) and the partitioning ratio of $\frac{O}{O_x}$ (bottom) to the current day's solar irradiation. Dependence reflects a change in the mixing ratio (top) or in the partitioning ratio (bottom) and is plotted against the current day's solar perturbation. Dashed black line represents the average solar perturbation of the 200 ensemble members. Hatched out areas represent altitudes at which the response is negligible (standard deviation of less than 5 % of the maximum).

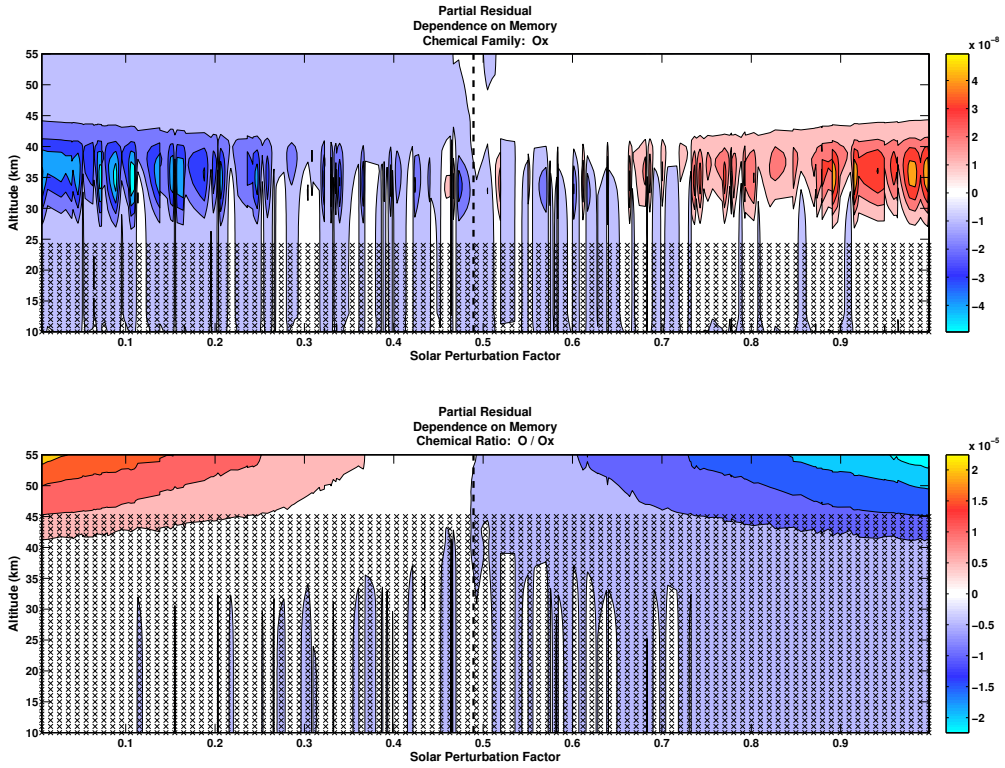

Figure 3.17: Memory dependence (partial residual) of O_x (top) and the partitioning ratio of $\frac{O}{O_x}$ (bottom) to the previous day's solar irradiation. Dependence reflects a change in the mixing ratio (top) or in the partitioning ratio (bottom) and is plotted against the previous day's solar perturbation. Dashed black line represents the average solar perturbation of the 200 ensemble members. Hatched out areas represent altitudes at which the response is negligible (standard deviation of less than 5 % of the maximum).

lower in altitude than that of the response to the current day's solar perturbation. The location is shifted downward due to the increase in the life-time of O_x with decreasing altitude. In other words, the carry-over effect (or memory) of the previous day's increase in solar irradiation is still found (only slightly attenuated and a little bit lower in altitude) on the next day. The response for $\frac{O}{O_x}$ is anti-correlated, but is negligibly small compared to the current day's solar perturbation response as is suggested from the regression coefficients in Fig. 3.11 (Sec. 3.2.1).

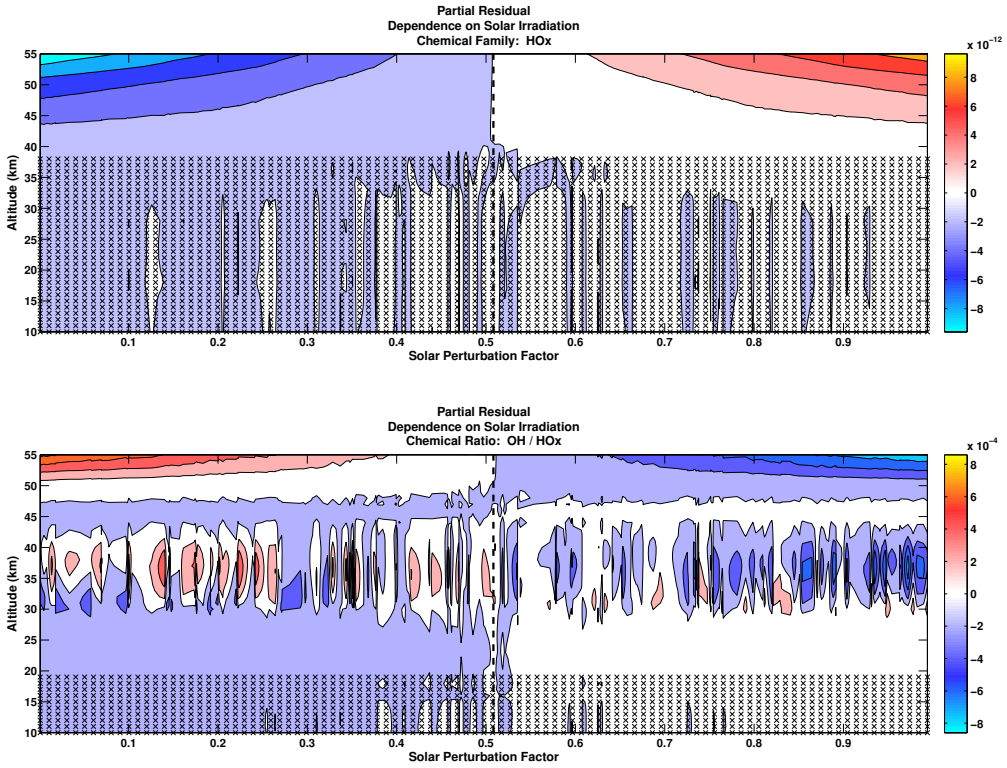

Figure 3.18: Same as Fig. 3.16 but for HO_x (top) and $\frac{OH}{HO_x}$ (bottom).

HO_x

In Fig. 3.18, it can be seen that the response of HO_x to the current day's solar perturbation is correlated and the strongest response is a change of 0.008 ppbv at the top of the model. The peak change occurs at the top of the model as the solar irradiation is strongest here allowing for an increase in the oxidation of water vapour (Re. 1.7). For $\frac{OH}{HO_x}$, the response is anti-correlated with the strongest response being a change in the partitioning ratio of - 8×10^{-4} at the top of the model. In the upper stratosphere, Re. 1.11 dominates the conversion between OH and HO_2 (*Dessler*, 2000). The increase in O at the top of the model (seen in Sec. 3.2.2) causes Re. 1.11 to be faster, resulting in a decrease in the partitioning ratio of $\frac{OH}{HO_x}$. There is a smaller and less clear change in the partitioning ratio of - 5×10^{-4} between 35 - 40 km. This is due to the enhanced conversion of OH to HO_2 through an increase in Re. 1.8 (described in Sec. 3.1.2).

Figure 3.19 corroborates with the regression coefficients for HO_x (Sec. 3.2.1), as

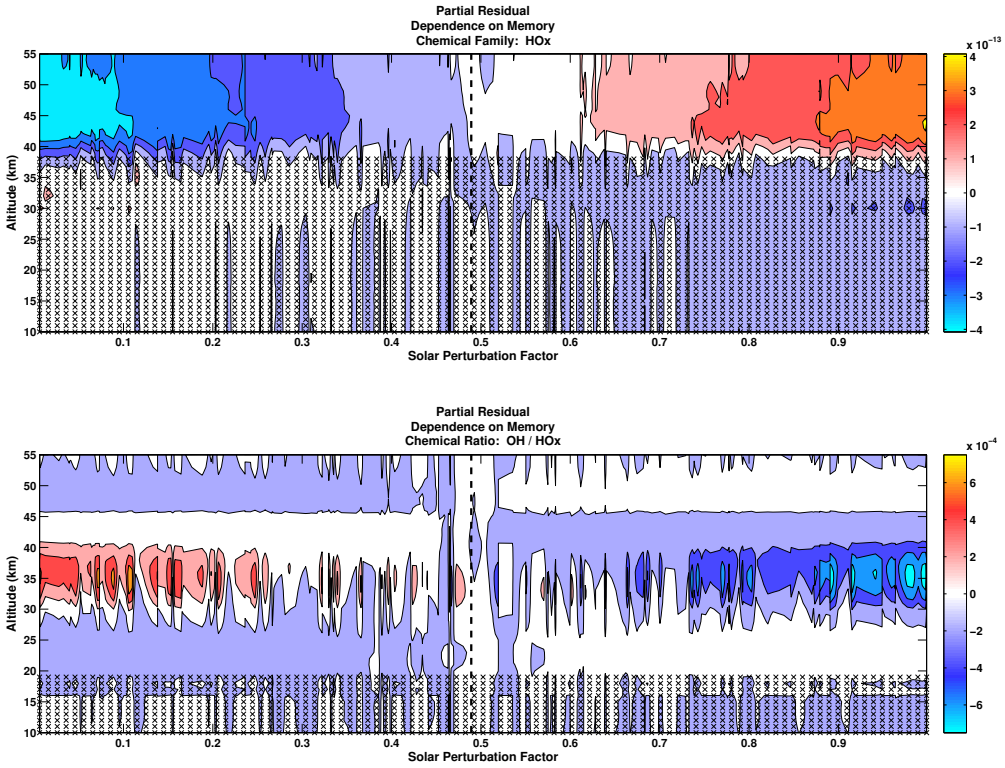

Figure 3.19: Same as Fig. 3.17 but for HO_x (top) and $\frac{OH}{HO_x}$ (bottom).

the response to the memory is more than a magnitude smaller than the response to the current day's solar perturbation. For $\frac{OH}{HO_x}$, the response to memory is anti-correlated with the largest change in the partitioning ratio being - 6×10^{-4} between 35 - 40 km, and is due to the same chemistry as the solar irradiation response at this altitude.

NO_x

Figure 3.20 shows that the response for NO_x to the current day's solar perturbation is positively correlated and the peak response is a change of 0.03 ppbv just above 30 km. The strongest response is located at this altitude due to the life-time of HNO_3 at this altitude. At 30 km, the life-time of HNO_3 is approximately 1 day (*Dessler*, 2000). Thus with stronger photolysis of HNO_3 (Re. 1.22), the life-time decreases (to less than 1 day) and more NO_x is produced than when the solar irradiation is weaker (and the life-time is still slightly longer than 1 day). For $\frac{NO}{NO_x}$, the response

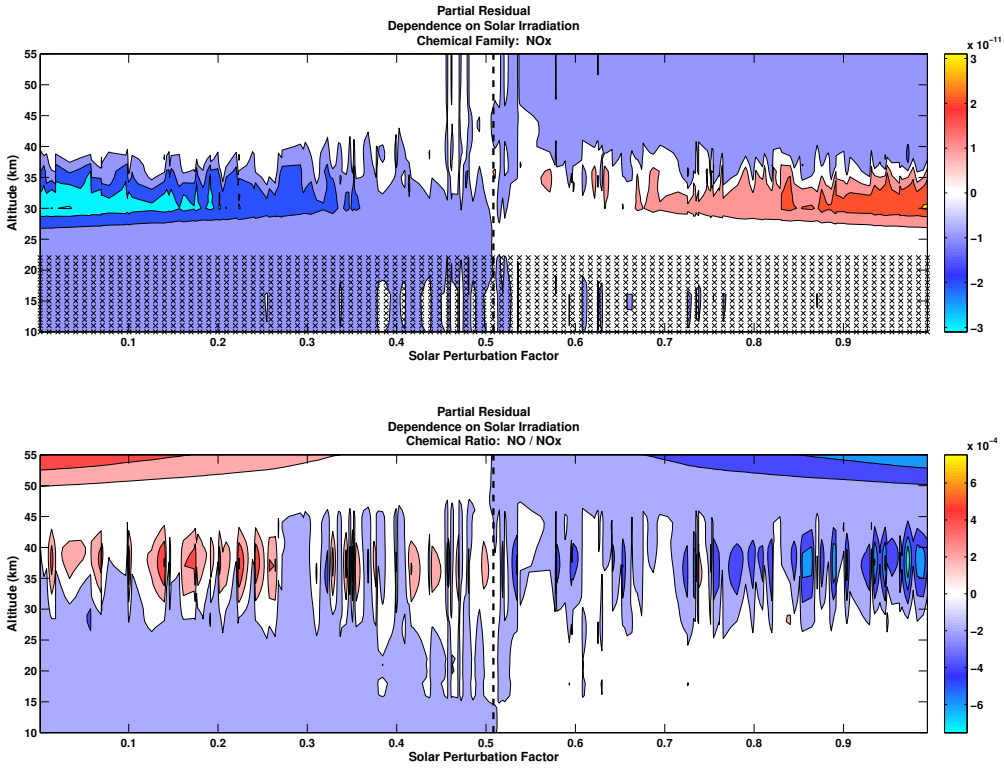

Figure 3.20: Same as Fig. 3.16 but for NO_x (top) and $\frac{NO}{NO_x}$ (bottom).

is anti-correlated and the strongest response is a change in the partitioning ratio of - 6×10^{-4} at the top of the model. The maximum is found at the top of the model as this is where the enhanced conversion from OH to HO_2 occurs during solar maximum (seen in Fig. 3.18), resulting in an increase of Re. 1.14, therefore reducing the partitioning ratio of $\frac{NO}{NO_x}$. A similar peak response occurs between 35 - 45 km. The signal for this response is not quite as clear, but it is due to the increase in Re. 1.13 (described in Sec. 3.1.2).

For the memory, Fig. 3.21 shows that there is both a correlated and anti-correlated response for NO_x. The maximum anti-correlated response is a change of - 0.015 ppbv between 35 - 40 km. Again, this negative response to the memory is due to the positive response of O_x to the memory at the same altitude. The increase in O_x, results in a decrease in NO_x, due to the chemistry described in Sec. 3.1.2. The correlated response is smaller and has a peak change of approximately 0.005 ppbv at 30 km. This peak response is found here due to the location of the peak response to the

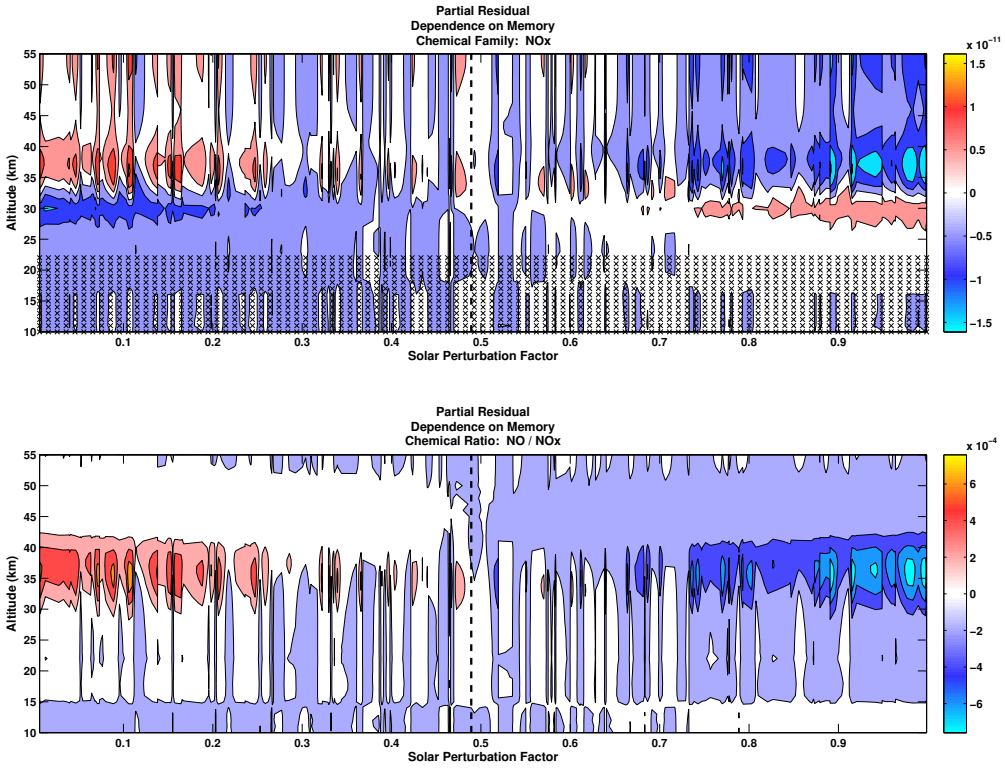

Figure 3.21: Same as Fig. 3.17 but for NO_x (top) and $\frac{NO}{NO_x}$ (bottom).

current day's solar irradiation and is significantly smaller due to the short life-time of NO_x at this altitude. For $\frac{NO}{NO_x}$, the memory response is anti-correlated and the peak change in the partitioning ratio is - 6×10^{-4} between 35 - 40 km, and is due to the same chemistry as the solar irradiation response at this altitude.

3.2.3 Residuals

Correlation coefficients determine how well a linear model fits a data set. Where the correlation coefficient is low, there are residuals caused by non-linearities. For O_x, $\frac{O}{O_x}$, and HO_x, the correlation coefficients are very near 1 and thus the residuals are negligible or non-existent. However, the correlation coefficients are low at certain altitudes for $\frac{OH}{HO_x}$, NO_x, and $\frac{NO}{NO_x}$. Thus there are non-linearities in the chemical response to solar irradiation for these species. These non-linearities are attributed to either the current day's solar perturbation or to the memory. To determine this, the residual is plotted against both the current day's solar perturbation and the

previous day's solar perturbation (memory). If the signal in the plot is clear, rather than appearing like noise, then the residual is attributed to that factor. Figures 3.22 - 3.23 present that the non-linearities (residuals) are attributed to the previous day's solar perturbation (memory). The residuals plotted against the current day's solar perturbation appeared as noise (not shown).

HO_x

As is expected, the residual for HO_x is negligible throughout the vertical column (Fig. 3.22). For $\frac{OH}{HO_x}$, the residual is seen to be anti-correlated and occurs between 30 - 40 km with a peak change in the partitioning ratio of - 4×10^{-4}. The residual is located where the correlation coefficient is near its lowest and also where the response to the memory is found. Thus it is likely attributed to noise as well. Notice that the residual is of the same magnitude as the memory response and therefore the non-linearity is very significant for $\frac{OH}{HO_x}$ if it is in fact not simply noise.

NO_x

Figure 3.23 shows that the residual for NO_x is anti-correlated and is located between 35 - 40 km, with a peak change of approximately - 0.0125 ppbv. This is the same altitude as where the correlation coefficient was lowest, and is also the same altitude as the peak negative response to the memory. Therefore it is likely attributed to the same chemistry that is involved in the response to memory (Sec. 3.2.2). Once again, the residual is of the same magnitude as that of the memory response and therefore the non-linearity is very significant for NO_x as well. The residual for $\frac{NO}{NO_x}$ is similar to that of NO_x. The peak change in the partitioning ratio is - 4×10^{-4} and is found at the same altitude as the response to memory for $\frac{NO}{NO_x}$, and is therefore most likely attributed to the same chemistry as in the memory response (Sec. 3.2.2). At this altitude, the correlation coefficient for $\frac{NO}{NO_x}$ is not at its lowest, but is fairly close. Again, the magnitude of the residual is similar to that of the memory response and therefore the non-linearity for $\frac{NO}{NO_x}$ is also very significant.

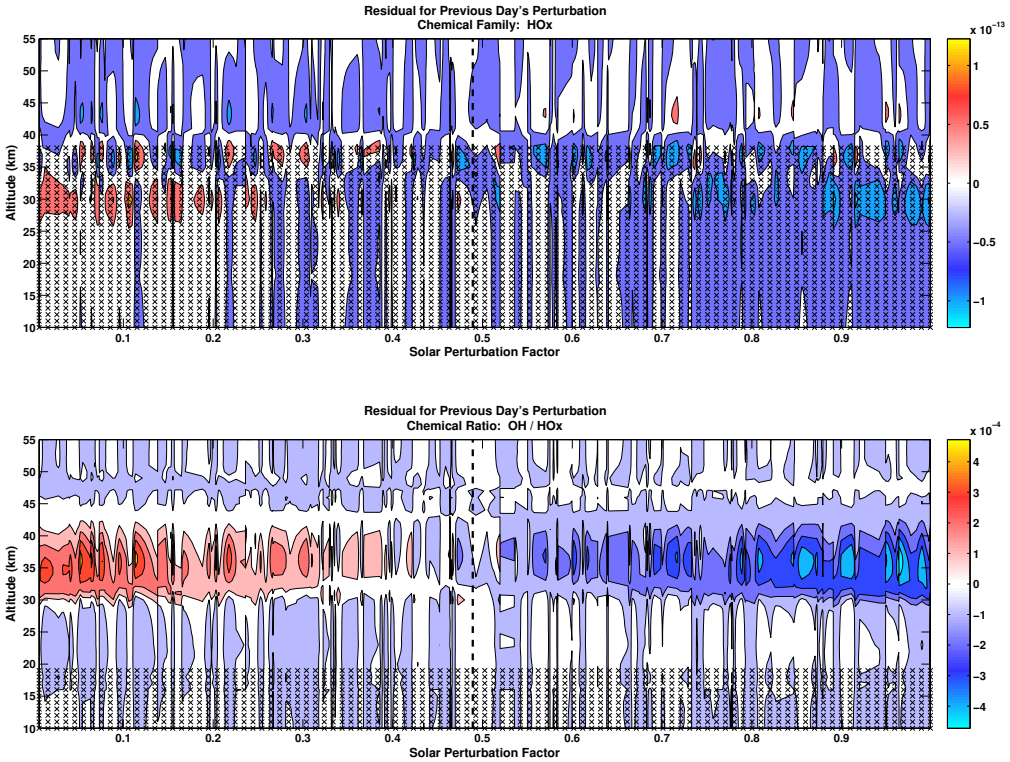

Figure 3.22: Non-linearity (residual) of the response of HO_x (top) and the partitioning ratio of $\frac{OH}{HO_x}$ (bottom) to the previous day's solar perturbation. Residual reflects a change in the mixing ratio (top) or in the partitioning ratio (bottom) and is plotted against the previous day's solar perturbation. Dashed black line represents the average solar perturbation of the 200 ensemble members. Hatched out areas represent altitudes at which the response is negligible (standard deviation of less than 5 % of the maximum).

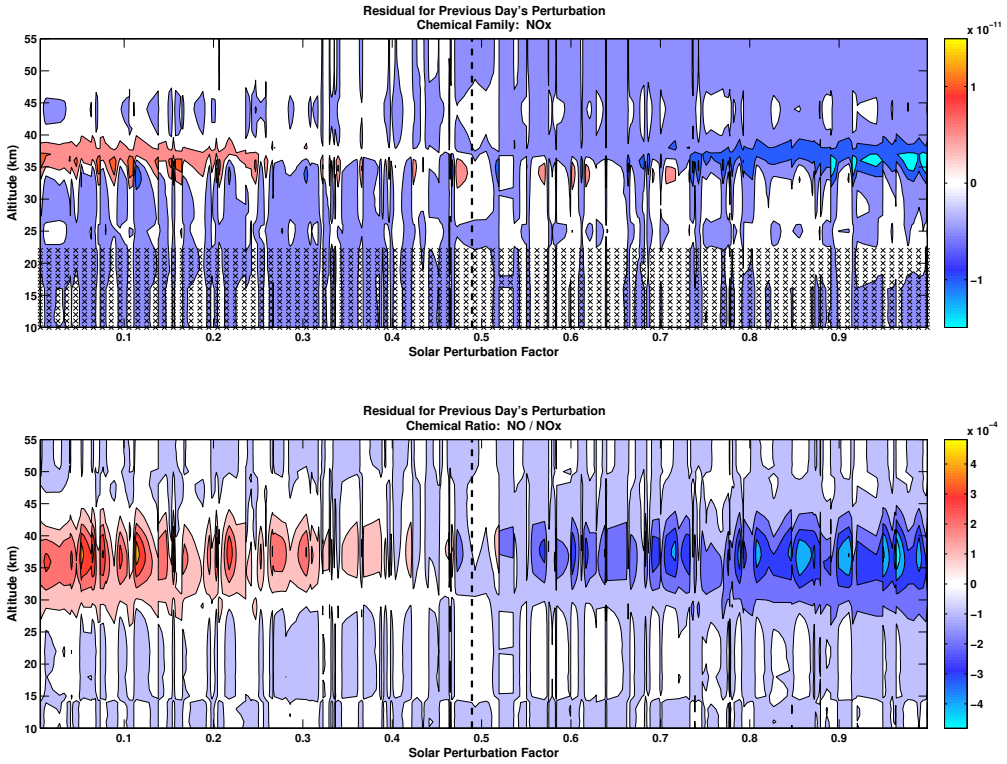

Figure 3.23: Same as Fig. 3.22 but for NO_x (top) and $\frac{NO}{NO_x}$ (bottom).

3.2.4 Linear Model as a Predictive Tool

The linear model is a very good fit for O_x ($R^2 \simeq 1$), and therefore can be used as a predictive tool. Without solving any chemistry, the change in concentration of O_x can be predicted knowing only the current day's solar irradiation and the previous day's concentration. As ozone is the link between chemistry and dynamics (and $[O_x] \simeq [O_3]$ below 42 km), the linear model calculated in Sec. 3.2 can be used to create a predictive model for the ozone perturbation by solar variability. The model can also be used for the other species that have high correlation coefficients, however only the results for ozone are shown here.

It was determined that the residual was negligible, so the linear model becomes:

$$Y(t) \simeq AX_1 + BX_2. \tag{3.7}$$

Recall that $X_2(t) = Y(t-1)$, and thus $Y(t-1)$ can be substituted for $X_2(t)$ iteratively

until the equation becomes:

$$Y(t) = A\sum_{k=1}^{N} B^{k-1}X_1^{N-k+1} + B^N Y(t=0), \tag{3.8}$$

where N is the number of time steps it takes to get to time t. Now $Y(t)$ only depends on the initial conditions and the solar irradiation time sequence. It is important to remember here that the predicted concentrations are the daily averages, and further temporal resolution can not be given from the predictive model.

Equation 3.8 is used to predict the daily average concentrations of ozone for one year using the 27-day solar cycle as the solar forcing. The 27 day solar cycle has an amplitude that is approximately 0.2 % of the TSI (compared to the 11-year cycle which has an amplitude of 0.1 % of the TSI) (*Fröhlich and Lean*, 2004), and thus the solar perturbations go between - 0.5 and 1.5. The 27-day solar forcing is implemented as a sine wave function with the amplitude described above. The sine wave is a similar implementation as in *Williams et al.* (2001). Note that since the linear model is created using a single latitude, longitude and season, the seasonal variation in ozone is not captured. A slightly more complicated predictive tool would be needed to capture the seasonal variation. Also, the linear model was created by analyzing perturbations between 0 and 1, and is now going to be forced with perturbations outside those boundaries (- 0.5 to 1.5). This is not expected to cause any inaccuracies due to the extreme linearity that was found in the ozone response, as well as the fact that the perturbations used will not be far outside of the initial range.

Figure 3.24 presents the sinusoidal evolution of O_x (ozone) with the 27-day solar cycle. In the upper stratosphere, the ozone concentration is maximum when the 27-day solar cycle is at its maximum and is minimum when the 27-day solar cycle is at its minimum. In the middle stratosphere, the response is seen to lag the perturbation because of the longer chemical life-times. Also, as is expected, the maximum percent difference (from the average solar irradiation case) occurs at 40 km and is 3 % when the solar irradiation is largest and - 3 % when the solar irradiation is smallest.

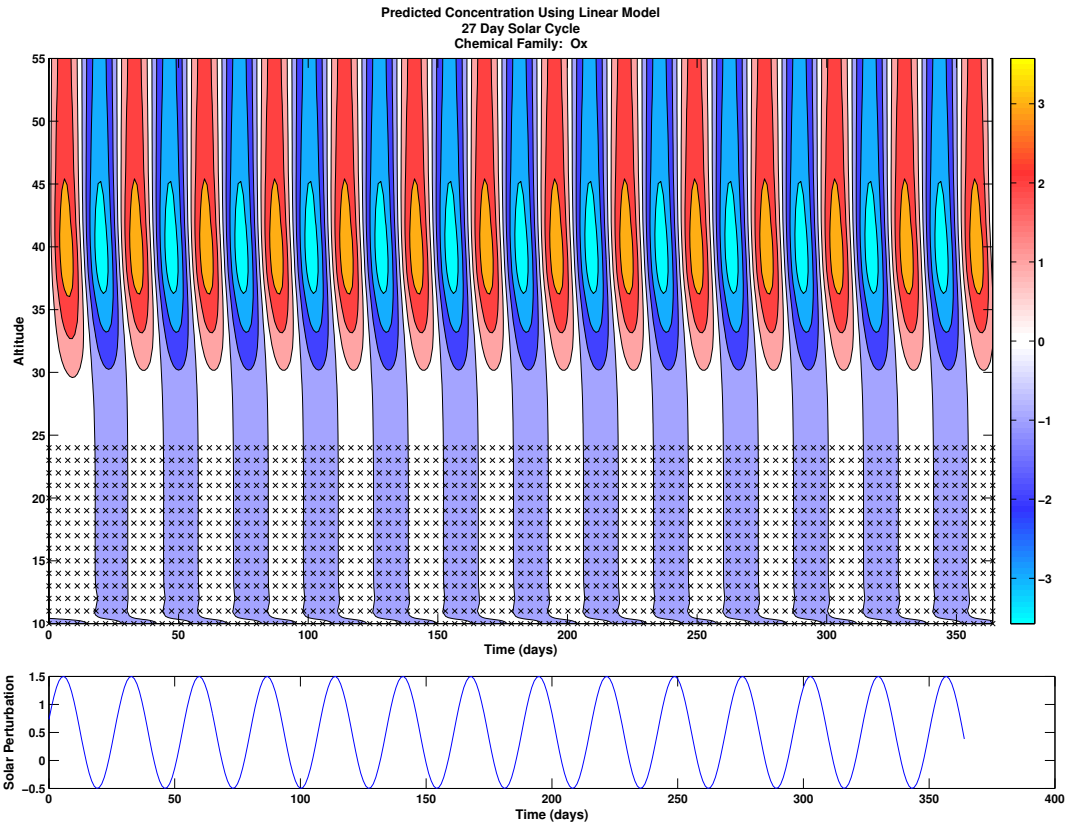

Figure 3.24: 1 year evolution of the predicted change in the mixing ratio of O_x (top), following the 27-day solar cycle perturbations (bottom). Changes are presented as the % change from solar average concentrations. Predicted mixing ratios are calculated using the linear model (Eq. 3.8), and are forced by a sine wave with a period of 27-days. Hatched out areas represent altitudes at which the response is negligible (standard deviation of less than 5 % of the maximum).

3.2.5 Ozone Sensitivity to the 27-day Cycle

Using the predicted concentrations, the ozone sensitivity to the 27-day solar cycle is calculated. In accordance with literature, the sensitivity is defined as the percent change in ozone due to a 1 % change in the 205 nm flux. Figure 3.25 presents the ozone sensitivity as a function of altitude.

In Fig. 3.25, as expected, the sensitivity increases with height until a maximum of a 0.45 % change in ozone per 1 % change in 205 nm flux at 40 km and then slightly decreases above 40 km. These results are within the range of the ozone sensitivities calculated from observations (e.g., *Keating et al.*, 1987) and from CCMs (e.g., *Rozanov et al.*, 2006; *Austin et al.*, 2007), and are slightly higher than the long-time average value of 0.4 % calculated from observational analysis (e.g., *Hood and Zhou*, 1999; *Fioletov*, 2009) and from simulations by 1-D models (e.g., *Brasseur et al.*, 1987), 2-D models (e.g., *Brasseur*, 1993) and CCMs (e.g., *Williams et al.*, 2001). However, the value is also slightly lower than the 0.5 % calculated by *Fleming et al.* (1995) with a 2-D photo-chemical model with pre-specified temperature and transport fields. Therefore, a possible reason for the higher ozone sensitivity is the exclusion of dynamics in the modified BIRA box model, specifically the lack of temperature feedback. Brasseur (1987) calculated the ozone sensitivity both with and without temperature feedback using a 1-D chemical-radiative model, and found that the ozone response to the 205 nm flux decreases when the temperature feedback is included in the calculation. Therefore, not having the temperature feedback in the modified BIRA box model can result in a slightly over-estimated ozone sensitivity. The temperature feedback begins with an increase in ozone (due to enhanced photolysis), resulting in an increase of temperature (due to a larger absorption of solar irradiation), which then results in an increase in the destruction of ozone (reducing the response via negative feedback). The chemistry behind this temperature dependence is explained further in Sec. 3.3.2.

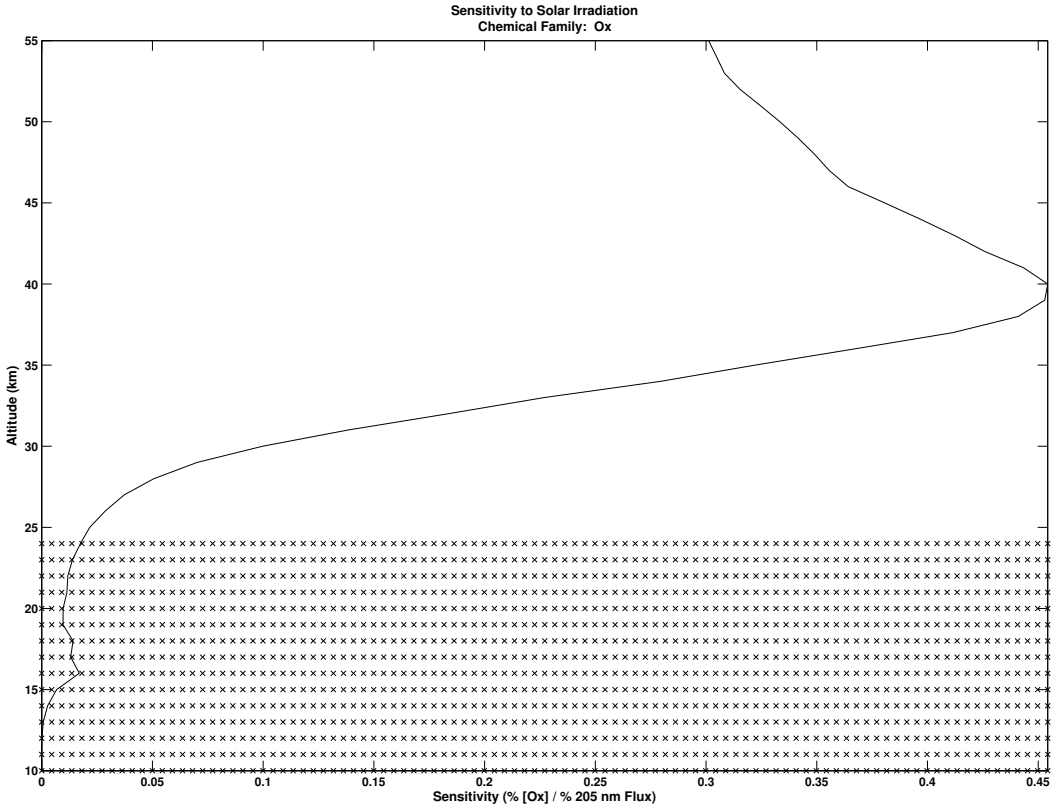

Figure 3.25: Sensitivity of O_x to the 27-day solar cycle. Presented as the % change (from solar average concentrations) in the mixing ratio of O_x for each % change in 205 nm flux. Hatched out areas represent altitudes at which the response is negligible (standard deviation of less than 5 % of the maximum).

3.3 Sensitivity to Initial Conditions

In order understand how the initial conditions affect the chemical response to the solar perturbations, a multiple linear regression is performed on the data from the simulations with perturbed initial conditions. To assess the sensitivity to these initial conditions, the standard deviation and the regression coefficients are compared in Fig. 3.26 - 3.32. Results are only shown for O_x and NO_x. The results are not shown for HO_x since it was found that the response of HO_x to solar variability is not significantly sensitive to the initial conditions.

3.3.1 Standard Deviation

O_x

Figure 3.26 clearly shows that initial condition perturbations of O_x and H_2O do not affect the standard deviation of the O_x members. The NO_x perturbation also has little to no effect on the standard deviation of O_x. It is found that an initial condition perturbation of temperature does indeed affect the standard deviation of O_x amongst the members. Above 35 km, larger standard deviations occur in the initial conditions with the lowest temperatures. The reason for this is explained in Sec. 3.3.2 when describing the effects on the regression coefficients. Note that the difference in the standard deviations among the different days is due to the fact that the average solar irradiation for each day differs slightly.

NO_x

For NO_x, Fig. 3.27 shows similar results for perturbations in O_x and H_2O, however perturbations of NO_x do affect the standard deviation of NO_x. The difference is found throughout most of the vertical column with the largest difference not surprisingly being found at 30 km (where the response to solar irradiation is strongest). Larger standard deviations in NO_x occur with the larger concentrations of NO_x. Similarly to O_x, the perturbation in temperature also has a significant effect on the

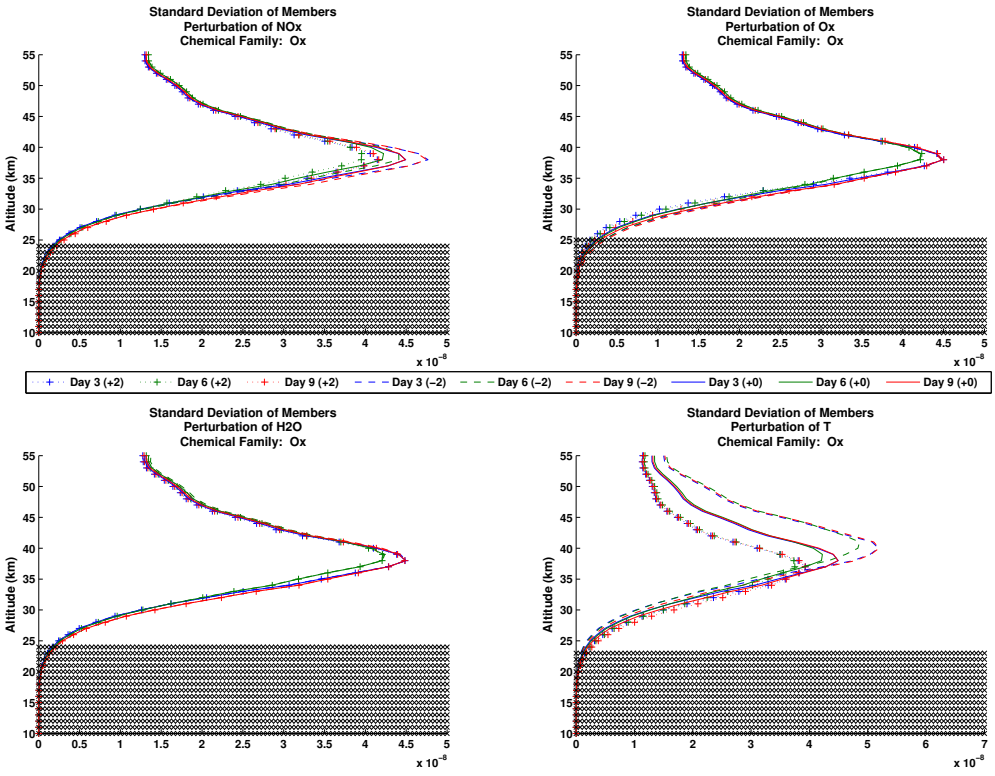

Figure 3.26: Standard deviation in the mixing ratio of the 100 ensemble members for O_x with initial condition perturbations in NO_x (top left), O_x (top right), H_2O (bottom left), and temperature (bottom right). Results are shown for days 3 (blue), 6 (green) and 9 (red). Lines with plus signs represent + 2 standard deviations, dashed lines represent -2 standard deviations, and solid lines represent zero perturbation. Hatched out areas represent altitudes at which the response is negligible (standard deviation of less than 5 % of the maximum).

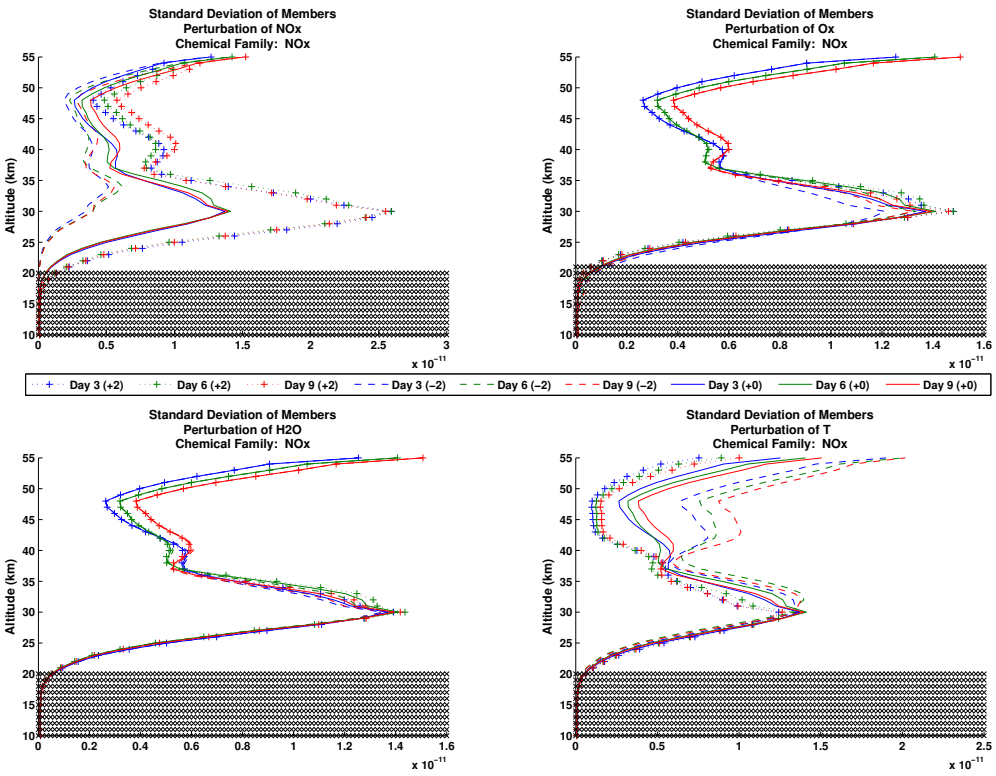

Figure 3.27: Same as Fig. 3.26 but for NO_x.

standard deviation of NO_x above 30 km, with larger standard deviations occurring with lower initial temperatures. The reason for this is explained later in Sec. 3.3.2.

3.3.2 Regression Coefficients

Recall that the regression coefficients presented earlier (Sec. 3.2.1) represented a change in the number of standard deviations of the observed specie. Since the standard deviations are seen to change amongst the different initial conditions, the standardized regression coefficients do not give a clear idea of the sensitivity of the regression coefficients to the perturbations in the initial conditions. To account for this, the standardized coefficients are simply multiplied by the standard deviation of the observed species (O_x or NO_x).

O_x

Figure 3.28 presents the initial condition sensitivity of the response to the current day's solar irradiation for O_x. As expected from the standard deviations, the only significant sensitivity occurs for the perturbation in temperature. Above 40 km, higher initial temperatures coincide with a weaker response to solar irradiation. Using observations, Fioletov (2009) also discovered that the ozone response tends to be reduced when a temperature disturbance is in phase with the solar variation. A similar feedback was found by *Brasseur et al.* (1987) and *Keating et al.* (1987), where increases in upper stratospheric temperatures resulted in increased rates of ozone destruction. The reduced response is due to a speed up of the O_x destroying chemical reactions due to the higher temperatures. In a separate experiment, *Brasseur et al.* (1990) found that a stratospheric cooling caused by a doubling of CO_2 resulted in an increase of net ozone production. Most chemical reactions that destroy O_X are bimolecular reactions whose rates typically increase with temperature. As temperatures increase the molecules have more energy and thus have a greater probability of meeting and reacting with each other (*NASA*, 2000). Specifically, Re. 1.13 has a large temperature dependence (seen in Fig. 3.29), resulting in an increased destruction of O_x with increased temperatures. Furthermore, the production of O_3 (Re. 1.2) is also temperature dependent (Fig. 3.29). Reaction 1.2 is a termolecular reaction, whose rates typically decrease with temperature (*NASA*, 2000). Thus, as the O_x production rates decrease and the destruction rates increase, the O_x concentrations become less photolysis driven and the solar irradiation response becomes weaker.

A similar situation is seen in Fig. 3.30 for the memory regression coefficient for O_x. Above 30 km, the memory coefficient is weaker for higher initial temperatures. The chemistry behind this is the same as for the solar irradiation response. As the O_x concentration becomes less photolysis driven, less of the response to the current day's solar irradiation is held through the night, and therefore the memory response is weaker.

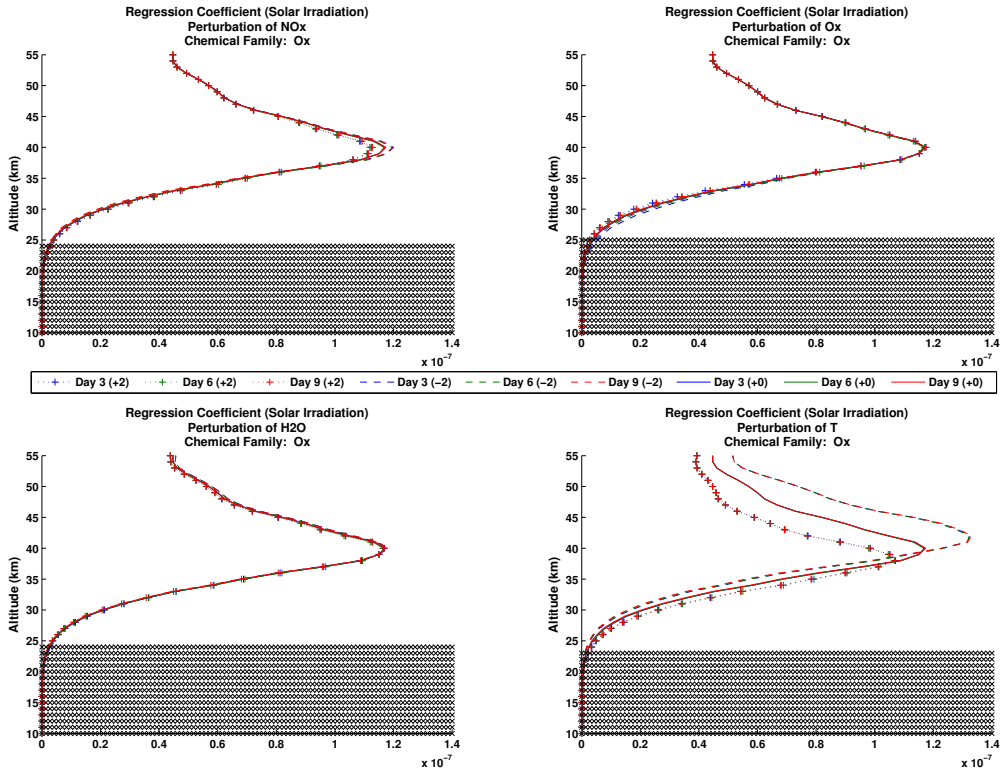

Figure 3.28: Unstandardized solar irradiation regression coefficient for O_x with initial condition perturbations in NO_x (top left), O_x (top right), H_2O (bottom left), and temperature (bottom right). Results are shown for days 3 (blue), 6 (green) and 9 (red). Lines with plus signs represent + 2 standard deviations, dashed lines represent -2 standard deviations, and solid lines represent zero perturbation. Hatched out areas represent altitudes at which the response is negligible (standard deviation of less than 5 % of the maximum).

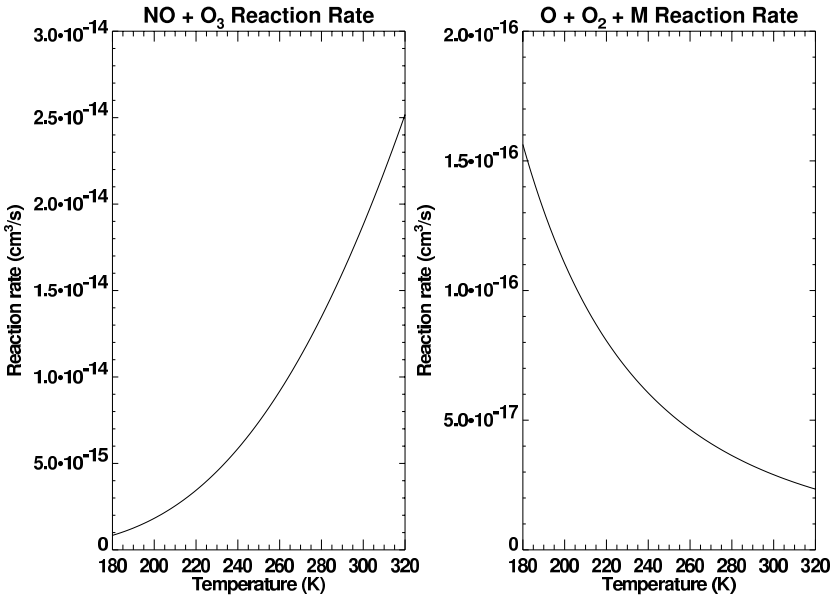

Figure 3.29: Temperature dependence of reactions between chemical species. Source: *NASA* (2000).

NO_x

Figure 3.31 shows sensitivities to initial conditions for the solar irradiation coefficient to both NO_x and temperature perturbations. The perturbation in NO_x has two separate effects. The larger effect is found below 35 km, where larger initial concentrations in NO_x result in a stronger response to solar irradiation. Note that when the initial NO_x conditions are perturbed, N_2O_5 and HNO_3 are perturbed as well. The increase in HNO_3 results in an increase of Re. 1.22, producing more NO_x during photolysis, therefore increasing the response to solar irradiation. The smaller effect is found above 35 km, where larger initial concentrations in NO_x result in a slightly larger negative response to solar irradiation. Recall that the negative response to solar irradiation (Sec. 3.1.2) is due to the enhancement of Re. 1.20. An increase in the initial concentrations of NO_2 (NO_x) results in a further increase in the rate of Re. 1.20, as well as Re. 1.19, resulting in a stronger negative response. The sensitivity to temperature also has two separate effects. Below 40 km, higher initial temperatures result in a weaker response to solar irradiation. The change is small

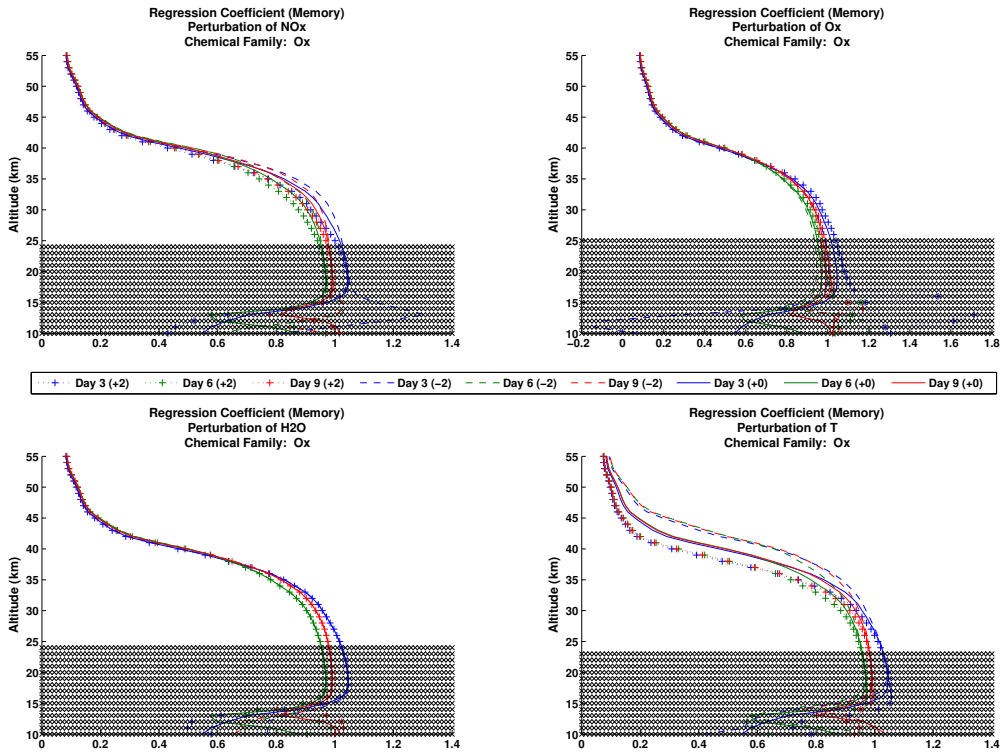

Figure 3.30: Unstandardized memory regression coefficient for O_x with initial condition perturbations in NO_x (top left), O_x (top right), H_2O (bottom left), and temperature (bottom right). Results are shown for days 3 (blue), 6 (green) and 9 (red). Lines with plus signs represent + 2 standard deviations, dashed lines represent -2 standard deviations, and solid lines represent zero perturbation. Hatched out areas represent altitudes at which the response is negligible (standard deviation of less than 5 % of the maximum).

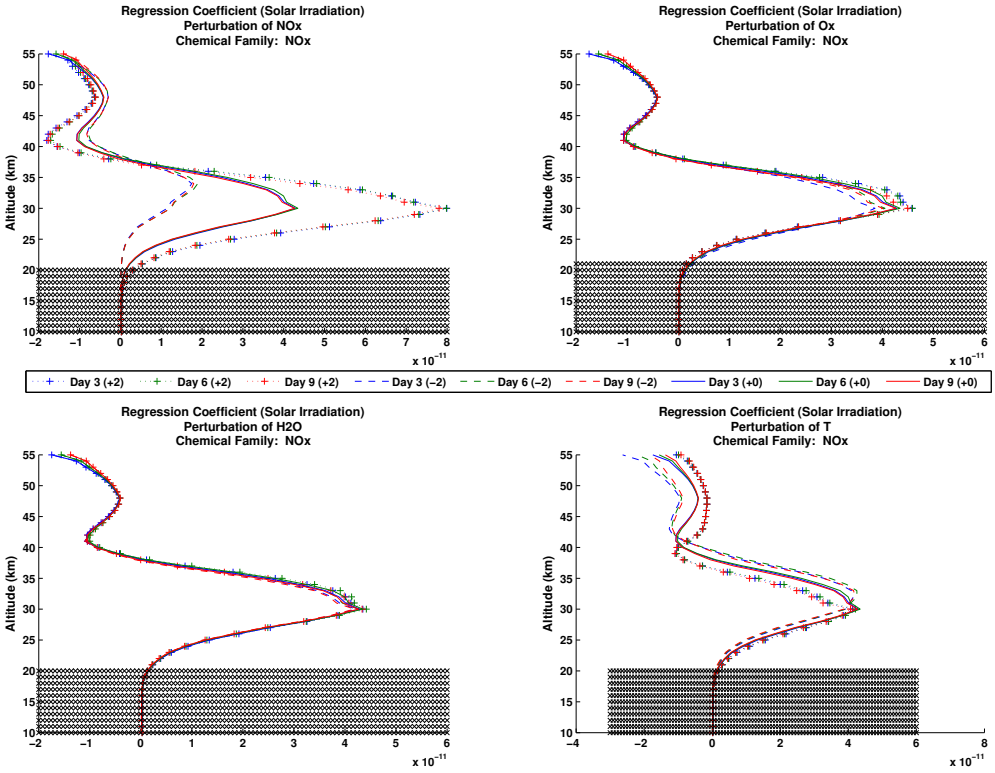

Figure 3.31: Same as Fig. 3.28 but for NO_x.

and is likely due to the decreased production of HNO_3 and N_2O_5 through termolecular Re. 1.19 and 1.20 due to the temperature dependence. This would result in a decrease in the photolysis back to NO_x through Re. 1.21 and 1.22, causing a weaker response to solar irradiation. Above 40 km, higher initial temperatures result in a weaker negative response to solar irradiation. The weaker negative response is due to the temperature dependence of Re. 1.19 and 1.20. Both reactions are termolecular and their rates decrease with temperature, resulting in a weaker negative response. Overall, larger initial concentrations of NO_x result in an increased response to solar irradiation, while higher initial temperatures result in a decreased response to solar irradiation.

Again, sensitivities of the memory coefficient to both NO_x and temperature perturbations are seen in Fig. 3.32. For the NO_x perturbation, the effect is only found below 30 km. This time the sensitivity only seems to occur for lower initial concentrations of NO_x, which correspond to a weaker memory response. The reasoning

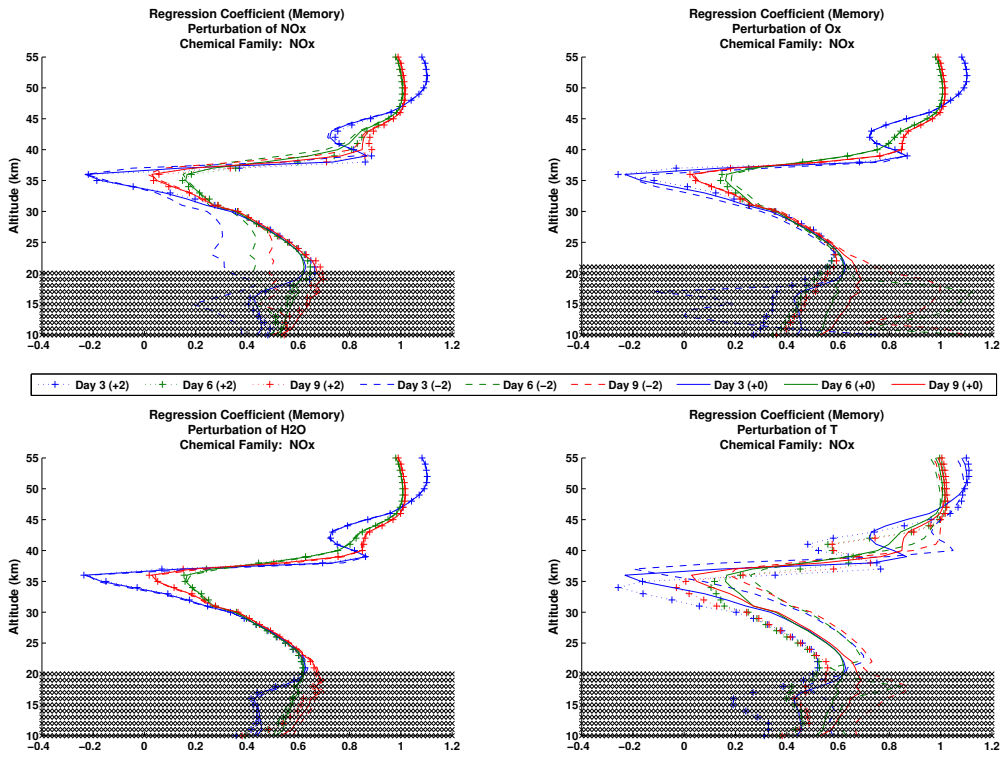

Figure 3.32: Same as Fig. 3.30 but for NO_x.

is the same as for the solar irradiation coefficient at these altitudes. The lack of sensitivity in the memory response to an increase in the initial NO_x concentrations can be thought of as a saturation of the memory. For the temperature perturbation, the sensitivity is mainly seen below 35 km, where lower initial temperatures result in a stronger memory response. Again, the reasoning is the same as for the solar irradiation coefficient at these altitudes.

3.4 IGCM-BIRA

3.4.1 Constant Solar Irradiation

Similarly to Sec. 3.1.2, the difference between solar minimum and solar maximum conditions is identified. Results are only shown for O_x as none of the other species showed any statistically significant differences due to the short length of the simulations. Figure 3.33 presents the seasonal difference between the zonal mean solar

minimum and solar maximum concentrations as a function of latitude and height.

O_x

From Fig. 3.33, it can be seen that the only statistically significant difference for O_x is the peak minimum-to-maximum difference, which for all seasons is 1×10^{-7} (~ 2 %) and is centered around the equator at an altitude of 40 km. The altitude of the peak difference is expected and is due to the same chemistry as previously discussed in Sec. 3.1.2. The value is less than the 3 % that was estimated in Sec.3.1.2, but is still within the low-end of the range determined in the observations by *Soukharev and Hood* (2006) and *Fioletov* (2009), and in the CCM simulations by *Tourpali et al.* (2003). The value is also in very good agreement with the minimum-to-maximum differences determined from simulations by 2-D models *Brasseur* (e.g., 1993) and CCMs *Egorova et al.* (e.g., 2005). Although the signal is weakly significant, a latitudinal and seasonal dependence can still be extracted qualitatively. The latitudinal dependence is seen in how the difference between solar maximum and solar minimum conditions weakens away from the equator, which is expected since the solar irradiation is strongest at the equator. The seasonal dependence is seen in the fact that away from the equator, the minimum-to-maximum difference appears to be stronger in the hemisphere in which it is summer or spring. However, these differences are not statistically significant, and thus the seasonal dependence is not certain.

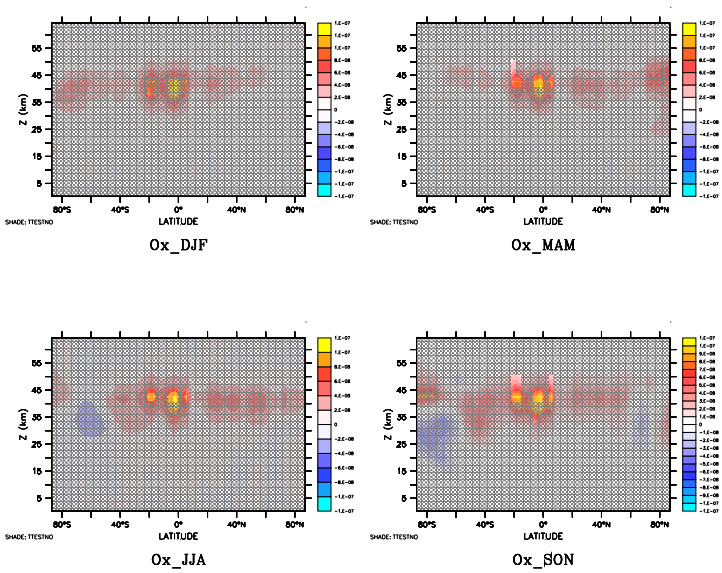

Figure 3.33: Latitudinal dependence of the difference in the zonal mean volume mixing ratio of O_x between solar minimum and solar maximum simulations for DJF (upper left), MAM (upper right), JJA (lower left), and SON (lower right). Shading marks regions where the difference is not statistically significant at the 95 % confidence level.

Chapter 4

Summary and Discussion

Modified BIRA Box Model

A new stratospheric chemistry box model that includes a more accurate photolysis calculation has been developed. The photolysis rates are no longer interpolated from a look-up table and are no longer calculated using standard atmospheric temperatures and absorbing gas concentrations. The photolysis rates are calculated on-line and are fully-interactive with pressure, temperature, and all of the absorbing gases (O_3, O_2, NO, NO_2, CO_2, and air).

Constant Solar Irradiation

Using the modified BIRA box model, three short 10-day simulations were run using solar minimum irradiation, solar maximum irradiation, and average solar irradiation. These simulations highlight the difference between solar minimum and solar maximum conditions through changes in the photo-chemistry. The largest minimum-to-maximum difference for O_x was determined to be approximately 3 % at around 40 km, and is due to the increase of O atoms (increased photolysis of O_2). This result is in close agreement with both the observational analysis and the other simulations in the literature. Therefore the pure photo-chemical effect is extremely important in the response of ozone to solar variability. The difference between solar minimum

and solar maximum conditions was also determined for HO_x (3 % at 50 - 55 km) and NO_x (1 % at 25 - 30 km, and - 1.5 % at 35 - 40 km), and for the partitioning ratios of $\frac{O}{O_x}$ (1 % at 55 km), $\frac{OH}{HO_x}$ (- 2 % at 30 - 45 km), and $\frac{NO}{NO_x}$ ($<$ 1 % at 25 - 45 km). Detailed response mechanisms are identified. Note that this analysis fills a gap as most studies on solar variability focus on the response of ozone only.

Solar Variability

The important part of the paper is the investigation of the effect of daily solar variability on the chemical response. This was done by using random solar perturbations as the solar forcing, and performing a multiple regression analysis on the ensemble members. The use of a random solar perturbations provided the opportunity to analyze the fundamentals of the chemical response. Also, by using a large ensemble of random solar forcing it was possible to cover a wide range of solar activity conditions, which is necessary to assess the relationship to solar variability (*Haigh*, 1994, 1996; *Rind and Balachandran*, 1995).

Regression Coefficients, Partial Residuals, and Residuals

From the regression analysis, it was seen that for most chemical species the solar irradiation coefficient was dominant in the upper stratosphere while the memory coefficient was dominant in the lower stratosphere. This is due to both the abundance of sunlight at the top of the model and the decrease in chemical life-time with increasing altitude. A look at the partial residuals separated the effect of the current day's solar irradiation from the previous day's solar irradiation (memory). An increase in the current day's solar irradiation was found to lead to an increase in O_x (40 km), HO_x (55 km) and NO_x (30 - 35 km), and an increase in the partitioning ratio of $\frac{O}{O_x}$ (55 km). On the other hand, it led to a decrease in the partitioning ratios of $\frac{OH}{HO_x}$ (35 km and 55 km) and $\frac{NO}{NO_x}$ (35 - 40 km, and 55 km). For the memory, an increase in the previous day's solar irradiation led to an increase in O_x (35 - 40 km) and HO_x (45 - 55 km). On the other hand, it led to a decrease in NO_x (35 - 40 km) and a

decrease in the partitioning ratios of $\frac{O}{O_x}$ (55 km), $\frac{OH}{HO_x}$ (35 km) and $\frac{NO}{NO_x}$ (35 - 40 km). It is also worth noting that the regression coefficients did not differ significantly from day to day. Therefore the chemical response is constant throughout the simulation.

A look at the correlation coefficients from the regression analysis showed that the chemical response for O_x, HO_x, and $\frac{O}{O_x}$ is linear, whereas the chemical response was determined to be non-linear for NO_x, $\frac{OH}{HO_x}$, and $\frac{NO}{NO_x}$. The non-linearity in $\frac{OH}{HO_x}$ was a negative response and was possibly caused by noise. The non-linearity in NO_x was a negative response and was caused by the positive response of O_x, resulting in an increase of Re. 1.18 and 1.19. The non-linearity in $\frac{NO}{NO_x}$ was also a negative response and was caused by the positive response of $\frac{OH}{HO_x}$, resulting in an increase of Re. 1.14. The residual for each of these species was found to be quite significant and was determined to be associated with the previous day's solar perturbation. Therefore, the non-linear response acts through the memory of the species.

Upon suggestion of one of the reviewers, additional terms of $x_3(t) = y(t-2)$ and $x_4(t) = y(t-3)$ were included in the regression analysis to ensure that the non-linearities were in fact associated with the previous day's memory and not associated with a two-day or three-day lagged memory. These additional terms were found to be negligible and did not influence the correlation coefficients or the residuals in any way. Thus a one-day lagged memory is sufficient and the non-linearities are in fact associated with the memory of the species. This is expected as the problem at hand is simply an initial condition problem.

Predictive Model and Ozone Sensitivity

Since the response of O_x was found to be linear, it was possible to create a linear model to predict the change in concentration of O_x due to a solar perturbation. A predictive model of this kind would be very helpful as it could be used to completely replace a computationally expensive chemistry scheme in a global circulation model (GCM) as far as the response of O_3 to solar variability is concerned. However, the linear model would first need to include a dependence on latitude and initial conditions. The model was used to assess the ozone response to the 27-day solar

cycle by calculating the ozone sensitivity. The maximum ozone sensitivity was found to be a 0.45 % change in ozone per 1 % change in 205 nm flux, around 40 km. This value is slightly larger, but in close agreement with the values found in literature. The higher sensitivity can be due to the lack of dynamics or to an ozone-temperature feedback (seen in the initial condition sensitivity simulations).

Although the linear model for ozone can not quite be used as a replacement for a chemistry scheme, it is interesting that the predictions (at the equator) match so well with observations and other simulations. The linear model was created from the regression analysis of daily responses to random solar perturbations, and yet was able to reproduce the response on a longer time-scale (27-day solar cycle). The daily response was also extrapolated well to the 11-year solar cycle in the constant solar irradiation simulations. *Brasseur et al.* (1987) found that the mechanisms responsible for the response of ozone to the 27-day and 11-year solar cycles are similar, which suggests that the amplitude of the 11-year cycle in ozone may be calculated from the regression analysis of the 27-day cycle in ozone (*Keating et al.*, 1994; *Chandra and McPeters*, 1994). The research in this paper confirms this, and shows that the daily response of ozone can be extrapolated to the 27-day ozone cycle. Therefore, the short-term response of ozone can be extrapolated to longer time-scale responses. This ability to extrapolate to longer time-scales may help with the issue of extracting the response of ozone to the 11-year cycle from such short records of observations. It is expected that this would also be possible for the other chemical species that showed a linear response (HO_x and $\frac{O}{O_x}$).

Sensitivity to Initial Conditions

In order to determine if the initial conditions used have an effect on the chemical response to solar variability, an ensemble of simulations were run with perturbed initial conditions. The perturbations were in NO_x, O_x, H_2O and temperature. It was determined that the response of HO_x was not significantly sensitive to the initial conditions, and that the response of both O_x and NO_x were not sensitive to perturbations of O_x or H_2O. As was expected, O_x was found to be sensitive to tem-

perature perturbations due to the temperature dependence of O_x destroying chemical reactions (such as Re. 1.13) and the production of ozone (Re. 1.2). An increase in temperature resulted in a decrease in the response of O_x. NO_x was found to be sensitive to both perturbations in NO_x and temperature. Larger concentrations in NO_x meant larger concentrations of HNO_3 and N_2O_5. This increased the response of NO_x to solar variability because it led to an increase in Re. 1.22. Higher temperatures result in a decrease in the response of NO_x, which is due to Re. 1.19 - 1.20 being weaker due to their temperature dependence.

IGCM-BIRA

Once the pure chemical response was investigated, the modified BIRA box model was coupled to the IGCM to include atmospheric dynamics. The modified IGCM-BIRA is the first climate-chemistry model to include an on-line photolysis calculation. Although it is computationally expensive, it allows for an extremely accurate representation of the photo-chemistry in the stratosphere. The model allows for the effect of including dynamics to be looked at. Also, since the simulations were run globally and over several years, the latitudinal and seasonal dependence could be assessed.

Constant Solar Irradiation

Using the IGCM-BIRA, two 5-year long simulations were run using either solar minimum or solar maximum irradiation. It was found that the simulations were not long enough to determine a statistically significant minimum-to-maximum difference, especially in the higher latitudes which are influenced more by the dynamics. Only the peak difference in O_x was determined to be statistically significant. The peak difference was found near the equator to be ~ 2 % at an altitude of approximately 40 km. As expected, this value is less than that calculated in the pure chemistry simulations. The latitudinal dependence was seen in how the minimum-to-maximum difference was strongest near the equator and no clear seasonal dependence was

seen. Recall that the chemical responses were not extremely sensitive to the initial conditions, and thus it appears that the strength of the solar irradiation and the length of the day are the dominant factors in the latitudinal and seasonal dependence.

Future Work

Although the simulations included an accurate calculation of photolysis rates, there are still some limitations that need to be addressed in future work. It was seen that the chemical response of the species (specifically ozone) had a temperature dependence. As mentioned, this temperature feedback was not accounted for in the simulations since the ozone was not coupled to the radiation scheme. Additionally, in order to get an accurate simulation of the solar signal in the stratosphere it is necessary to have a correct representation of the heating rates due to oxygen and ozone (*Egorova et al.*, 2004). Thus, for future simulations it would be necessary to couple the ozone to the radiation scheme and to include solar variability in the UV radiation as well. Running simulations both with and without the temperature feedback mechanism allows for the separation of the response due to the dynamics and the response due to the radiation feedback. Also, the analysis involving the BIRA-IGCM results is only a first step in analyzing the chemistry-dynamics response. Further simulations with the BIRA-IGCM will allow for the separation of the dynamical effect from the chemical effect. Simulations investigating the effect of including dynamics on the ozone sensitivity to the 27-day solar cycle are currently under way. Longer simulations can be run to produce more statistically significant results. Also, the height up to which the chemistry is solved could be raised from 1 hPa to 0.1 hPa to better represent the photo-chemistry that occurs in the upper stratosphere.

It is not only the representation of the atmospheric processes in the model that can be better represented, the solar variability forcing could also be represented more accurately. Solar variability through random solar perturbations was successful in covering a wide range of solar activity and in investigating the basic chemical re-

sponse, however the next step is to include more realistic solar variations. Since absorption is strongly wavelength dependent, there is the need for simulations with spectrally resolved solar variability (*Fröhlich and Lean*, 2002). Another reason to include more realistic solar forcing in climate simulations is that the solar cycles contain more frequencies than just the 27-day or 11-year (*Austin et al.*, 2007). Spectrally resolved irradiance can be obtained from either satellite observations (*Thuillier et al.*, 2003; *Harder et al.*, 2005) or from solar models. Solar models can be used to either create solar reconstructions or to predict solar output. Examples of such models can be found in *Charbonneau et al.* (2008), *Crouch et al.* (2008) and *Fröhlich and Lean* (2004). Along with spectrally resolved solar variability, inter-daily solar variability could also be implemented. This could be incorporated using satellite observations or solar models, and would include sudden changes in the TSI, such as during the famous solar storm in October of 2003. There are future plans to collaborate with Paul Charbonneau (Université de Montréal) to couple a solar model to the IGCM-BIRA with on-line photolysis calculation.

Chapter 5

Conclusion

In this study, a new stratospheric chemistry box model with an accurate on-line photolysis calculation has been successfully developed. The model was used to simulate the effect of daily solar variability on stratospheric chemistry. A step-by-step approach was taken, allowing for the isolation of the effects of various mechanisms. The first step was to thoroughly investigate the chemistry-only response to solar variability. Short simulations forced by solar minimum and solar maximum irradiation showed that the strongest response for ozone occurs at 40 km. Here there is 3 % more ozone during solar maximum irradiation, a value that is in agreement with the literature. By including a daily random solar perturbation, the fundamental mechanisms behind the chemical response were assessed thoroughly. The effect of the current day's solar perturbation was separated from the memory effect of the previous day's solar perturbation, and both were studied in detail. In general, it was found that the effect of the current day's solar irradiation was more prominent in the upper stratosphere, whereas the memory effect of the previous day's solar perturbation was more prominent in the lower stratosphere where chemical life-times are longer. The chemical response of O_x to solar variability was found to be extremely linear in nature, along with the response of HO_x and $\frac{O}{O_x}$, whereas non-linearities of significant magnitude were found in the response of NO_x, $\frac{OH}{HO_x}$ and $\frac{NO}{NO_x}$. The non-linearity was determined to act through the memory of the response. The detailed analysis of O_x and the other chemical species fills a gap in current research.

The linear nature of O_x allowed for the development of a predictive model, which was used to test the response of O_x to the 27-day solar cycle. The ozone sensitivity was calculated to be a 0.45 % change in ozone per 1 % change in the 205 nm flux, which is in close agreement with literature. This means that the daily response of ozone can be extrapolated to capture the response to the 27-day cycle. The ability of extrapolating the daily response to longer time-scales suggests that the daily response can be extrapolated to determine the effect of a solar forcing that consists of a superposition of sine waves, and therefore of a realistic solar variability.

The next step was the inclusion of dynamics by coupling the chemistry model with on-line photolysis calculation to a general circulation model. The addition of dynamics led to a decrease in the minimum-to-maximum difference in O_x. The calculated difference of 2 % is still in agreement with literature, as there is a wide range of results. The decrease in the response of O_x was determined to be due solely to the inclusion of dynamics and not due to the ozone-temperature feedback as the ozone was un-coupled from the radiation scheme.

Next steps would involve coupling the ozone to the radiation code in order to isolate the radiation effect, but first longer simulations need to be run in order to extract a clearer response from ozone and the other species. Also, simulations forced by more realistic, spectrally resolved solar variability from either observations or from a solar model should be performed. There are still discrepancies between models and observations, and the mechanisms behind the response of ozone and other chemical species to solar variability is still unclear, and thus more work needs to be done. However, the step-by-step approach undertaken in this study is a good start.

Appendix A

Appendix

A.1 Photolysis Reactions

Rate	Reaction
$J(O_2)$	$O_2 + h\nu \longrightarrow 2O$
$J(O_3)$	$O_3 + h\nu \longrightarrow O + O_2$
$J(H_2O)$	$H_2O + h\nu \longrightarrow H + OH$
$J(N_2O)$	$N_2O + h\nu \longrightarrow N_2 + O(^1D)$
$J(CO_2)$	$CO_2 + h\nu \longrightarrow CO + O$
$J(CH_4)$	$CH_4 + h\nu \longrightarrow CH_3 + H$
$J(NO_2)$	$NO_2 + h\nu \longrightarrow NO + O$
$J(HNO_3)$	$HNO_3 + h\nu \longrightarrow OH + NO_2$
$J(CFC12)$	$CFC12 + h\nu \longrightarrow Cl + CF_2O + products$
$J(CFC11)$	$CFC11 + h\nu \longrightarrow Cl + CClFO + products$
$J(CFC10)$	$CFC10 + h\nu \longrightarrow Cl + products$
$J(HOCl)$	$HOCl + h\nu \longrightarrow OH + Cl$
$J(CH_3CCl_3)$	$CH_3CCl_3 + h\nu \longrightarrow 3Cl$
$J(HO_2NO_2)_{HO_2}$	$HO_2NO_2 + h\nu \longrightarrow HO_2 + NO_2$
$J(CH_3Cl)$	$CH_3Cl + h\nu \longrightarrow Cl + CH_3$

Continued on next page

Table A.1 – continued from previous page

Rate	Reaction
$J(ClONO_2)_{ClO}$	$ClONO_2 + h\nu \longrightarrow ClO + NO_2$
$J(N_2O_5)$	$N_2O_5 + h\nu \longrightarrow NO_2 + NO_3$
$J(O_3)_{O(^1D)}$	$O_3 + h\nu \longrightarrow O(^1D) + O_2$
$J(CFC113)$	$CFC113 + h\nu \longrightarrow CF_2O + products$
$J(CFC_22)$	$HCFC22 + h\nu \longrightarrow CF_2O + products$
$J(Ha1211)$	$Ha1211 + h\nu \longrightarrow 2HF$
$J(Ha1301)$	$Ha1301 + h\nu \longrightarrow 3HF$
$J(H_2O_2)$	$H_2O_2 + h\nu \longrightarrow 2OH$
$J(CH_2O)_{HCO}$	$CH_2O + h\nu \longrightarrow CHO + H$
$J(BrONO_2)_{Br}$	$BrONO_2 + h\nu \longrightarrow Br + NO_3$
$J(HOBr)$	$HOBr + h\nu \longrightarrow Br + OH$
$J(CH_3Br)$	$CH_3Br + h\nu \longrightarrow CH_3 + Br$
$J(OClO)$	$OClO + h\nu \longrightarrow O + ClO$
$J(Cl_2O_2)$	$Cl_2O_2 + h\nu \longrightarrow Cl + ClOO$
$J(Cl_2)$	$Cl_2 + h\nu \longrightarrow 2Cl$
$J(CCl_2O)$	$CCl_2O + h\nu \longrightarrow products$
$J(CClFO)$	$CClFO + h\nu \longrightarrow HF + products$
$J(CF_2O)$	$CF_2O + h\nu \longrightarrow 2HF + products$
$J(CFC114)$	$CFC114 + h\nu \longrightarrow 2CF_2O + products$
$J(CFC115)$	$CFC115 + h\nu \longrightarrow CF_2O + HF$
$J(HCl)$	$HCl + h\nu \longrightarrow H + Cl$
$J(CH_2O)_{CO}$	$CH_2O + h\nu \longrightarrow CO + H_2$
$J(CH_3OOH)$	$CH_3OOH + h\nu \longrightarrow CH_3O + OH$
$J(CH_3CO_3)$	$CH_3CO_3 + h\nu \longrightarrow products$
$J(PAN)$	$PAN + h\nu \longrightarrow products$
$J(ClNO_2)$	$ClNO_2 + h\nu \longrightarrow Cl + NO_2$
$J(NO_3)$	$NO_3 + h\nu \longrightarrow NO_2 + O$

Continued on next page

Table A.1 – continued from previous page

Rate	Reaction
$J(NO)$	$NO + h\nu \longrightarrow N + O$
$J(BrCl)$	$BrCl + h\nu \longrightarrow Br + Cl$
$J(BrO)$	$BrO + h\nu \longrightarrow Br + O$
$J(HO_2NO_2)_{OH}$	$HO_2NO_2 + h\nu \longrightarrow OH + NO_3$
$J(ClONO_2)_{Cl}$	$ClONO_2 + h\nu \longrightarrow Cl + NO_3$
$J(NO_3)_{O_2}$	$NO_3 + h\nu \longrightarrow NO + O_2$
$J(ClOO)$	$ClOO + h\nu \longrightarrow ClO + O$
$J(O_2)_{O(^1D)}$	$O_2 + h\nu \longrightarrow O(^1D) + O$
$J(CHBr_3)$	$CHBr_3 + h\nu \longrightarrow 3Br$
$J(HO_2)$	$HO_2 + h\nu \longrightarrow OH + O$
$J(BrONO_2)_{BrO}$	$BrONO_2 + h\nu \longrightarrow BrO + NO_2$

Table A.1: Photo-chemical reactions that are included in the BIRA box model.

A.2 Chemical Reactions

#	Reaction
1	$O(^3P) + O_2 \longrightarrow O_3$
2	$O_3 + O(^3P) \longrightarrow 2O_2$
3	$O(^1D) + N_2 \longrightarrow O(^3P)$
4	$O(^1D) + N_2 \longrightarrow N_2O$
5	$O(^1D) + O_2 \longrightarrow O(^3P)$
6	$O_3 + O(^1D) \longrightarrow 2O_2$
7	$O_3 + O(^1D) \longrightarrow 2O(^3P)$
8	$H_2O + O(^1D) \longrightarrow 2OH$
9	$H_2 + O(^1D) \longrightarrow OH + H$
10	$CH_4 + O(^1D) \longrightarrow H_2 + CH_2O$
11	$CH_4 + O(^1D) \longrightarrow CH_3 + OH$
12	$N_2O + O(^1D) \longrightarrow O_2 + N_2$
13	$N_2O + O(^1D) \longrightarrow 2NO$
14	$O(^3P) + O(^3P) \longrightarrow O_2$
15	$H + O_2 \longrightarrow HO_2$
16	$H + O_3 \longrightarrow OH + O_2$
17	$H_2 + OH \longrightarrow H_2O + H$
18	$O_3 + OH \longrightarrow HO_2 + O_2$
19	$OH + O(^3P) \longrightarrow H + O_2$
20	$OH + OH \longrightarrow H_2O + O(^3P)$
21	$OH + OH \longrightarrow H_2O_2$
22	$HO_2 + O(^3P) \longrightarrow OH + O_2$
23	$O_3 + HO_2 \longrightarrow OH + 2O_2$
24	$H + HO_2 \longrightarrow 2OH$
25	$H + HO_2 \longrightarrow H_2O + O(^3P)$
26	$H + HO_2 \longrightarrow H_2 + O_2$

Continued on next page

Table A.2 – continued from previous page

#	Reaction
27	$OH + HO_2 \longrightarrow H_2O + O_2$
28	$HO_2 + HO_2 \longrightarrow H_2O_2 + O_2$
29	$H_2O_2 + OH \longrightarrow H_2O + HO_2$
30	$H_2O_2 + O(^3P) \longrightarrow OH + HO_2$
31	$H_2 + O(^3P) \longrightarrow H + OH$
32	$NO + O_3 \longrightarrow NO_2 + O_2$
33	$NO + HO_2 \longrightarrow NO_2 + OH$
34	$NO_2 + O(^3P) \longrightarrow NO + O_2$
35	$NO_2 + O(^3P) \longrightarrow NO_3$
36	$NO + O(^3P) \longrightarrow NO_2$
37	$NO_2 + O_3 \longrightarrow NO_3 + O_2$
38	$NO_2 + OH \longrightarrow HNO_3$
39	$NO_2 + HO2 \longrightarrow HNO_4$
40	$NO_3 + O(^3P) \longrightarrow NO_2 + O_2$
41	$NO_3 + NO \longrightarrow 2NO_2$
42	$NO_3 + NO_2 \longrightarrow N_2O_5$
43	$N_2O_5 \longrightarrow NO_3 + NO_2$
44	$HNO_3 + OH \longrightarrow NO_3 + H_2O$
45	$HNO_4 + OH \longrightarrow NO_2 + H_2O + O_2$
46	$HNO_4 \longrightarrow NO_2 + HO_2$
47	$NO_3 + OH \longrightarrow NO_2 + HO_2$
48	$NO_3 + HO_2 \longrightarrow NO_2 + OH + O_2$
49	$NO_3 + HO_2 \longrightarrow HNO_3 + O_2$
50	$N + NO \longrightarrow O(^3P) + N_2$
51	$N + O_2 \longrightarrow NO + O(^3P)$
52	$NO + O(^3P) \longrightarrow NO_2$

Continued on next page

Table A.2 – continued from previous page

#	Reaction
53	$Cl + O_2 \longrightarrow ClOO$
54	$O_3 + Cl \longrightarrow ClO$
55	$H_2 + Cl \longrightarrow H + HCl$
56	$CH_4 + Cl \longrightarrow CH_3 + HCl$
57	$CH_2O + Cl \longrightarrow HCO + HCl$
58	$Cl + HO_2 \longrightarrow HCl$
59	$Cl + HO_2 \longrightarrow OH + ClO$
60	$H_2O_2 + Cl \longrightarrow HCl + HO_2$
61	$HOCl + Cl \longrightarrow Cl_2 + OH$
62	$HOCl + Cl \longrightarrow HCl + ClO$
63	$OClO + Cl \longrightarrow 2ClO$
64	$ClOO + Cl \longrightarrow Cl_2$
65	$ClOO + Cl \longrightarrow 2ClO$
66	$ClO + O(^3P) \longrightarrow Cl$
67	$OH + ClO \longrightarrow Cl + HO_2$
68	$OH + ClO \longrightarrow HCl$
69	$HO_2 + ClO \longrightarrow HOCl$
70	$ClO + NO \longrightarrow Cl + NO_2$
71	$NO_2 + ClO \longrightarrow ClONO_2$
72	$ClO + ClO \longrightarrow OClO + Cl$
73	$ClO + ClO \longrightarrow ClOO + Cl$
74	$ClO + ClO \longrightarrow Cl_2$
75	$ClO + ClO \longrightarrow Cl_2O_2$
76	$ClOO \longrightarrow Cl$
77	$NO_3 + ClO \longrightarrow ClOO + NO_2$
78	$Cl_2O_2 \longrightarrow 2ClO$
79	$HCl + OH \longrightarrow H_2O + Cl$

Continued on next page

Table A.2 – continued from previous page

#	Reaction
80	$HCl + O(^3P) \longrightarrow Cl + OH$
81	$OClO + O(^3P) \longrightarrow ClO$
82	$OClO + OH \longrightarrow HOCl$
83	$OClO + NO \longrightarrow NO_2 + ClO$
84	$HOCl + O(^3P) \longrightarrow OH + ClO$
85	$HOCl + OH \longrightarrow H_2O + ClO$
86	$Cl_2 + OH \longrightarrow HOCl + Cl$
87	$ClONO_2 + O(^3P) \longrightarrow NO_3 + ClO$
88	$ClONO_2 + OH \longrightarrow HOCl + NO_3$
89	$ClONO_2 + Cl \longrightarrow Cl_2 + NO_3$
90	$Cl + NO_2 \longrightarrow ClNO_2$
91	$NO_3 + Cl \longrightarrow NO_2 + ClO$
92	$Cl_2 + O(^1D) \longrightarrow Cl + ClO$
93	$HCl + O(^1D) \longrightarrow Cl + OH$
94	$Cl_2O_2 + Cl \longrightarrow Cl_2$
95	$O_3 + Br \longrightarrow BrO$
96	$HO_2 + Br \longrightarrow HBr$
97	$CH_2O + Br \longrightarrow HCO + HBr$
98	$OClO + Br \longrightarrow BrO + ClO$
99	$BrO + O(^3P) \longrightarrow Br$
100	$BrO + HO_2 \longrightarrow HOBr$
101	$BrO + NO \longrightarrow NO_2 + Br$
102	$BrO + NO_2 \longrightarrow BrONO_2$
103	$BrO + ClO \longrightarrow OClO + Br$
104	$BrO + ClO \longrightarrow ClOO + Br$
105	$BrO + ClO \longrightarrow BrCl$
106	$BrO + BrO \longrightarrow 2Br$

Continued on next page

Table A.2 – continued from previous page

#	Reaction
107	$BrO + BrO \longrightarrow Br_2$
108	$HBr + OH \longrightarrow H2O + Br$
109	$HBr + O(^3P) \longrightarrow OH + Br$
110	$HOBr + O(^3P) \longrightarrow BrO + OH$
111	$Br_2 + OH \longrightarrow HOBr + Br$
112	$BrO + OH \longrightarrow HO_2 + Br$
113	$HBr + O(^1D) \longrightarrow OH + Br$
114	$CO + OH \longrightarrow CO_2 + H$
115	$CH_4 + OH \longrightarrow CH_3 + H_2O$
116	$CH_2O + OH \longrightarrow HCO + H_2O$
117	$CH_2O + O(^3P) \longrightarrow HCO + OH$
118	$HCO + O_2 \longrightarrow CO + HO_2$
119	$CH_3 + O_2 \longrightarrow CH_3O_2$
120	$CH_3O + O_2 \longrightarrow CH_2O + HO_2$
121	$CH_3O_2 + NO \longrightarrow CH_3O + NO_2$
122	$CH_3O_2 + HO_2 \longrightarrow CH_3OOH$
123	$CH_3OOH + OH \longrightarrow CH_3O_2 + H_2O$
124	$CH_3OOH + OH \longrightarrow H_2O + CH_2O$
125	$CH_2O + NO_3 \longrightarrow CO + HNO_3 + HO_2$
126	$CO + O(^3P) \longrightarrow CO_2$
127	$ClONO_2 \longrightarrow HNO_3 + HOCl$
128	$ClONO_2 + HCl \longrightarrow HNO_3 + Cl_2$
129	$N_2O_5 \longrightarrow 2HNO_3$
130	$N_2O_5 + HCl \longrightarrow ClNO_2 + HNO_3$
131	$HOCl + HCl \longrightarrow Cl_2 + H_2O$
132	$BrONO_2 \longrightarrow HNO_3 + HOBr$
133	$HOBr + HCl \longrightarrow BrCl + H_2O$

Continued on next page

Table A.2 – continued from previous page

#	Reaction
134	$HBr + HOBr \longrightarrow Br_2 + H_2O$
135	$BrONO_2 + HCl \longrightarrow BrCl + HNO_3$
136	$O_2 \longrightarrow 2O(^3P)$
137	$O_3 \longrightarrow O(^3P)$
138	$O_3 \longrightarrow O(^1D)$
139	$HO_2 \longrightarrow OH + O(^3P)$
140	$H_2O_2 \longrightarrow 2OH$
141	$NO_2 \longrightarrow NO + O(^3P)$
142	$NO_3 \longrightarrow NO_2 + O(^3P)$
143	$NO_3 \longrightarrow NO$
144	$N_2O_5 \longrightarrow NO_3 + NO_2$
145	$HNO_3 \longrightarrow OH + NO_2$
146	$HNO_4 \longrightarrow NO_3 + OH$
147	$HNO_4 \longrightarrow NO_2 + HO_2$
148	$Cl_2 \longrightarrow 2Cl$
149	$OClO \longrightarrow ClO + O(^3P)$
150	$Cl_2O_2 \longrightarrow ClOO + Cl$
151	$HOCl \longrightarrow Cl + OH$
152	$ClONO_2 \longrightarrow NO_3 + Cl$
153	$ClONO_2 \longrightarrow Cl + NO_2 + O(^3P)$
154	$ClNO_2 \longrightarrow Cl + NO_2$
155	$BrCl \longrightarrow Cl + Br$
156	$BrO \longrightarrow Br + O(^3P)$
157	$HOBr \longrightarrow OH + Br$
158	$BrONO_2 \longrightarrow NO_3 + Br$
159	$BrONO_2 \longrightarrow BrO + NO_2$
160	$CH_2O \longrightarrow HCO + H$

Continued on next page

Table A.2 – continued from previous page

#	Reaction
161	$CH_2O \longrightarrow CO + H2$
162	$CH_3OOH \longrightarrow CH_3O + OH$
163	$ClOO \longrightarrow ClO + O(^3P)$
164	$ClO \longrightarrow Cl + O(^3P)$
165	$Br_2 \longrightarrow 2Br$
166	$O_2 \longrightarrow O(^1D) + O(^3P)$
167	$H_2O \longrightarrow H + OH$
168	$N_2O \longrightarrow O(^1D)$
169	$CH_4 \longrightarrow CH_3O_2 + H$
170	$HCl \longrightarrow H + Cl$
171	$NO \longrightarrow N + O(^3P)$
172	$CCl_4 \longrightarrow 4Cl$
173	$CFC11 \longrightarrow HF + 3Cl$
174	$CFC12 \longrightarrow 2HF$
175	$CFC113 \longrightarrow 3HF$
176	$CFC114 \longrightarrow 4HF$
177	$CFC115 \longrightarrow 5HF$
178	$HCFC22 \longrightarrow 2HF$
179	$Ha1211 \longrightarrow 2HF$
180	$Ha1301 \longrightarrow 3HF$
181	$CH_3Cl \longrightarrow CH_3 + Cl$
182	$CH_3CCl_3 \longrightarrow 3Cl$
183	$CH_3Br \longrightarrow CH_3 + Br$
184	$CHBr_3 \longrightarrow 3Br$
185	$CCl_4 + O(^1D) \longrightarrow 4Cl$
186	$CFC11 + O(^1D) \longrightarrow HF + 3Cl$
187	$CFC12 + O(^1D) \longrightarrow 2HF$

Continued on next page

Table A.2 – continued from previous page

#	Reaction
188	$CFC113 + O(^1D) \longrightarrow 3HF$
189	$CFC114 + O(^1D) \longrightarrow 4HF$
190	$CFC115 + O(^1D) \longrightarrow 5HF$
191	$HCFC22 + O(^1D) \longrightarrow 2HF$
192	$HCFC22 + OH \longrightarrow H_2O + Cl$
193	$Ha1211 + O(^1D) \longrightarrow 2HF$
194	$Ha1301 + O(^1D) \longrightarrow 3HF$
195	$CH_3Cl + OH \longrightarrow Cl + HO_2$
196	$CH_3Cl + Cl \longrightarrow 2HCl$
197	$CH_3CCl_3 + OH \longrightarrow H_2O + 3Cl$
198	$CH_3Br + O(^1D) \longrightarrow Br$
199	$CH_3Br + OH \longrightarrow H_2O + Br$
200	$CHBr_3 + OH \longrightarrow H_2O + 3Br$

Table A.2: Chemical reactions that are included in the BIRA box model.

Acknowledgments

First and foremost, I would like to thank my supervisor, Prof. Michel Bourqui. Through our discussions I have gained insight into atmospheric dynamics and especially atmospheric chemistry. In my time working on this project, he has helped me become familiar and comfortable with a subject that was new to me. Thanks also to him for all of the help and advice provided, ensuring that my research was both exciting and successful. I would also like to thank those that I have collaborated with on this project. Thanks to Stella Melo from the Canadian Space Agency for advising my research and posing interesting questions. Thanks to Prof. Paul Charbonneau from the Université de Montréal for providing insight into the solar aspect of the project. I would also like to thank Jerry Harder from the University of Colorado, Ken Tapping from National Research Council Canada, and Donald Danskin from Natural Resources Canada for their support, encouragement and interest at conferences. Finally, I would like to thank the Department of Atmospheric and Oceanic Sciences at McGill University for providing a friendly work environment.

References

Austin, J., L. L. Hood, and B. E. Soukharev (2007), Solar cycle variations of stratospheric ozone and temperature in simulations of a coupled chemistry-climate model, *Atmos. Chem. Phys*, *7*, 1693–1706.

Bourqui, M., C. Taylor, and K. Shine (2005), A new fast stratospheric ozone chemistry scheme in an intermediate general-circulation model. II: Application to effects of future increases in greenhouse gases, *Quarterly Journal of the Royal Meteorological Society*, *131*(610).

Brasseur, G. (1993), The response of the middle atmosphere to long-term and short-term solar variability: a two-dimensional model., *J. Geophys. Res.*, *98*(D12).

Brasseur, G., A. De Rudder, G. M. Keating, and M. C. Pitts (1987), Response of middle atmosphere to short-term solar ultraviolet variations: 2. Theory, *Journal of Geophysical Research-Atmospheres*, *92*(D1).

Brasseur, G., S. Walters, M. H. Hitchman, M. Dymek, E. Falise, and M. Pirre (1990), An interactive chemical dynamical radiative two-dimensional model of the middle atmosphere, *Journal of Geophysical Research*, *95*(D5), 5639–5655.

Chandra, S., and R. McPeters (1994), The solar cycle variation of ozone in the stratosphere inferred from Nimbus 7 and NOAA 11 satellites, *Journal of Geophysical Research. D. Atmospheres*, *99*, 20.

Charbonneau, P., A. Crouch, and K. Tapping (2008), L'Irradiance Solaire et ses Variations, *Physics in Canada/La Physique au Canada*.

Chipperfield, M. (1999), Multiannual simulations with a three-dimensional chemical transport model, *Journal of Geophysical Research-Atmospheres*, *104*(D1).

Crouch, A. D., P. Charbonneau, G. Beaubien, and D. Paquin-Ricard (2008), A Model for the Total Solar Irradiance Based on Active Region Decay, *The Astrophysical Journal*, *677*, 723–741.

de F. Forster, P. M., M. Blackburn, R. Glover, and K. P. Shine (2000), An examination of climate sensitivity for idealised climate change experiments in an intermediate general circulation model, *Climate Dynamics*, *16*(10), 833–849.

Dessler, A. E. (2000), *The chemistry and physics of stratospheric ozone*, Academic press.

Egorova, T., E. Rozanov, E. Manzini, M. Haberreiter, W. Schmutz, V. Zubov, and T. Peter (2004), Chemical and dynamical response to the 11-year variability of the solar irradiance simulated with a chemistry-climate model, *Geophys. Res. Lett*, *31*(6119), 1–4.

Egorova, T., E. Rozanov, V. Zubov, W. Schmutz, and T. Peter (2005), Influence of solar 11-year variability on chemical composition of the stratosphere and mesosphere simulated with a chemistry-climate model, *Advances in Space Research*, *35*(3), 451–457.

Fioletov, V. E. (2009), Estimating the 27-day and 11-year solar cycle variations in tropical upper stratospheric ozone, *Journal of Geophysical Research-Atmospheres*, *114*(D2), D02,302.

Fleming, E., S. Chandra, C. Jackman, D. Considine, and A. Douglass (1995), The middle atmospheric response to short and long term solar UV variations: Analysis of observations and 2D model results, *Journal of Atmospheric and Terrestrial Physics*, *57*(4), 333–365.

Fröhlich, C., and J. Lean (2002), Solar irradiance variability and climate, *Astronomische Nachrichten*, *323*(3-4), 203–212.

Fröhlich, C., and J. Lean (2004), Solar radiative output and its variability: evidence and mechanisms, *Astronomy and Astrophysics Review*, *12*(4), 273–320.

Haigh, J. (1996), The impact of solar variability on climate, *Science*, *272*(5264), 981.

Haigh, J. D. (1994), The role of stratospheric ozone in modulating the solar radiative forcing of climate, *Nature*, *370*(6490), 544–546.

Harder, J., J. Fontenla, O. White, G. Rottman, and T. Woods (2005), Solar spectral irradiance variability comparisons of the SORCE SIM instrument with monitors of solar activity and spectral synthesis, *Memorie-Societa Astronomica Italiana*, *76*(4), 735.

Hedin, A. (1991), Extension of the MSIS thermosphere model into the middle and lower atmosphere, *Journal of Geophysical Research-Space Physics*, *96*(A2).

Hood, L. L., and S. Zhou (1999), Stratospheric effects of 27-day solar ultraviolet variations- The column ozone response and comparisons of solar cycles 21 and 22, *Journal of Geophysical Research*, *104*, 26.

Intergovernmental Panel of Climate Change (2001), *Climate change 2001: the scientific basis*, Cambridge University Press Cambridge.

Intergovernmental Panel of Climate Change, WGI (2007), Climate Change 2007: The Physical Science Basis, *Summary for Policy Makers, Contribution of Working Group I to the Fourth Assessment Report of the Intergovernmental Panel on Climate Change*.

Keating, G., G. Brasseur, L. Chiou, and N. Hsu (1994), Estimating 11-year solar UV variations using 27-day response as a guide to isolate trends in total column ozone, *Advances in Space Research-Oxford-*, *14*, 199–199.

Keating, G. M., M. C. Pitts, G. Brasseur, and A. De Rudder (1987), Response of middle atmosphere to short-term solar ultraviolet variations: 1. Observations, *Journal of Geophysical Research-Atmospheres*, *92*(D1).

Khosravi, R., G. Brasseur, A. Smith, D. Rusch, S. Walters, S. Chabrillat, and G. Kockarts (2002), Response of the mesosphere to human-induced perturbations and solar variability calculated by a 2-D model, *Journal of Geophysical Research-Atmospheres*, *107*(D18), 4358.

Lean, J. (1997a), The sun's variable radiation and its relevance for Earth, *Annual review of Astronomy and Astrophysics*, *35*(1), 33–67.

Lean, J. L. (1997b), Detection and parameterization of variations in solar mid- and near-ultraviolet radiation (200-400 nm), *Journal of Geophysical Research*, *102*(D25), 29–939.

Matthes, K., K. Kodera, J. D. Haigh, D. T. Shindell, K. Shibata, U. Langematz, E. Rozanov, and Y. Kuroda (2003), GRIPS solar experiments intercomparison project: Initial results, *Pap. Meteorol. Geophys*, *54*(2), 71–90.

NASA (2000), Studying earth's environment from space, `http://www.ccpo.odu.edu/SEES/index.html`.

North, G. R., Q. Wu, and M. J. Stevens (2004), Detecting the 11-year solar cycle in the surface temperature field, *Solar Variability and its Effects on Climate. Geophysical Monograph 141, edited by Judit M. Pap, Peter Fox, Claus Frohlich, Hugh S. Hudson, Jeffrey Kuhn, John McCormack, Gerald North, William Sprigg and ST Wu. ISBN 0-87590-406-8. Published by the American Geophysical Union, Washington, DC, USA, 2004, p. 251.*

Ravishankara, A. R. (2005), Introductory Lecture: Chemistry–climate coupling: the importance of chemistry in climate issues, *Faraday Discussions*, *130*, 9–25.

Rind, D., and N. Balachandran (1995), Modeling the effects of UV variability and the QBO on the troposphere–stratosphere system. Part II: The troposphere, *Journal of Climate*, *8*(8), 2080–2095.

Rozanov, E., T. Egorova, C. Frohlich, M. Haberreiter, T. Peter, and W. Schmutz

(2002), Estimation of the ozone and temperature sensitivity to the variation of spectral solar flux, *European Space Agency-Publications-ESA SP*, *508*, 181–184.

Rozanov, E., T. Egorova, W. Schmutz, and T. Peter (2006), Simulation of the stratospheric ozone and temperature response to the solar irradiance variability during sun rotation cycle, *Journal of Atmospheric and Solar-Terrestrial Physics*, *68*(18), 2203–2213.

Rozanov, E. V., M. E. Schlesinger, T. A. Egorova, B. Li, N. Andronova, and V. A. Zubov (2004), Atmospheric response to the observed increase of solar UV radiation from solar minimum to solar maximum simulated by the University of Illinois at Urbana-Champaign climate-chemistry model, *J. Geophys. Res*, *109*.

Shindell, D., D. Rind, N. Balachandran, J. Lean, and P. Lonergan (1999), Solar cycle variability, ozone, and climate, *Science*, *284*(5412), 305.

Solanki, S., and M. Fligge (1999), A reconstruction of total solar irradiance since 1700, *Geophys. Res. Lett*, *26*(16), 2465–2468.

Soukharev, B., and L. Hood (2006), Solar cycle variation of stratospheric ozone: Multiple regression analysis of long-term satellite data sets and comparisons with models, *J. Geophys. Res*, *111*, D20,314.

Taylor, C., and M. Bourqui (2005), A new fast stratospheric ozone chemistry scheme in an intermediate general-circulation model. I: Description and evaluation, *Quarterly Journal of the Royal Meteorological Society*, *131*(610).

Thuillier, G., A. Joukoff, and W. Schmutz (2003), The PICARD mission, in *In: Solar variability as an input to the Earth's environment. International Solar Cycle Studies (ISCS) Symposium, 23-28 June 2003, Tatranská Lomnica, Slovak Republic. Ed.: A. Wilson. ESA SP-535, Noordwijk: ESA Publications Division, ISBN 92*, vol. 9092, pp. 251–257.

Tourpali, K., C. Schuurmans, R. Van Dorland, B. Steil, and C. Brühl (2003), Stratospheric and tropospheric response to enhanced solar UV radiation: A model study, *Geophysical Research Letters*, *30*(5), 1231.

Williams, V., J. Austin, and J. D. Haigh (2001), Model simulations of the impact of the 27-day solar rotation period on stratospheric ozone and temperature, *Advances in Space Research*, *27*(12), 1933–1942.

Zhou, S., G. J. Rottman, and A. J. Miller (1997), Stratospheric ozone response to short-and intermediate-term variations of solar UV flux, *Journal of Geophysical Research-Atmospheres*, *102*(D7).